Axel Deloncle

Three-dimensional instabilities in stratified fluids

Thèse de doctorat
LadHyX - Ecole Polytechnique
2007

Contents

Chapter 1

Introduction

1.1 Geophysical fluids

Geophysical fluids like the atmosphere and the oceans have generally a variable density along the vertical direction. This density stratification is due, for instance, to variations of temperature and pressure in the atmosphere and to variations of temperature and salinity in the oceans. In most cases, the density decreases with altitude, resulting in a stable stratification. Parcels of fluid that are displaced vertically are accelerated back to their initial position by a restoring buoyancy force. They will oscillate around their equilibrium position at the Brunt–Väisälä frequency $N = \sqrt{-g/\rho \, \mathrm{d}\rho/\mathrm{d}z}$, where ρ is the ambient density and g the gravity acceleration along the vertical z-direction. In a stably stratified fluid, the large vertical displacements are then highly inhibited.

Geophysical fluids are also subject to a Coriolis force because of the Earth's rotation. These fluids are therefore referred to as stratified and rotating fluids. The importance of the stratification and rotation in the dynamics varies with scale. At the largest geophysical scales, rotation and stratification are both significant. At atmospheric mesoscale (1km–100km) and oceanic submesoscale (10m–10km), Coriolis effects weaken but stratification effects are still important.

Because of the limitation of computers resources, atmospheric and oceanic numerical models cannot resolve all scales, from large scales (1000km) down to small dissipative scales (1mm). The grid resolution is generally limited to a few kilometres to hundreds of kilometres. However, the large scale dynamics is very sensitive to the subgrid processes, those that have dimensions smaller than the model resolution. In both the atmosphere and ocean, a good understanding of the dynamics of these subgrid scales is thus crucial in the development of accurate parameterizations needed in the climate and meteorological models. On these subgrid scales, the flows are stratified but weakly influenced by the

rotation. Moreover, the Reynolds number is large, resulting in turbulent flows. This stratified regime is the object of this dissertation.

1.2 Basic concepts in turbulence

Before going into the main object of this dissertation, we recall some basic concepts in turbulence that are important in the understanding of the following. We present briefly two classical cases: homogeneous turbulence and two-dimensional turbulence.

1.2.1 Homogeneous turbulence

In homogeneous and isotropic turbulence, the flow is classically considered as a superposition of structures covering a large range of time and length scales. The energy which is injected at large scales is dissipated at the small dissipative viscous scales. This simple observation leads one to expect an energy flux between scales. Richardson (1922) has proposed that the large structures transfer part of their energy to smaller ones through a "cascade" process. The key idea is that this process is iterative and implies a hierarchy of vortices with different scales. This direct cascade of energy, from large to small scales, ends up when viscous effects become dominant leading to the dissipation of the corresponding small vortices. Using self-similarity arguments, Kolmogorov (1941) has derived the famous power law dependence of the energy spectrum: $E(k) \sim k^{-5/3}$, where k is the wavenumber, which has been confirmed by numerous experiments and numerical simulations.

Different mechanisms have been proposed to explain the direct energy cascade observed in homogeneous turbulence. For instance, let us consider a tube of vorticity placed in a background strain field (see figure 1.1). The vortex tube is stretched leading to a contraction of the vortex along the stretching direction. The vorticity of the fluid increases to satisfy angular momentum conservation. A direct consequence is that there is an increase of small-scale vorticity, as well as small scale kinetic energy. This stretching process thus leads to a transfer of energy from large scales to small scales.

Another possible mechanism it the destabilization through successive instabilities. The figure 1.2 shows the example of the destabilization of a large-scale shear layer by the Kelvin–Helmholtz instability. As seen on figure 1.2, a row of vortices appear owing to the nonlinear development of the Kelvin–Helmholtz instability. This row eventually leads to the formation of small billows, through stretching and successive destabilizations. Here again this corresponds to a transfer of energy from large scales to small scales.

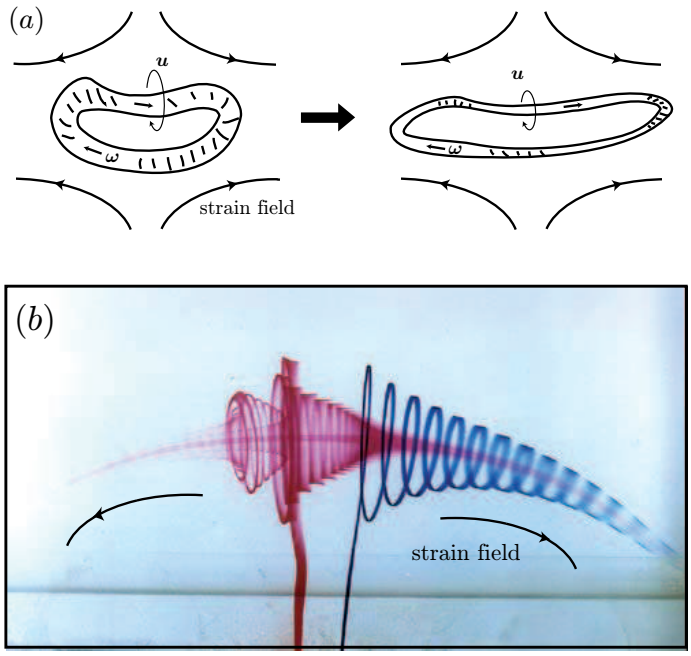

Figure 1.1: Stretching of a vortex tube by a background strain. The sketch (a) is from Morize (2006) and the experiment (b) from Petitjeans (2003).

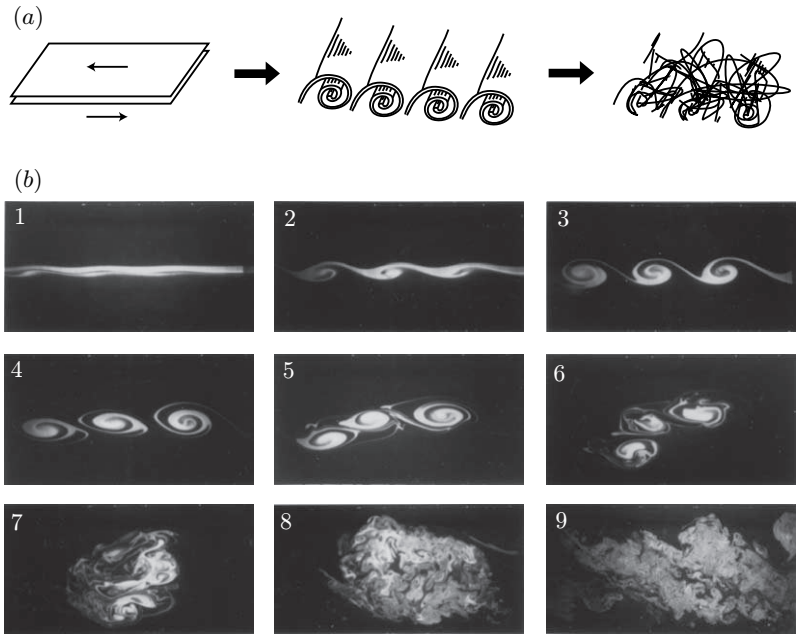

Figure 1.2: Destabilization of a shear layer by a Kelvin–Helmholtz instability. Small and intense vortices are formed during the late stage of the nonlinear evolution of the instability. The sketch (a) is from Morize (2006) and the experiment (b) from Falkovich & Sreenivasan (2006).

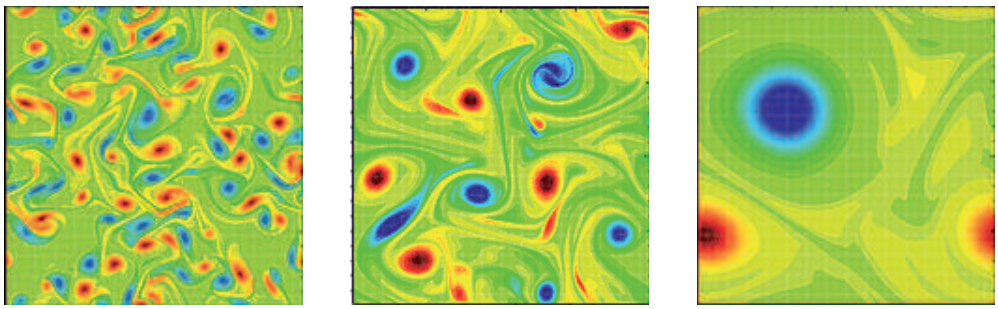

Figure 1.3: Numerical simulation of two-dimensional turbulence. The initial small vortices merge and form large vortices. From Clercx *et al.* (1999).

These two example of mechanisms are certainly too simple to fully explain the dynamics of homogeneous turbulence. However, they are valuable to understand the key processes underlying turbulence.

1.2.2 Two-dimensional turbulence

An important property of two-dimensional flows is that the process of vortex stretching is absent. This implies that the mechanism of stretching mentioned above to explain the direct energy cascade in homogeneous turbulence cannot apply. As expected, two-dimensional turbulence has a distinctive behaviour. The theory of Kraichnan (1967) predicts the existence of an inverse energy cascade, i.e. from small scales to large scales. This inverse energy flux is classically explained by a mechanism of merging of the vortices: small vortices merge into large vortical structures as illustrated by a numerical simulation in figure 1.3. The energy accumulates at the largest scales allowed by the system and no stationary state is reached in the absence of a dissipative process affecting the large scales. Scaling arguments lead to a spectrum similar to the one of the three-dimensional turbulence: $E(k_h) \sim k_h^{-5/3}$, where k_h is the horizontal wavenumber. However, one should keep in mind that this identical spectrum is due to physical processes of different nature. At the same time as the vortices merge, thin filaments of vorticity are formed and ejected. This corresponds to a direct cascade of enstrophy to small scales.

1.3 Structure of the stratified turbulence

The buoyancy force in stably stratified fluids highly inhibits vertical motion, giving rise to a specific dynamics. A stratified flow can be decomposed into two main types of motion (Riley & Lelong 2000). First, internal gravity waves can propagate because of the restoring buoyancy force. Secondly, horizontal motions are not affected by the stratification and can thus develop. This

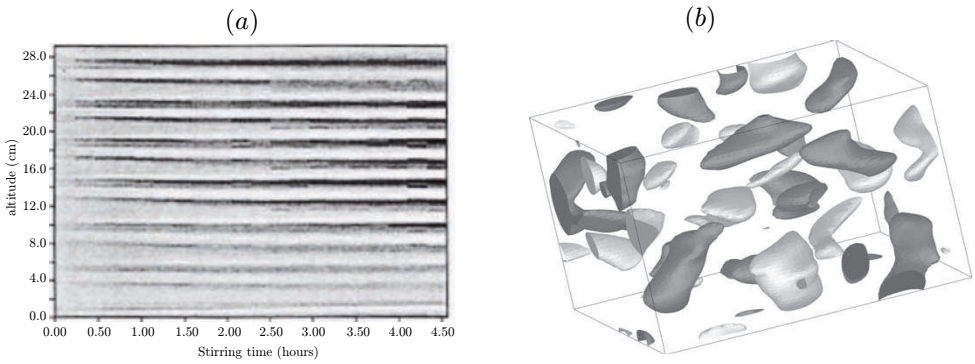

Figure 1.4: (*a*): Shadowgraph of the flow obtained by towing a rake of vertical cylinders in a stratified fluid (Holford & Linden 1999). (*b*): Three-dimensional structure of the vertical vorticity of the flow obtained by towing a rake of vertical flat plates in a stratified fluid (Praud *et al.* 2005).

nonpropagating component of the flow possesses potential vorticity and corresponds to vortices with their axis aligned with the vertical direction. In this dissertation, we do not address propagating internal waves that have already been largely treated (see Staquet & Sommeria 2002 for a review); instead we address the nonpropagating component of the motion.

As expected, stratified flows are highly anisotropic because of the buoyancy force. A commonly observed feature of stratified turbulence is the formation of quasi-horizontal layers, often described as pancake structures. This layering was observed in numerous experiments such as the grid turbulence experiments presented in figure 1.4 (Holford & Linden 1999; Praud *et al.* 2005). Similar structures are also present in numerical simulations (Waite & Bartello 2004; Godeferd & Staquet 2003; Lindborg 2006; Brethouwer *et al.* 2007) (see figure 1.5). The energy dissipation is principally due to the strong vertical shear that develops between the horizontal layers.

A complementary description can be given in the spectral space. By analyzing measurements collected by airplanes in the mesoscale atmosphere, Nastrom & Gage (1985) have found a robust power law of the energy horizontal spectrum in $k_h^{-5/3}$ (see figure 1.6*a*). Remarkably, this is the same power law as in homogeneous or two-dimensional turbulence. In contrast, a spectrum of the form k_v^{-3} is obtained on the vertical direction, where k_v is the vertical wavenumber (Smith *et al.* 1987; Cot 2001, figure 1.6*b*). This confirms the strong anisotropy of stratified flows.

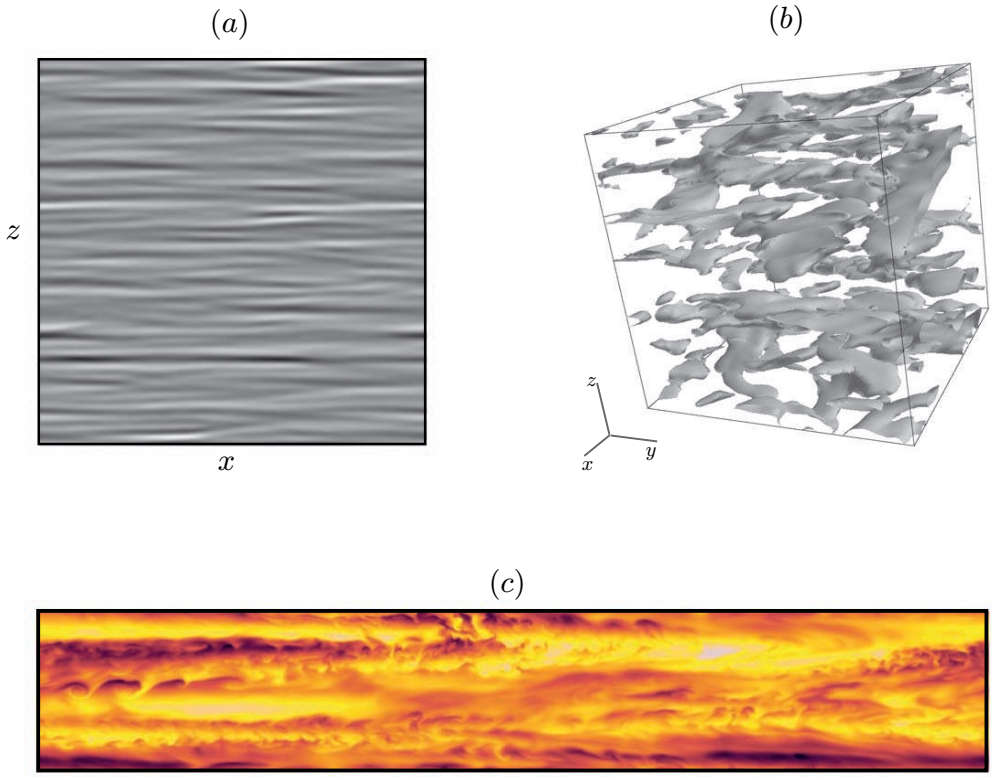

Figure 1.5: (*a*): Vertical cross-section of the horizontal vorticity in a simulation of stably stratified forced turbulence (Waite & Bartello 2004). (*b*): Isosurfaces of the vertical gradient of the horizontal velocity in a simulation of stably stratified decaying turbulence (Godeferd & Staquet 2003). (*c*): Vertical cross-section of the temperature field in a simulation of stably stratified forced turbulence (Brethouwer *et al.* 2007).

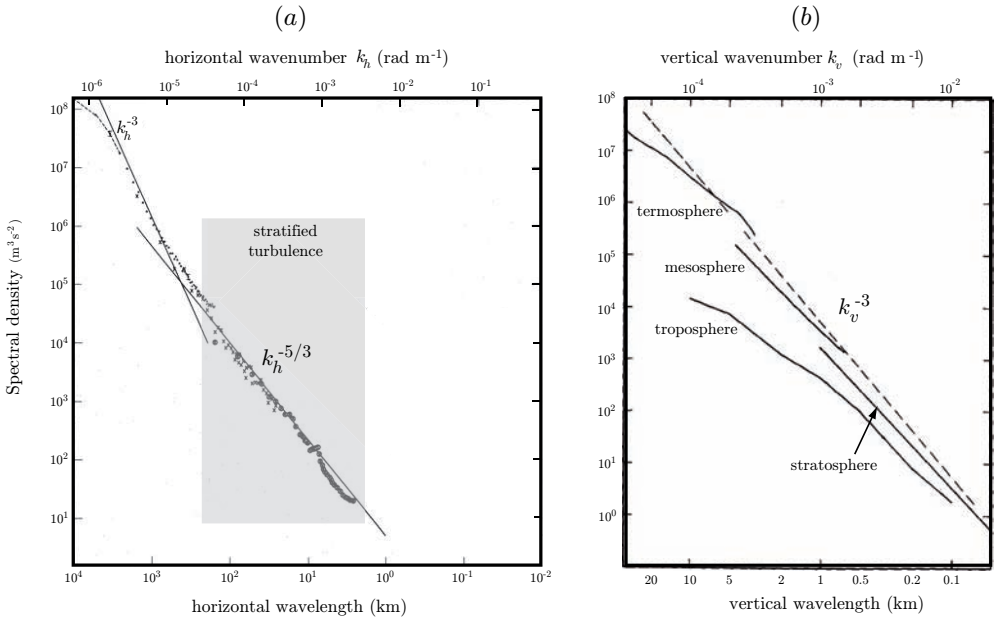

Figure 1.6: (a): horizontal power spectrum of zonal wind. Measurements were collected using commercial airplanes flights in the upper troposphere and lower stratosphere (Nastrom & Gage 1985). (b): vertical power spectrum of horizontal wind (Smith *et al.* 1987).

1.4 Theoretical models of stratified turbulence

1.4.1 A two-dimensional dynamics?

In spite of numerous observations in nature, in the laboratory or in numerical simulations, there is no clear theoretical explanation of the dynamics of stratified turbulence. Different theories have been suggested to explain the various observations of § 1.3. Because the stratification constrains the motion to be approximately layerwise two-dimensional, a two-dimensional dynamics has been first proposed in strongly stratified fluids as a good approximation of the vortical motions (Riley *et al.* 1981; Lilly 1983). In this scaling analysis, the horizontal and vertical length scales are both considered large compared to the buoyancy length scale defined as U/N where U is the horizontal velocity scale. A direct consequence of this theory is that strongly stratified turbulence should be similar to two-dimensional turbulence. A horizontal spectrum $k_h^{-5/3}$ is thus expected, in agreement with the observations of Nastrom & Gage (1985), and an inverse energy cascade is speculated. In this theory, the flow is considered as a "stack" of horizontal layers, without any vertical coupling. In this case, a mean vertical shear will increase in time if it is initially non-zero, which could explain the decorrelation of the horizontal layers. However, because the vertical dependence is undetermined, this model does not predict any vertical scale the layers and fails to explain the k_v^{-3} vertical spectrum of energy.

1.4.2 A three-dimensional dynamics?

Recent studies have questioned the validity of the two-dimensional turbulence hypothesis. By calculating high order statistical moments, Lindborg (1999) and Cho & Lindborg (2001) has concluded that the energy cascade in the atmospheric kinetic energy spectrum is a direct energy cascade in the mesoscales, i.e. from large to small scales, suggesting a three-dimensional dynamics. Numerical simulations of stratified turbulence also support the direct cascade hypothesis. Waite & Bartello (2004), Lindborg (2006) and Brethouwer *et al.* (2007) have obtained a nearly stationary state in their simulations of strongly stratified turbulence forced in large-scales, which indicates an energy flux from large to small scales. In strongly stratified freely decaying turbulence, the results of Riley & deBruynKops (2003) suggest that the larger-scale, quasi-horizontal motions would be a continuous source of smaller-scale turbulence through shear instabilities.

Billant & Chomaz (2001) and Lindborg (2006) have proposed a scaling of the governing equations taking into account three-dimensional effects. In this analysis, the vertical length scales like the buoyancy length scale U/N, in contrast with the two-dimensional analysis of Riley *et al.* (1981) and Lilly (1983). Using self-similarity arguments, Lindborg (2006) has derived an en-

ergy horizontal spectrum in $k_h^{-5/3}$ corresponding to a direct energy cascade. Moreover, the three-dimensional dependence predicted by the scaling leads to a vertical energy spectrum in k_v^{-3}, confirming the observations. Horizontal layers with a thickness scaling like U/N were also observed numerical simulations at sufficiently high Reynolds number (Waite & Bartello 2004; Lindborg 2006; Brethouwer *et al.* 2007).

1.5 Objectives

The results mentioned previously tend to show that stratified turbulence is three-dimensional but highly anisotropic with a direct cascade of energy.

However, what physical mechanisms are behind this dynamics remains an open question. The main purpose of this dissertation is the study of the fundamental processes which can explain the structure and dynamics of stratified turbulence.

One ubiquitous feature of stratified turbulence is its three-dimensional structure. Billant & Chomaz (2000*a*) and Otheguy *et al.* (2006) have investigated the stability of a pair of columnar vertical vortices in a strongly stratified fluid and showed the existence of a three-dimensional instability called zigzag instability that vertically bends the vortices with a most unstable vertical wavelength scaling like the buoyancy length scale U/N (see figures 1.7 and 1.8). In their experiments, this instability ultimately leads to the formation of pancake vortices as illustrated in figure 1.9. This instability limits the vertical coherence of the flow and therefore it has been speculated that it may explain and predict the vertical size of the horizontal layers observed in stratified turbulence.

However, a number of questions have to be answered to assess this hypothesis. First, the zigzag instability was evidenced only in strongly stratified fluids and for very idealized configurations: a pair of counter-rotating vortices (Billant & Chomaz 2000*a*), a pair of co-rotating vortices (Otheguy *et al.* 2006) and an elliptic vortex in a background strain (Billant *et al.* 2006). A mechanism having a significant role in stratified turbulence should be robust and should apply in many conditions. It remains unclear how generic the zigzag instability is.

Could the zigzag instability affect simpler flows than vortex pairs or an elliptic vortex? To address this question, we have investigated the three-dimensional stability of one of the simplest flow that may be encountered in stratified flows: a horizontal shear layer. It is well-known that such flow is most unstable to a two-dimensional Kelvin–Helmholtz instability in homogeneous fluid (see figure 1.2) but could it be most unstable to three-dimensional perturbations in stratified fluids? This question will be answered in chapter 3.

Could the zigzag instability also affect complex flows made of a large number of interacting vertical vortices such as the Kármán vortex street that is

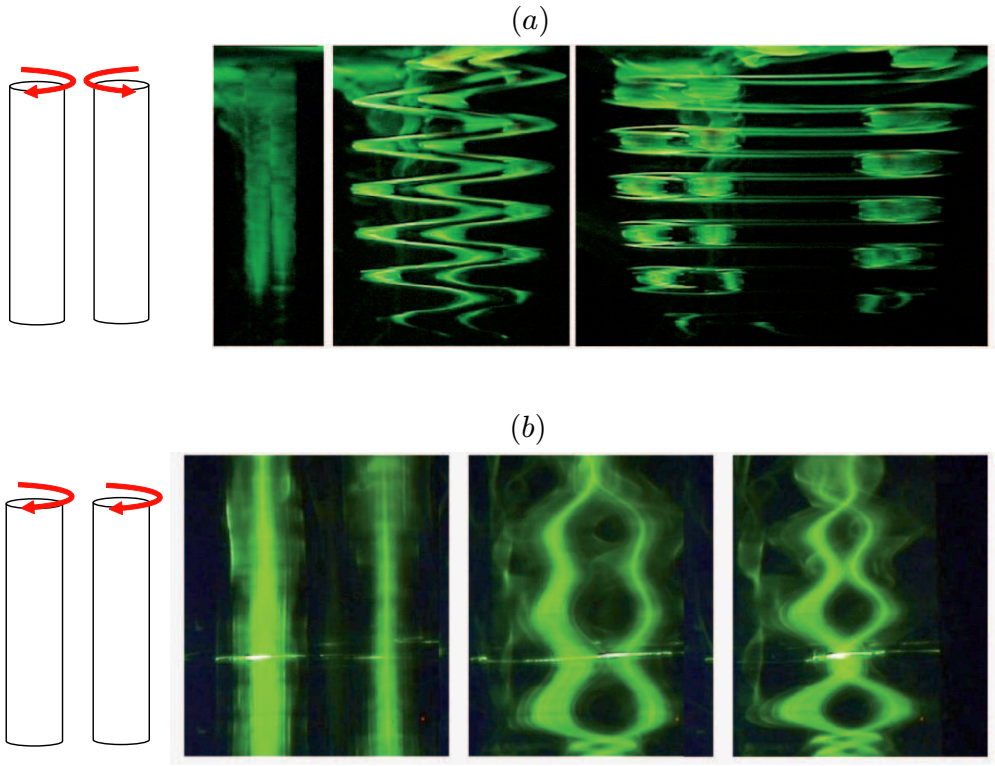

Figure 1.7: Development of the zigzag instability that affects a pair of (a) counter-rotating vortices (Billant & Chomaz 2000a) and (b) co-rotating vortices (Otheguy *et al.* 2006) in a strongly stratified fluid.

Figure 1.8: Sketch of the zigzag mode of a pair of counter-rotating vortices: the vortices are bended on the vertical. From Billant *et al.* (2007).

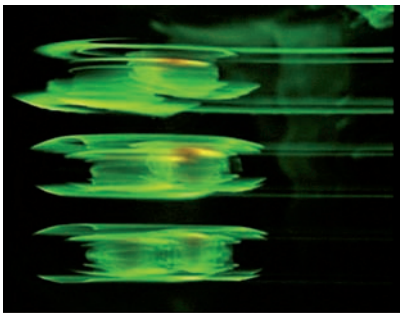

Figure 1.9: (a) Close-up view of the pancake vortices appearing in the late development of the zigzag instability. From Billant & Chomaz (2000a).

formed behind a vertical cylinder? The results of a three-dimensional stability are presented in chapters 4 and 5. In this case, we have investigated the effect of the Coriolis force in addition to stratification effects because of its interest in geophysical flows.

Finally, the more difficult problem of the three-dimensional stability of unsteady two-dimensional flows is tackled in chapter 6, in order to understand the three-dimensionalization of more realistic flows.

Another fundamental question on stratified turbulence is how the direct cascade of energy is achieved? i.e. how the energy is transferred from the large to the small dissipative scales. Do the pancake vortices, formed by the three-dimensional instability, break-up into smaller structures through successive instabilities? Or does it exist mechanisms which are able to transfer energy directly to the small dissipative scales? To address these questions, we have studied in chapter 7 by means of direct numerical simulations the nonlinear development of the zigzag instability on the simple case of a pair of counter-rotating vortices.

1.6 Outline

The body of this dissertation is composed of six chapters. Four of them are presented in the form of publications and hence can be read separately.

Chapter 2: we present the numerical code and the main steps of the parallelization that has allowed us to run large **direct numerical simulations** on parallel computers.

Chapter 3: this chapter is devoted to an investigation of the three-dimensional **stability of a horizontal flow sheared horizontally**, the hyperbolic tangent velocity profile, in a stably stratified fluid. We are particularly interested

in the destabilization of three-dimensional modes for strong stratifications.

Chapters 4 and 5: the **stability of three classical vortex arrays** is investigated in stratified and rotating fluid: the Kármán vortex street, the symmetric double row and the single row of co-rotating vortices. We determine when the zigzag instability should occur by theoretical (chapter 4) and numerical (chapter 5) stability analysis.

Chapter 6: the **stability of unsteady vortex distributions** is tackled. We show that random distributions of vortices that are initially two-dimensional are unstable to the zigzag instability in stratified fluids. This supports the idea that the zigzag instability is a generic mechanism that can occur in complex stratified flows.

Chapter 7: we present high-resolution direct numerical simulations of the **nonlinear evolution of the zigzag instability** of a pair of counter-rotating vertical vortices in a stratified fluid. We focus on the energy transfers induced by the zigzag instability.

Chapter 2

NS3D: a direct numerical simulation code

We present in this chapter the direct numerical simulation (DNS) code used throughout the dissertation to simulate stratified flows. The code integrates the Navier–Stokes equations under the Boussinesq approximation and is called NS3D for Three-Dimensional equations. It was first written for a homogeneous fluid by Vincent & Meneguzzi (1991) and later adapted to stratified fluids by Billant & Chomaz (2000*c*) and Otheguy *et al.* (2006). We describe here the main steps of the parallelization of this code which has allowed us to run large simulations on parallel computers.

2.1 Governing equations

The code integrates the Navier–Stokes equation within the Boussinesq approximation:

$$\frac{\partial \boldsymbol{u}}{\partial t} = \boldsymbol{u} \times \boldsymbol{\omega} - \boldsymbol{\nabla}\left[\frac{p}{\rho_0} + \frac{\boldsymbol{u}^2}{2}\right] + b\boldsymbol{e}_z + \nu\boldsymbol{\Delta}\boldsymbol{u}, \tag{2.1a}$$

$$\boldsymbol{\nabla}\cdot\boldsymbol{u} = 0, \tag{2.1b}$$

$$\frac{\partial b}{\partial t} + \boldsymbol{u}\cdot\boldsymbol{\nabla} b + N^2 w = D\Delta b, \tag{2.1c}$$

where $\boldsymbol{u} = (u, v, w)$ is the velocity vector in Cartesian coordinates (x, y, z), ρ_0 a constant reference density, p the pressure, $b = -g\rho/\rho_0$ the buoyancy with ρ the density perturbation with respect to the base density $\rho_0 + \overline{\rho}(z)$, g the gravity and $\boldsymbol{e}_z$ the unit vector in the upward z-direction. $N = \sqrt{-g/\rho_0\, d\overline{\rho}/dz}$ is the Brunt–Väisälä frequency assumed here constant, ν is the kinematic viscosity and D the molecular diffusivity of the stratifying agent.

2.2 Numerical method

To integrate numerically the equations (2.1), a pseudo-spectral scheme has been implemented in Cartesian coordinates with periodic boundary conditions. The main steps of the numerical methods are outlined below.

The variables are expressed in Fourier space by application of a three-dimensional Fourier transform, for example:

$$\hat{\boldsymbol{u}}(k_x,k_y,k_z,t)=\iiint \boldsymbol{u}(x,y,z,t)\mathrm{e}^{-\mathrm{i}(k_x x+k_y y+k_z z)}\mathrm{d}x\mathrm{d}y\mathrm{d}z, \tag{2.2a}$$

where the hat denotes the Fourier transform, and k_z, k_y and k_z are the components of the total wavenumber $\boldsymbol{k}=(k_x,k_y,k_z)$. In spectral space, the governing equations (2.1) are replaced by:

$$\frac{\partial\hat{\boldsymbol{u}}}{\partial t}=\mathsf{P}(\boldsymbol{k})\left(\widehat{\boldsymbol{u}\times\boldsymbol{\omega}}+\hat{b}\boldsymbol{e_z}\right)-\nu\boldsymbol{k}^2\hat{\boldsymbol{u}}, \tag{2.3a}$$

$$\frac{\partial\hat{b}}{\partial t}=-\mathrm{i}\boldsymbol{k}\cdot\widehat{b\boldsymbol{u}}-N^2\hat{w}-D\boldsymbol{k}^2\hat{b}. \tag{2.3b}$$

The tensor $\mathsf{P}(\boldsymbol{k})$ with Cartesian components $\mathsf{P}_{ij}=\delta_{ij}-k_ik_j/\boldsymbol{k^2}$ designates the projection operator on the space of solenoidal fields so as to enforce the divergence equation $\boldsymbol{k}\cdot\boldsymbol{u}=0$. The viscous and diffusive terms are integrated exactly:

$$\frac{\partial\hat{\boldsymbol{u}}\mathrm{e}^{\nu\boldsymbol{k}^2t}}{\partial t}=\left[\mathsf{P}(\boldsymbol{k})\left(\widehat{\boldsymbol{u}\times\boldsymbol{\omega}}+\hat{b}\boldsymbol{e_z}\right)\right]\mathrm{e}^{\nu\boldsymbol{k}^2t}, \tag{2.4a}$$

$$\frac{\partial\hat{b}\mathrm{e}^{D\boldsymbol{k}^2t}}{\partial t}=\left[-\mathrm{i}\boldsymbol{k}\cdot\widehat{b\boldsymbol{u}}-N^2\hat{w}\right]\mathrm{e}^{D\boldsymbol{k}^2t}. \tag{2.4b}$$

Originally, time advancement was performed with a second order Adams–Bashforth numerical scheme but we have now implemented a classical fourth-order Runge–Kutta scheme. The nonlinear terms in brackets in (2.4) are computed from $\hat{\boldsymbol{u}}$ and $\hat{b}$ by performing the following steps:

1. we evaluate the vorticity in spectral space $\hat{\boldsymbol{\omega}}=\mathrm{i}\boldsymbol{k}\times\hat{\boldsymbol{u}}$.
2. we apply backward Fourier transforms to the spectral terms $\hat{\boldsymbol{u}}$, $\hat{\boldsymbol{\omega}}$ and $\hat{b}$ to obtain $\boldsymbol{u}$, $\boldsymbol{\omega}$ and b in the physical space.
3. we evaluate the nonlinear terms $\boldsymbol{u}\times\boldsymbol{\omega}$ and $b\boldsymbol{u}$ in physical space.
4. A forward Fourier transforms is applied to the physical terms $\boldsymbol{u}\times\boldsymbol{\omega}$ and $b\boldsymbol{u}$ to obtain $\widehat{\boldsymbol{u}\times\boldsymbol{\omega}}$ and $\widehat{b\boldsymbol{u}}$ in the spectral space.
5. we evaluate the first nonlinear term $\mathsf{P}(\boldsymbol{k})\left(\widehat{\boldsymbol{u}\times\boldsymbol{\omega}}+\hat{b}\boldsymbol{e_z}\right)$ in spectral space.
6. we evaluate the second nonlinear term $-\mathrm{i}\boldsymbol{k}\cdot\widehat{b\boldsymbol{u}}-N^2\hat{w}$ in spectral space.

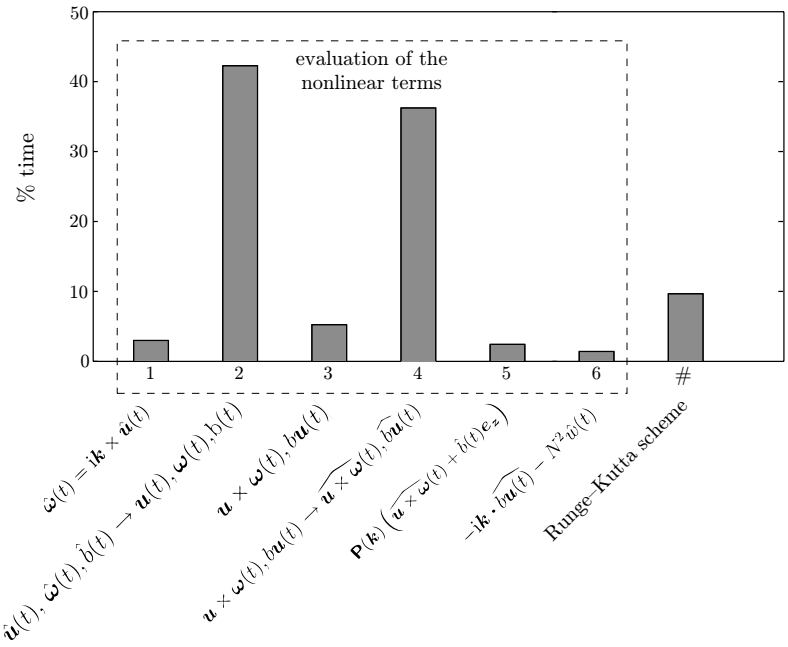

Figure 2.1: Percentage of time spent at each step of the pseudo-spectral algorithm described in § 2.2. We indicate the operation for each step. The timing was done for a run of a simulation of size $N = 256 \times 256 \times 256$ with the FFT library FFTW 3.2 run on a single 3.6GHz Intel Xeon processor. The elapsed times were determined with the Fortran function "system_clock".

2.3 Sequential execution

Before going into the parallelization, it is first important to identify the sections of the program that are taking most of the resources in order to optimize them. Figure 2.1 shows the percentage of time spent at each step of the algorithm described in § 2.2 for a typical simulation of dimension $N = 256 \times 256 \times 256$ run on a single 3.6GHz Intel Xeon processor. We see that 42+36=78% of the time is spent at steps 2 and 4 of the evaluation of the nonlinear terms. These steps correspond to Fourier Transforms between physical and spectral spaces that are performed with a Fast-Fourier Transform (FFT) algorithm. One FFT requires $O(N \log N)$ operations whereas all the other steps involved in the pseudo-spectral algorithm need only $O(N)$ operations. This explains why the FFTs of a pseudo-spectral code are the most time–consuming and become increasingly critical for large simulations.

Figure 2.2 shows the speed of a few FFT libraries for a FFT of size $N = 256 \times 256 \times 256$ performed on a single 3.6GHz Intel Xeon processor. The different libraries have extremely different speeds: on this example, the highly opti-

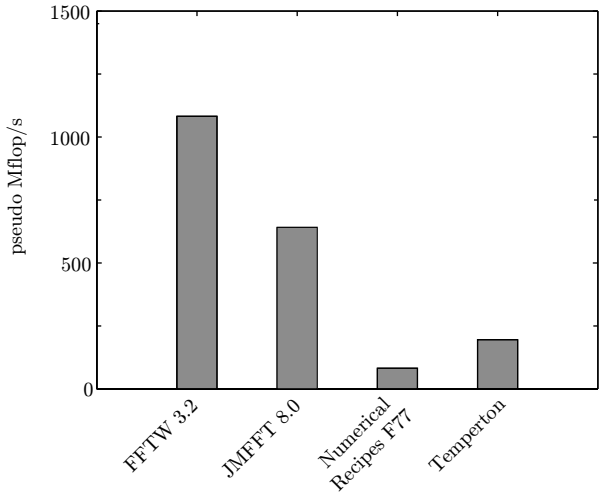

Figure 2.2: Comparison of the performances of different FFT libraries for one real–complex FFT of size $N = 256 \times 256 \times 256$ performed on a single 3.6GHz Intel Xeon processor. The performance is given in pseudo Mflop/s defined as $\frac{5/2N\log_2(N)}{\text{runtime}}$. Higher is better.

mized FFTW 3.2 library is 13 times faster than the naive Numerical Recipes library (1082 Mflops compared to 82 Mflops). As already emphasized the choice of the FFT library is critical for the overall performances of the pseudo-spectral algorithm. It is thus important to determine the fastest (or at least a reasonably fast) library on each computer for a given dimension N. After benchmarking several libraries (FFTW 3.2, JMFFT 8.0, Temperton, Numerical Recipes F77, ESSL, MathKeisan, Intel MKL), we found that FFTW 3.2 was always the fastest (or almost) library on scalar processors (x86, IBM Power) and that the MathKeisan library was the fastest on the NEC-SX vector processors.

2.4 Parallelization of the NS3D code

In the present dissertation, we have performed numerical simulations with a large number of collocation points, up to $N = 1440 \times 1440 \times 192$ in chapter 7. These large simulations require much computing time and memory, which makes necessary the use of parallel computers. This has required the parallelization of the NS3D code since the original version was only sequential. We present below the two types of parallelization that have been implemented. Three different parallel computers have been used:

- "Tournesol": - SGI Altix 450 cluster based at LadHyX.
  - 16 × 1.6GHz dual-core Intel Itanium processors (32 cores).
  - 128 Go of shared memory.

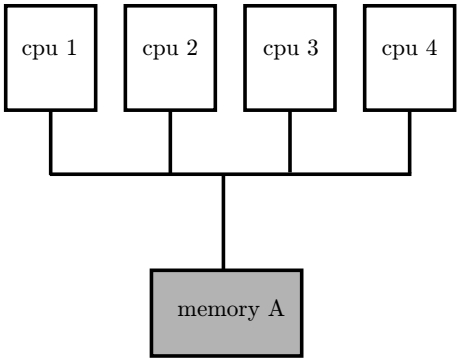

Figure 2.3: A shared memory architecture: all the processors can access all the memory.

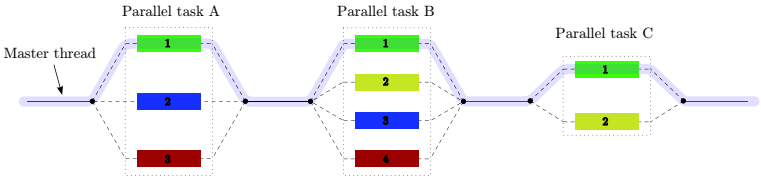

Figure 2.4: An illustration of multi-threading: the master thread forks off a number of threads which execute blocks of code in parallel. (source: Wikipedia)

- "Zahir": - IBM Regatta cluster based at IDRIS.
  - 1024 × 1.3/1.7GHz IBM Power4 processors.
  - 3136 Go of distributed/shared memory.
- "Brodie": - NEC cluster based at IDRIS.
  - 80 × 2GHz SX-8 NEC processors.
  - 640 Go of distributed/shared memory.

2.4.1 Shared memory parallelism

Shared memory parallel computers have the ability for all processors to access all the memory as a global address space as shown in figure 2.3. For that reason, shared memory parallelism is usually very easy to implement since the programmer does not have to care about the locality of the memory. In this architecture, parallelism is often achieved with a multi-threading paradigm such as OpenMP or POSIX Threads. As illustrated in figure 2.4, a master thread "forks" a specified number of slave threads which execute sections of code in parallel.

The three-dimensional FFT algorithm is well adapted for parallelization. Indeed, a three-dimensional FFT of total size $N = N_x \times N_y \times N_z$ is done by first

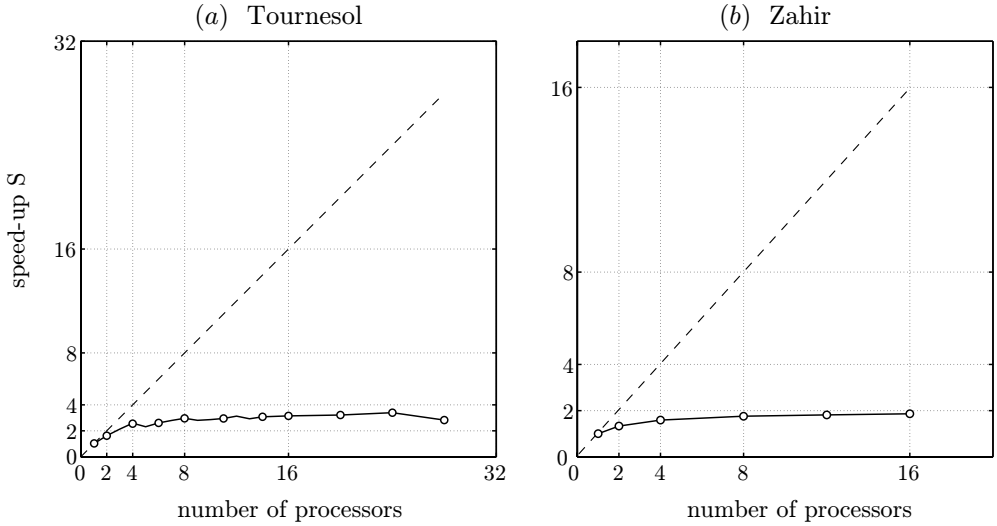

Figure 2.5: Speed-up S of the NS3D code parallelized with multi-threading on (a) Tournesol and (b) Zahir. The ideal linear speed-up is shown in dashed line. The size of the simulation is $N = 256 \times 256 \times 256$. The FFT library is the multi-threaded version of FFTW 3.2.

performing a sequence of $N_y \times N_z$ one-dimensional FFTs of size N_x along the x-direction. Then, $N_x \times N_z$ transformations of size N_y are performed along the y-direction and finally $N_x \times N_y$ transformations of size N_z along the z-direction. At each step, the one-dimensional FFTs are computed independently allowing to distribute them among the different processors. Most of the FFT libraries propose a parallel version based on multi-threading. This is the case of the FFTW 3.2 library used on Tournesol and Zahir or the MathKeisan library used on Brodie. This is very interesting since most of the cpu time is spent by the FFT subroutines as emphasized in § 2.3.

The efficiency of a parallel algorithm can be estimated by its speed-up $S = T_s/T_p$ where T_s is the time taken by the sequential algorithm and T_p the time taken by the corresponding parallel algorithm. Ideal speed-up should be linear i.e. a speed-up of p using p processors. Figure 2.5(a) shows the speed-up obtained for the NS3D code on Tournesol for a number of processors from 1 to 28 and using the multi-threaded version of the FFT library FFTW 3.2. We see a good speed-up up to 4 processors ($S = 2.48$) and then there is almost saturation of the speed-up when more processors are used: $S = 2.83$ with 28 processors. Tournesol is a Non-Uniform Memory Access (NUMA) computer where the memory access time depends on the memory location relative to a processor. As shown by figure 2.6, the processors are grouped into nodes of 4 processors that have a fast uniform memory access within the node but a slower non-uniform memory access with the other nodes.

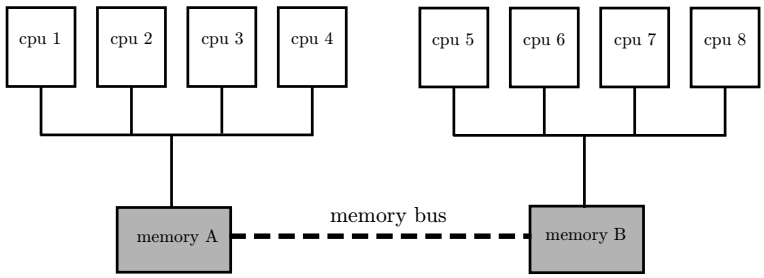

Figure 2.6: An illustration of the non-uniform memory access of Zahir: the processors are grouped into nodes of 4 processors. The memory access is uniform within each node but non-uniform between different nodes.

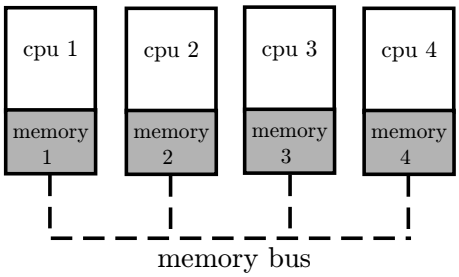

Figure 2.7: A distributed memory architecture: each processor has its own memory.

The data exchange impacts dramatically the performances of the code when the communication time becomes important compared to the calculation time. This clearly happens for Tournesol when using different nodes because they are connected with a relatively slow communication bus. The communication overhead depends on the specific architecture of each computer. For instance, on Zahir, the speed-up obtained is only $S = 1.59$ with 4 processors and the best value is limited to $S = 1.86$ with 16 processors (see figure 2.5*b*). The saturation of the speed-up for a large number of processors limits dramatically the size of the simulations that can be performed with shared memory parallelism.

2.4.2 Distributed memory parallelism

To overcome the difficulty encountered with shared memory parallelism, we have developed another parallelization of the NS3D code based on a distributed memory algorithm. In this case, there is no concept of global address space and each processor has its own memory as shown in figure 2.7.

On such architectures, parallelism is usually achieved through the use of Message Passing Interface (MPI). In this paradigm, the data structure is split up and resides as "slices" in the local memory of each task. All the tasks work

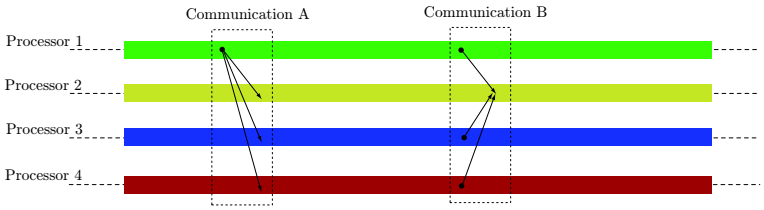

Figure 2.8: The Message Passing Interface (MPI) paradigm: all the tasks run concurrently and exchange data through different types of communications.

concurrently and exchange data through communications by sending and receiving "messages" as illustrated in figure 2.8. Compared to shared memory, the implementation is more complex because we have to define explicitly the distribution of the whole data among the processors as well as each data communication. However, better performances are usually expected because each processor works only on its local memory and data communications are limited to what is strictly required by the parallel algorithm.

We outline here the implementation of an MPI parallelization of NS3D code. If we consider a simulation running on a computer with p processors, the data in physical space are stored in the "natural" order $(x, y, z*)$ where the star indicates that the z-direction is distributed among the p processors. It means that each processor has a data slice of size $N_x \times N_y \times N_z/p$ for a simulation of total size $N_x \times N_y \times N_z$.

We recall here that Fortran stores data in column-major order meaning that contiguous elements in memory correspond to the first dimension of an array. Accessing array elements that are contiguous in memory is much faster than accessing elements which are not, due to caching. This is important when implementing the FFT algorithm in parallel. We describe below briefly its main steps on a forward FFT:

1. Each processor performs a sequence of $N_y \times N_z/p$ one-dimensional FFTs of size N_x along the local x-direction. At this step, the array is in the order $(x, y, z*)$ so the data in the x-direction are stored contiguously ensuring a fast memory access.

2. Each processor transposes the data between the local first and second dimensions: $(x, y, z*) \rightarrow (y, x, z*)$.

3. Each processor performs a sequence of $N_x \times N_z/p$ one-dimensional FFTs of size N_y along the local y-direction. Thanks to the transpose of the previous step, the array is in the order $(y, x, z*)$ ensuring again a fast memory access.

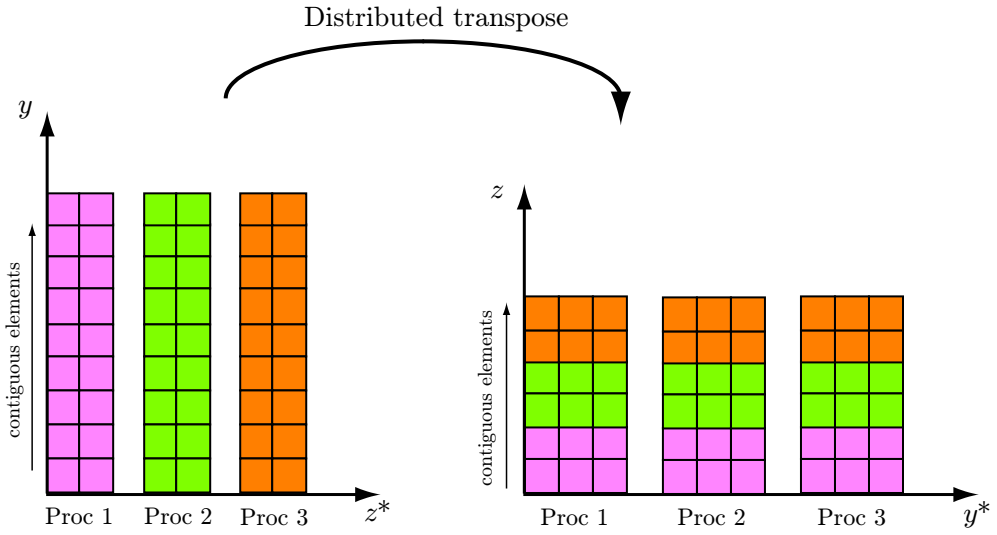

Figure 2.9: Schematic of a distributed transpose with $p = 3$ processors on a two-dimensional array of total size $N_y \times N_z = 9 \times 6$. The array is initially in the order $(y, z*)$: the data are distributed along the z-direction and the y-direction corresponds to contiguous elements in memory. The distributed transpose ends up with an array in the order $(z, y*)$: the data are distributed along the y-direction and the z-direction corresponds to contiguous elements in memory.

4. We perform a distributed transpose of the data between the processors. This is done through a communication of type "MPI_alltoall" that distributes the data along the y-direction in the order $(z, x, y*)$ i.e. each processor has a data slice of size $N_z \times N_x \times N_y/p$. This distributed transpose between directions y and z is illustrated schematically on figure 2.9.

5. Each processor performs a sequence of $N_x \times N_y/p$ one-dimensional FFTs of size N_z along the local z-direction. At this step, the array is in the order $(z, x, y*)$ ensuring again a fast memory access.

This parallel transposed FFT algorithm gives the Fourier transform of the original data but transposed from $(x, y, z*)$ directions into $(z, x, y*)$. We have not implemented an extra distributed transpose to retrieve the original order because this would have required time–costly extra communications. All the other steps of the pseudo-spectral algorithm are simply performed point by point in both physical space and spectral space and makes use only of the local data of each processor. These portions are easy to implement and so we will not give more details here. The communications are thus limited to the distributed transpose performed in the FFT. This makes the distributed memory parallelization well adapted to the pseudo-spectral algorithm.

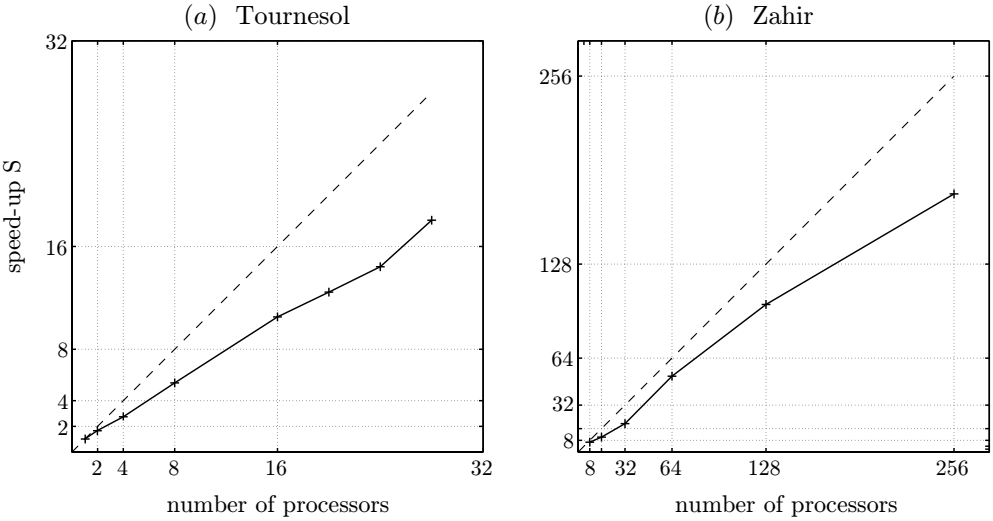

Figure 2.10: Speed-up S of the NS3D code parallelized with MPI on (a) Tournesol and (b) Zahir. The ideal linear speed-up is shown in dashed line. The size of the simulation is $N = 256 \times 256 \times 256$. The FFT library is FFTW 3.2.

Figure 2.10 shows the speed-up S obtained for the NS3D code on Tournesol and Zahir for a number of processors from 1 to 256 with an MPI parallelization. The speed-up remains excellent even for a large number of processors: we obtain $S = 18.04$ for 28 processors on Tournesol and $S = 176.41$ for 256 processors on Zahir. Therefore, MPI parallelism allows to run large simulations with a large number of processors, in contrast with shared memory parallelism.

Chapter 3

Three-dimensional stability of a horizontally sheared flow in a stably stratified fluid

Article published in the *Journal of Fluid Mechanics*, **570**, 297–305 (2007).

Three-dimensional stability of a horizontally sheared flow in a stably stratified fluid

By AXEL DELONCLE, JEAN-MARC CHOMAZ AND PAUL BILLANT

Hydrodynamics Laboratory (LadHyX), Ecole Polytechnique,
91128 Palaiseau Cedex, France
axel.deloncle@ladhyx.polytechnique.fr

(Published in the *Journal of Fluid Mechanics*, vol.570, pp.297–305)

This paper investigates the three-dimensional stability of a horizontal flow sheared horizontally, the hyperbolic tangent velocity profile, in a stably stratified fluid. In a homogeneous fluid, Squire theorem states that the most unstable perturbation is two-dimensional. When the flow is stably stratified, this theorem does not apply and we have performed a numerical study to investigate the three-dimensional stability characteristics of the flow. When the Froude number, F_h, is varied from ∞ to 0.05, the most unstable mode remains two-dimensional. However, the range of unstable vertical wavenumbers widens proportionally to the inverse of the Froude number for $F_h \ll 1$. This means that the stronger the stratification, the smaller the vertical scales that can be destabilized. This loss of selectivity of the two-dimensional mode in horizontal shear flows stratified vertically may explain the layering observed numerically and experimentally.

3.1 Introduction

Because of its importance in industrial and geophysical applications, the evolution of shear flows has been often studied (Ho & Huerre 1984). The basic case of a flow in a homogeneous fluid is well known. Squire's theorem (Squire 1933) states that any three-dimensional unstable mode is less unstable than two-dimensional modes, implying that shear flows are dominated by two-dimensional instabilities. Necessary conditions for their existence are given by Rayleigh's inflection point criterion (Rayleigh 1887) and Fjørtoft's criterion (Fjòrtoft 1950) on the basic velocity profile in the inviscid case. Howard (1961) also showed that the temporal growth rate of two-dimensional perturbations is confined inside a semi-circle in the complex plane.

Much attention has also been devoted to the situation of a vertical shear in a stably stratified fluid. Miles (1961) and Howard (1961) established a sufficient condition for stability as $Ri > 1/4$ with $Ri = N^2/S^2$, the Richardson number, where N is the Brunt–Väisälä frequency and S the shear rate.

In contrast, the case of a nonvertical shear in a vertically stratified fluid has been little addressed. Blumen (1970) extended the application of Howard's semicircle theorem for hydrostatic perturbations in a stratified fluid for an arbitrary orientation of the shear.

However, the Squire theorem does not hold for such flows, meaning that it is not at present known whether two-dimensional perturbations dominate the dynamics of a stratified sheared flow. In order to address this question, we investigate the three-dimensional linear stability of a purely horizontal mixing layer, the hyperbolic-tangent velocity profile, in a vertically stratified fluid.

The paper is organized as follows. In § 3.2.1, the governing equations as well as the basic state are presented. In §§ 3.2.2 and 3.2.3, we give the linearized equations and outline the numerical method. Section 3.3 is devoted to the results for different stratifications. Concluding remarks follow in § 3.4.

3.2 Problem formulation

3.2.1 The governing equations and the basic state

The flow is assumed to be inviscid non-diffusive stably stratified and to satisfy the Boussinesq approximation for the Euler equations:

$$\frac{\mathrm{D}\boldsymbol{u}}{\mathrm{D}t} = -\frac{1}{\rho_0}\boldsymbol{\nabla} p + b\boldsymbol{e}_z, \tag{3.1}$$

$$\boldsymbol{\nabla}\cdot\boldsymbol{u} = 0, \tag{3.2}$$

$$\frac{\mathrm{D}b}{\mathrm{D}t} + N^2 w = 0, \tag{3.3}$$

where $\boldsymbol{u} = (u, v, w)$ is the velocity vector in Cartesian coordinates, ρ_0 a constant reference density, p the pressure, $b = -g\rho'/\rho_0$ the buoyancy with ρ' the density perturbation with respect to the mean density $\overline{\rho}$, g the gravity and $\boldsymbol{e}_z$ the unit vector in the upward z-direction. $N = \sqrt{-g/\rho_0\,\mathrm{d}\overline{\rho}/\mathrm{d}z}$ is the Brunt–Väisälä frequency assumed here to be constant.

We investigate the stability of a purely horizontal flow, the hyperbolic-tangent velocity profile whose shear is in the y-direction (figure 3.1):

$$\boldsymbol{U}(y) = U(y)\,\boldsymbol{e}_x = U_0 \tanh\left(\frac{y}{L}\right)\boldsymbol{e}_x, \tag{3.4}$$

where U_0 and L are, respectively, the velocity and length scales of the base flow and $\boldsymbol{e}_x$ is the unit vector in the x-direction.

In the following, length and time scales are nondimensionalized such that $L = 1$ and $U_0 = 1$. The basic state becomes $U(y) = \tanh y$. For simplicity, the same notation is kept for the dimensionless variables.

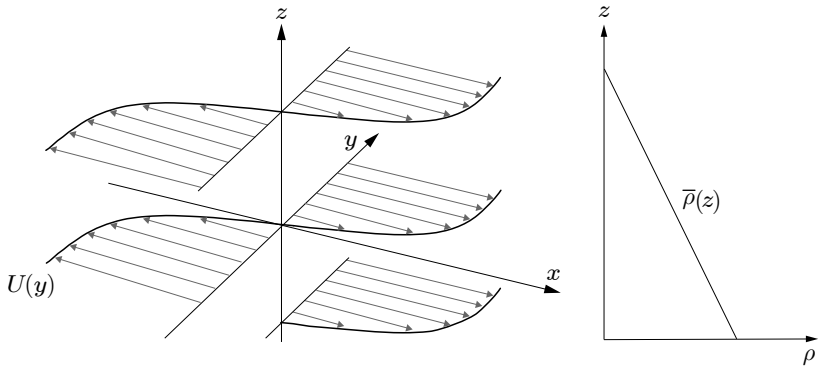

Figure 3.1: Sketch of the base flow. The hyperbolic-tangent velocity profile is horizontal with a velocity in the x-direction sheared in the y-direction and uniform in the z-direction. The fluid is stably stratified in the vertical z-direction.

3.2.2 Linearized equations

Since the basic state is uniform along the x- and z-axis, we consider infinitesimal perturbations of the form

$$[\tilde{\boldsymbol{u}}\,;\,\tilde{p}\,;\,\tilde{b}](x,y,z,t) = [\boldsymbol{u}\,;\,p\,;\,b](y)\,\mathrm{e}^{\mathrm{i}k_x x+\mathrm{i}k_z z+\sigma t} + \text{c.c.}, \tag{3.5}$$

where σ is the growth rate, k_x and k_z the wavenumbers along directions x and z, and c.c. denotes the complex conjugate.

For unbounded velocity profiles, the boundary conditions correspond to vanishing perturbations at infinity:

$$\lim_{y\to\pm\infty}[\boldsymbol{u}\,;\,p\,;\,b](y) = [0\,;\,0\,;\,0]. \tag{3.6}$$

The linearized equations for the perturbation quantities can be written in terms of u, v and b by eliminating the vertical velocity w and the pressure p:

$$\mathsf{A}\begin{pmatrix}u\\v\\b\end{pmatrix} = \sigma\mathsf{B}\begin{pmatrix}u\\v\\b\end{pmatrix}, \tag{3.7}$$

where

$$\mathsf{A} = \begin{pmatrix} 0 & \mathrm{i}k_x\left\{U(\mathrm{D}^2-k^2)-\mathrm{D}^2U\right\} & \mathrm{i}k_z\mathrm{D} \\ \mathrm{i}k_x(\mathrm{D}U+U\mathrm{D}) & \mathrm{D}^2U+k_x^2U+\mathrm{D}U\,\mathrm{D} & 0 \\ \mathrm{i}k_x/F_h^2 & \mathrm{D}/F_h^2 & k_xk_zU \end{pmatrix}, \tag{3.8}$$

$$\mathsf{B} = \begin{pmatrix} 0 & k^2-\mathrm{D}^2 & 0 \\ -\mathrm{D} & \mathrm{i}k_x & 0 \\ 0 & 0 & \mathrm{i}k_z \end{pmatrix}, \tag{3.9}$$

and where $k^2 = k_x^2+k_z^2$, $\mathrm{D} = \mathrm{d}/\mathrm{d}y$ and $F_h = U_0/LN$ is the horizontal Froude number. This matrix form is convenient for solving the problem numerically.

3.2.3 Numerical procedure

The three-dimensional stability of the hyperbolic-tangent profile is determined by computing all the eigenvalues of the matrix operator (3.7).

Because the domain of study $y \in]-\infty, \infty[$ is unbounded, an algebraic transformation $\tilde{y} = y/\sqrt{1+y^2}$ is first used to map the infinite interval of y to a finite one $\tilde{y} \in]-1, 1[$. The two operators A and B are then discretized using a set of Q Chebyshev polynomials interpolated on Gauss–Lobatto collocation points. The algebraic mapping in conjunction with the Chebyshev polynomials leads to the so-called *rational Chebyshev functions* (Grosch & Orszag 1977; Boyd 2001).

The discretized version of the eigenvalue problem (3.7) is finally solved by calling the eigensolver *eig* of Matlab. To eliminate the spurious modes which are not physically relevant, two discretizations with different numbers $Q_1 = 297$ and $Q_2 = 369$ of Chebyshev polynomials are used. We keep only the eigenvalues whose relative variation between the two discretizations is less than 0.01.

3.3 Results

To describe the general properties of the stability problem, it is more convenient to obtain a single equation for v from the linearized equations:

$$\mathrm{D}\left(\frac{\mathrm{D}v}{\tilde{k}^2}\right) - \left[\frac{\mathrm{i}k_x}{s}\mathrm{D}\left(\frac{\mathrm{D}U}{\tilde{k}^2}\right) + 1\right] v = 0, \tag{3.10}$$

where $s = \sigma + \mathrm{i}k_x U$ and $\tilde{k}^2 = k_x^2 + F_h^2 s^2 k_z^2/(F_h^2 s^2 + 1)$.

First, we can see that if σ is an eigenvalue of (3.10) for given wavenumbers (k_x, k_z), then it is also an eigenvalue for $(k_x, -k_z)$ while $-\sigma$ is an eigenvalue for $(-k_x, k_z)$. Therefore, positive k_x and k_z only can be studied without loss of generality.

When the fluid is homogeneous ($F_h = \infty$), we have $\tilde{k}^2 = k^2$ so that equation (3.10) reduces to the Rayleigh equation

$$\mathrm{D}^2 v - \left[\frac{\mathrm{i}k_x}{s}\mathrm{D}^2 U + k^2\right] v = 0. \tag{3.11}$$

We see from equation (3.11) that the growth rate can be sought in the form $\sigma = k_x f(k)$, where $f(k)$ is a function of $k = \sqrt{k_x^2 + k_z^2}$ only. This implies the well-known Squire transformation (Schmid & Henningson 2001), i.e. the growth rate and the eigenmode of a three-dimensional perturbation $k_z \neq 0$ can be deduced that of a two-dimensional perturbation $k_z = 0$. It implies also that any three-dimensional disturbance with wavenumbers (k_x, k_z) having a growth rate σ^{3D} has a corresponding two-dimensional disturbance $(\sqrt{k_x^2 + k_z^2}, 0)$ with

a larger growth rate $\sigma^{2D} = \sigma^{3D}\sqrt{k_x^2 + k_z^2}/k_x$. Since the hyperbolic tangent profile is neutral for wavenumbers $(k_x = 1, k_z = 0)$ the Squire theorem also implies that all perturbations with $k_x^2 + k_z^2 = 1$ are neutral. In the homogeneous case, it is also possible to prove the Rayleigh criterion from (3.11); a necessary condition of instability is that the velocity profile $U(y)$ has an inflection point, i.e. D^2U changes sign.

Figure 3.2(a) shows the growth rate of a two-dimensional disturbance as a function of its horizontal wavenumber k_x in the case of a homogeneous fluid. These results are in agreement with those of Michalke (1964) (diamonds in figure 3.2a). In particular, the growth rate is purely real with a maximum amplification, $\sigma_{max} = 0.1897$, occurring at $k_{xmax} = 0.4449$. The relative error does not exceed 1‰ except for the neutral mode around $k_x = 1$. This slight difference is due to the presence of a regular singularity at $y = 0$ in the neutral eigenmodes at $k_x = 1$. As our primary interest is the effect of the stratification on unstable modes, we have made no provision for keeping track of these singularities. The general case of a three-dimensional disturbance in a homogeneous fluid has been computed directly and is presented in figure 3.2(b). The most unstable mode is two-dimensional, in agreement with the Squire's transformation. The unstable domain in the (k_x, k_z)-plane is inside the neutral curve $k_x^2 + k_z^2 = 1$ (dashed line) in agreement with the Squire transformation.

In the stratified case, the classical theorems are not valid. The Squire transformation no longer applies for equation (3.10) in the case $F_h \neq \infty$ so that three-dimensional modes may possibly be more unstable than two-dimensional modes. In the stratified case, equation (3.10) shows that the Rayleigh inflection point criterion is only a necessary condition for two-dimensional perturbation, but not for three-dimensional perturbations. This leaves open the possibility for a horizontally sheared flow without an inflection point to be unstable to three-dimensional modes, but such a counter example to the Rayleigh criterion has not yet been found. In any case, the three-dimensional stability properties cannot be inferred from the two-dimensional results when the flow is stratified; they have to be computed numerically.

The task is slightly more involved than in the homogeneous case when $F_h \neq \infty$ because other regular singularities are present when $s = \pm\mathrm{i}/F_h$ and $s = \pm\mathrm{i}k_x/(F_h k)$ in addition to the singularity at $s = 0$. In nondimensional form, these extra singularities correspond to a Doppler shifted frequency $\mathrm{i}\sigma - k_x U$ equal to the Brunt–Väisälä frequency and to the frequency of internal gravity waves, respectively. Moreover, it can be shown that the two solutions of equation (3.10) are analytic at the critical point $s = \pm\mathrm{i}k_x/(F_h k)$, but only one solution is analytic at $s = \pm\mathrm{i}/F_h$. These additional singularities might explain why the computations become difficult and require higher spatial resolution for small growth rates when the fluid is stratified.

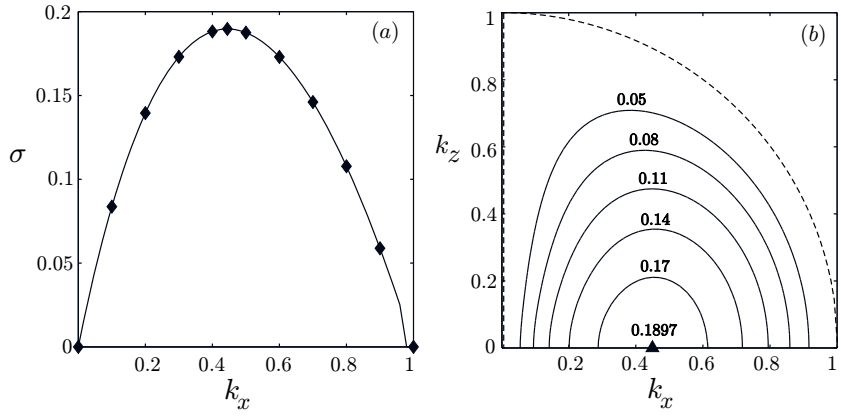

Figure 3.2: Homogeneous fluid. (a) Growth rate σ of a two-dimensional disturbance as a function of its wavenumber k_x; the results of Michalke (1964) are also plotted with ⧫. (b) Contours of growth rate σ of a three-dimensional disturbance as a function of its horizontal k_x and vertical k_z wavenumbers; ▲ indicates the most unstable mode. The unstable domain is bounded by neutral modes deduced from the Squire's transformation and plotted as a dashed line.

Figures 3.3 is similar to figure 3.2(b), but in stratified cases. The figure shows the growth rate contours in the (k_x, k_z)-plane for Froude numbers from $F_h = 10$ down to $F_h = 0.05$. In all four cases, the most amplified mode remains two-dimensional as in the homogeneous case. However, by paying attention to the vertical wavenumber range, we see that the unstable domain expands towards extremely large k_z as F_h decreases making the unstable domain strongly anisotropic when F_h is small. Moreover, we see that the contours in figure 3.3(b)-3.3(d) have the same shape and differ only by their vertical wavenumber range, suggesting a self-similarity law.

The growth rate for the most unstable streamwise wavenumber $k_{xmax} = 0.4449$ is plotted as a function of k_z in figure 3.4(a) for different stratifications F_h. The curve of σ as a function of k_z widens dramatically for small F_h. This implies that the selectivity of the two-dimensional modes strongly decreases with F_h, meaning that a broad range of vertical scales can develop in such a flow. For example, the growth rate for $F_h = 0.05$ at $k_z = 10$ is only 20% smaller than that for the two-dimensional mode.

Figure 3.4(b) presents the same growth rate curve as figure 3.4(a), but plotted versus $F_h k_z$. As already anticipated from figure 3.3, the growth rate contours collapse when represented as a function of $F_h k_z$. The growth rates for $F_h = 0.1$ and $F_h = 0.05$ are indiscernible. This self-similarity implies that the growth rate is a function of $F_h k_z$ and not F_h and k_z separately, i.e.

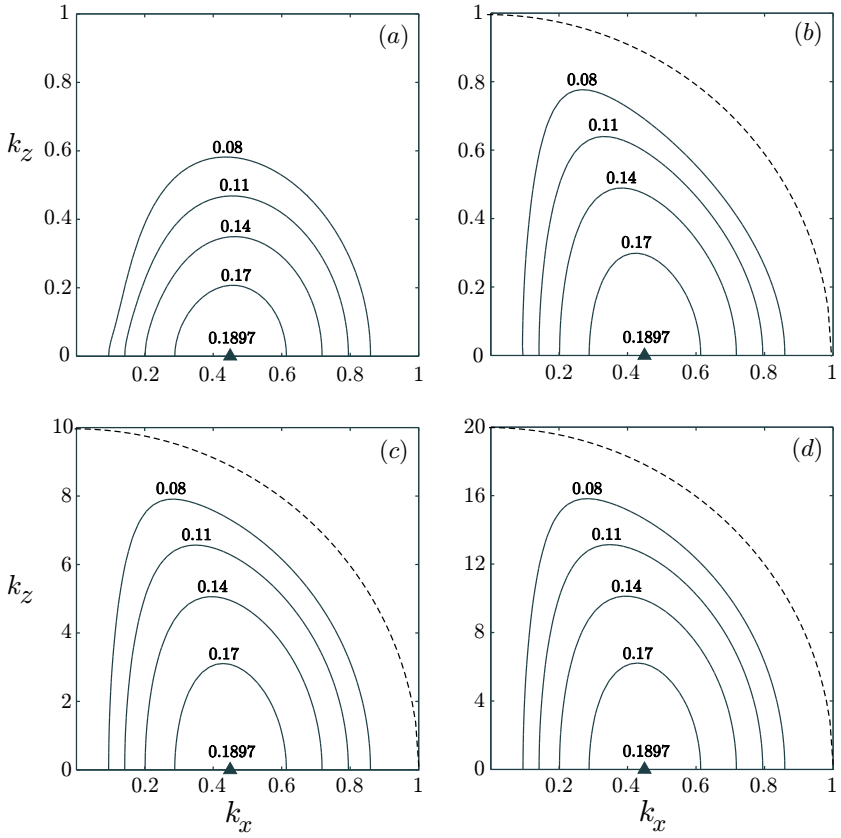

Figure 3.3: As figure 3.2(b), but in a stratified fluid. Increasing stratifications are presented: (a) $F_h = 10$, (b) $F_h = 1$, (c) $F_h = 0.1$ and (d) $F_h = 0.05$. The boundaries of the unstable domain valid for strong stratifications ($F_h \ll 1$) are also plotted as a dashed line for (b)–(d).

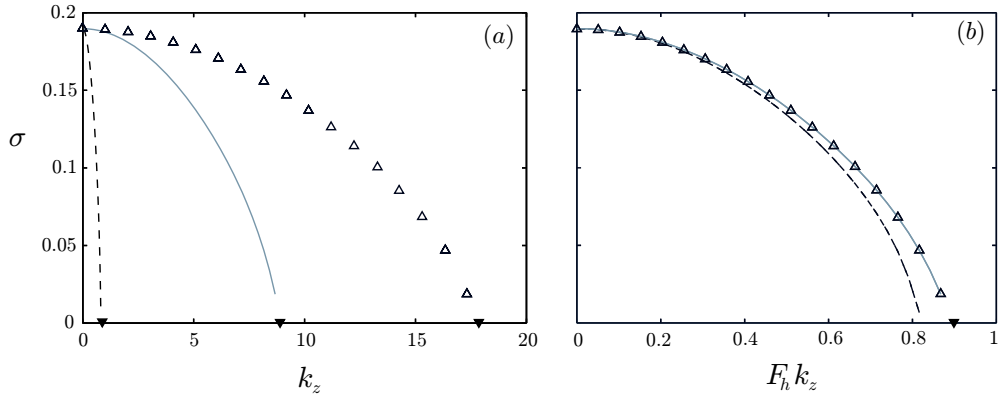

Figure 3.4: Growth rate as a function of (a) the vertical wavenumber k_z and (b) the rescaled vertical wavenumber $F_h k_z$ for the most unstable two-dimensional wavenumber $k_{xmax} = 0.4449$. Three stratifications are plotted $F_h = 1$ (dashed line), $F_h = 0.1$ (solid line) and $F_h = 0.05$ (△). The neutral modes given by equation (3.13) for strong stratifications are also plotted with ▼.

$\sigma(k_x, k_z, F_h) = \tilde{\sigma}(k_x, F_h k_z)$ for $F_h \leq 1$. This result is a generic feature valid for any strongly stratified flow as shown by Billant & Chomaz (2001).

For strong stratifications, this self-similarity may be proved for the neutral curve. First, we can see in equation (3.10) that the modes along the $k_x = 0$ axis remain neutral. Moreover, for strong stratifications ($F_h \ll 1$), we have at leading order $\tilde{k}^2 \simeq k_x^2 + F_h^2 s^2 k_z^2$, which is equivalent to the hydrostatic approximation. Following Blumen (1970), the neutral modes ($\sigma = 0$) of equation (3.10) are then:

$$v = k_x \mathrm{sech}^{k_x^2} y, \tag{3.12}$$

where k_x verifies the condition:

$$k_x^2 + (F_h k_z)^2 = 1. \tag{3.13}$$

The latter condition is similar to the one valid in a homogeneous fluid $k_x^2 + k_z^2 = 1$, except that the vertical wavenumber has been rescaled by F_h. The boundaries of the unstable domain are plotted with dashed lines in figure 3.3(b)–3.3(d).

3.4 Conclusion

We have investigated the three-dimensional instability of the hyperbolic tangent velocity profile. In homogeneous fluid, the Squire theorem tells us that

three-dimensional perturbations are always less unstable than two-dimensional ones. When the shear is horizontal and the fluid is vertically stratified, the theorem does not apply and we have determined numerically the three-dimensional stability of this particular shear flow.

Five different Froude numbers F_h have been studied, from a homogeneous fluid to a strongly stratified fluid. In all cases, the most unstable mode remains two-dimensional, but the stratification has been found to destabilize a broad range of three-dimensional modes whose extent increases in inverse proportion to F_h. Both the numerical results and an asymptotic analysis show that the unstable domain in the (k_x, k_z)-plane becomes strongly anisotropic with a neutral boundary that is no longer a circle $k_x^2 + k_z^2 = 1$ as in the homogeneous case, but an elongated ellipse $k_x^2 + (F_h k_z)^2 = 1$. When $F_h \leq 1$, numerical results show that the growth rate converges to a universal curve $\sigma(k_x, k_z, F_h) = \tilde{\sigma}(k_x, F_h k_z)$ function of the rescaled vertical wavenumber $F_h k_z$ rather than F_h and k_z separately. This decrease of the characteristic vertical length as F_h is in agreement with the self-similarity found by Billant & Chomaz (2001). In practice, our analysis shows that all the three-dimensional modes with k_z smaller than $1/F_h$ have a growth rate similar to the two-dimensional modes.

The selectivity of the two-dimensional instability is therefore dramatically decreased when the stratification is increased. This property might explain the results of the numerical simulations of Basak & Sarkar (2006) where a horizontal mixing layer is initially perturbed by a large-amplitude noise. The flow evolves into pancake vortices with a vertical correlation length scale that decreases with stratification. This vertical scale selection is reminiscent of the increase of the width of the unstable vertical wavenumber band predicted by the present stability analysis when F_h decreases. Indeed three-dimensional perturbations with a wavenumber in the x-direction equal to the most unstable two-dimensional wavenumber but with a vertical wavenumber k_z scaling as $1/F_h$, will grow as fast as the two-dimensional perturbation. Such a perturbation will induce a vertical deformation of the shear layer out of phase every half wavelength π/k_z on the vertical and therefore leads to a roll-up resulting in a pattern of vortices staggered on the vertical very similar to those observed in Basak & Sarkar (2006).

The layering observed by Praud *et al.* (2005) in the early evolution of the flow produced by towing a rake of vertical flat plates might result from a similar destabilization of large vertical wavenumber for the primary instability of the sheared flow and not from a secondary instability of the primary vortices.

Oceanic currents or atmospheric jets are configurations where horizontal shear is observed (Pedlosky 1982) and the present analysis questions the frequent assumption that such horizontal shear will be unstable to a two-dimensional (barotropic) mode. Instead, we may imagine that the weak selectivity for the two-dimensional mode demonstrated here for stratified flows will

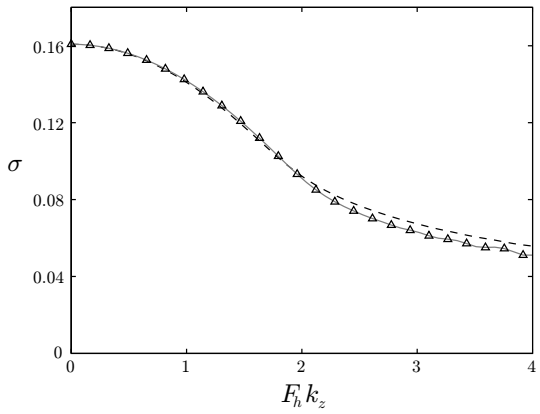

Figure 3.5: Similar to figure 3.4(b) for the Bickley jet $U(y) = \mathrm{sech}^2 y$. Growth rate as a function of the rescaled vertical wavenumber $F_h k_z$ for the most unstable two-dimensional wavenumber $k_{xmax} = 0.9021$. Three stratifications are plotted $F_h = 1$ (dashed line), $F_h = 0.1$ (solid line) and $F_h = 0.05$ ($\triangle$). Only the leading mode, at present even in y, is considered. The odd mode is not presented, but follows a similar trend.

favour the formation of vertically decorrelated layers of thickness proportional to F_h. This conjecture is confirmed by the stability analysis of the Bickley jet. Figure 3.5 presents the instability growth rate of this flow versus the rescaled vertical wavenumber at the horizontal wavenumber corresponding to the most unstable two-dimensional mode (similar to figure 3.4b). The instability growth rate converges toward a unique curve as a function of the rescaled vertical wavenumber $F_h k_z$ in agreement with the proposed self-similarity.

It is interesting to contrast this case of a horizontal shear with the well-known situation of a vertical shear in a stably stratified fluid. As recalled in § 3.1, strong stratification stabilizes vertical shear flow since the associated Richardson number is then larger than 1/4, whereas it destabilizes horizontal shear flow versus perturbations with short vertical wavelength. This suggests that in most realistic situations, a shear flow will be sensitive mainly to the horizontal component of the shear rather than to the vertical one because of this opposing effect of the stratification.

Chapter 4

Stability of vortex arrays in a stratified and rotating fluid: theoretical analysis

Article in preparation for the *Journal of Fluid Mechanics*.

Three-dimensional stability of vortex arrays in a stratified and rotating fluid: theoretical analysis

By AXEL DELONCLE, PAUL BILLANT AND JEAN-MARC CHOMAZ

Hydrodynamics Laboratory (LadHyX), Ecole Polytechnique,
91128 Palaiseau Cedex, France
axel.deloncle@ladhyx.polytechnique.fr

(In preparation for the *Journal of Fluid Mechanics*)

This paper investigates by an asymptotic approach the three-dimensional stability of steady vertical vortex arrays in a stratified and rotating fluid. Three classical vortex arrays are studied: the Kármán vortex street, the symmetric double row and the single row of co-rotating vortices. The analysis assumes well-separated vortices and long-wavelength bending perturbations like in the stability analyses of arrays of vortex filaments in homogeneous fluid. However, the present approach does not rely on the conservation of circulation and is therefore valid in a stratified and rotating fluid.

In a stratified and non-rotating fluid (for $F_h \leq 1$, where F_h is the horizontal Froude number), it is found that the Kármán vortex street for a street spacing ratio (the distance h between the rows divided by the distance b between vortices in the same row) $\kappa \leq 0.41$ and the symmetric double row for any spacing ratio are most unstable to a three-dimensional instability of zigzag type that vertically bends the vortices. The most amplified vertical wavenumber scales like $1/bF_h$ and the growth rate scales with the strain $\Gamma/2\pi b^2$ where Γ is the vortex circulation. For the Kármán vortex street, the zigzag instability is symmetric with respect to the middle plane between the two rows while it is antisymmetric for the symmetric double row. For the Kármán vortex street with well-separated vortex rows $\kappa > 0.41$ and the single row, the dominant instability is two-dimensional and corresponds to a pairing of adjacent vortices of the same row. The main differences between stratified and homogeneous fluids are the opposite symmetry of the dominant three-dimensional instabilities and the scaling of their most amplified wavenumber. When $F_h > 1$, three-dimensional instabilities are damped.

In the presence of background rotation in addition to the stratification, symmetric and antisymmetric modes do not decouple anymore but the dominant instability remains qualitatively the same for the three vortex arrays. However, the most unstable wavenumber of three-dimensional instabilities dramatically decreases with rotation and is shown to scale like Ro/bF_h for small Rossby number Ro in agreement with quasi-geostrophic scaling laws.

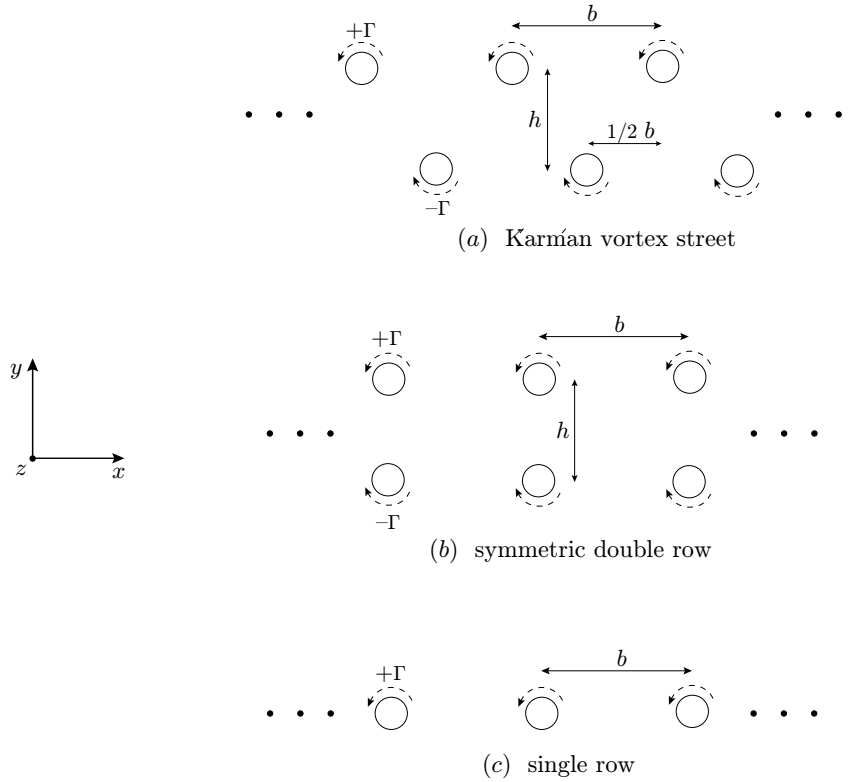

Figure 4.1: Sketch of the three vortex arrays. The vortices are initially two-dimensional with their axis in the vertical $z-$direction. The rows are infinite along the x-axis.

4.1 Introduction

In this article, we investigate the three-dimensional stability in a stratified and rotating fluid of three classical vortex arrays of two-dimensional vertical vortices: (i) the Kármán vortex street which consists in two staggered counter-rotating infinite rows of co-rotating vortices, (ii) the symmetric double row which is similar except that the two rows are not staggered and (iii) the single row of co-rotating vortices (figure 4.1).

Much attention has been devoted to their linear stability in homogeneous fluid using point vortices. This approach is valid for well-separated vortices with a reference length taken as the radius of the vortex core. The case of two-dimensional disturbances was first treated by von Kármán (1911, 1912) and von Kármán & Rubach (1912) who showed that all vortex arrays were always unstable except a single configuration of the Kármán vortex street for which the street spacing ratio (the ratio of the distance h between the two rows

and the separation distance b of the vortices in the same row, see figure 4.1) was equal to 0.281. This analysis is presented in the book of Lamb (1932).

The case of three-dimensional disturbances was later addressed by Robinson & Saffman (1982). Their analysis is based on vortex filaments and is therefore limited to long axial wavelengths and to well-separated vortices as well. Under these hypotheses, they could make use of the Biot–Savart law to compute the induced motion of the vortices and the cut-off approximation to determine the self-induced velocity of the individual vortices. They found that the Kármán vortex street and the symmetric double row are most unstable to three-dimensional or two-dimensional disturbances depending on the spacing ratio of the streets while the single row is always most unstable to two-dimensional disturbances.

The stability of such two-dimensional vortex arrays has been also investigated in a rotating fluid (see for example Leblanc & Cambon 1998; Potylitsin & Peltier 1999). However, it has been little addressed in a stably stratified and rotating fluid even if these configurations can be observed in geophysical flows for instance in the wake of mountains or islands (Kármán vortex street like in Etling 1990) or as the subsequent evolution of the destabilization of a jet (symmetric double row) or a shear layer (single row). Potylitsin & Peltier (1998) have investigated numerically the stability of an infinite vortex row but only in a weakly stratified and rotating fluid. They found that a weak stratification has a stabilizing effect on the elliptic instability. Experiments in a strongly stratified fluid have shown the formation of horizontal layers by the destabilization of the vortex streets created by towing a rake of vertical cylinders (Holford & Linden 1999) or a rake of vertical flat plates (Praud *et al.* 2005). The emergence of pancake vortices from a stratified horizontal shear layer has been also recently studied numerically by Basak & Sarkar (2006).

The stability of a pair of columnar vertical vortices in a stratified fluid has been investigated in the counter-rotating (Billant & Chomaz 2000*a*) and co-rotating (Otheguy *et al.* 2006) cases and showed the existence of a three-dimensional instability called zigzag instability that vertically bends the vortices with little internal deformation. Billant *et al.* (2007) recently derived a general theory to treat the stability of a pair of vortices for long-axial-wavelength bending perturbations and well-separated vortices in a stratified and rotating fluid. Their analysis led to stability equations formally identical to the ones given by Crow (1970) in homogeneous fluid using the Biot–Savart law and the cut-off approximation. Only the expressions of the self-induction and mutual induction functions differ between homogeneous fluid and stratified and rotating fluid. This asymptotic theory gives results in excellent agreement with full numerical stability analysis of the zigzag instability of vortex pairs. In the present paper, we make use of this approach to study the three-dimensional stability of the Kármán vortex street, the symmetric double row and the single

row for long-axial-wavelength perturbations and well-separated vortices in a stratified and rotating fluid.

The paper is organized as follows. In § 4.2.1, we present briefly the analysis of Billant *et al.* (2007) before generalizing it to vortex arrays in § 4.2.2. Section 4.3 is devoted to the stability results of the different vortex arrays in the non-rotating case. The effects of background rotation are presented in § 4.4. Concluding remarks follow in § 4.5.

4.2 Problem formulation

4.2.1 Interactions between a pair of vortices in a stratified and rotating fluid

For clarity, we first present briefly the simple case of two vortices in a stratified and rotating inviscid fluid treated by Billant *et al.* (2007) by means of an asymptotic theory. The generalization to several vortices is straightforward from this case.

We denote Γ_1 and Γ_2, the circulations of the two vertical vortices of radius a separated by a distance b. The Froude and Rossby numbers of each vortex are defined as follows:

$$F_{hi} = \frac{|\Gamma_i|}{2\pi a^2 N}, \quad Ro_i = \frac{\Gamma_i}{4\pi a^2 \Omega_b}, \quad \text{with} \quad i = \{1, 2\}, \tag{4.1}$$

where N is the Brunt–Väisälä frequency and Ω_b is the rotation rate about the vertical axis.

The asymptotic theory is based on two assumptions. First, it is assumed that the strains $\Gamma_i/2\pi b^2$ are small compared to the core vorticities $\Gamma_i/2\pi a^2$, i.e. $\Gamma_i/2\pi b^2 \ll \Gamma_i/2\pi a^2$. This is equivalent to state that the vortices are well-separated: $a \ll b$. The second hypothesis is that the perturbations consist in bending deformations of the vortices with a small vertical wavenumber k_z such that $k_z a F_{hi} \ll 1$. These two assumptions are similar to those assumed in vortex stability analysis using vortex filaments in a homogeneous fluid (Crow 1970; Robinson & Saffman 1982). The only difference is the long-wavelength hypothesis in homogeneous fluid which does not involve the Froude number: $k_z a \ll 1$.

The position of each vortex core is assumed to be perturbed by an amount $(\tilde{\Delta x}_1, \tilde{\Delta y}_1)$ and $(\tilde{\Delta x}_2, \tilde{\Delta y}_2)$. Writing these perturbations in the form:

$$\begin{pmatrix} \widetilde{\Delta x}_i \\ \widetilde{\Delta y}_i \end{pmatrix} = \begin{pmatrix} \Delta x_i \\ \Delta y_i \end{pmatrix} \mathrm{e}^{\mathrm{i}k_z z} + \text{c.c.}, \tag{4.2}$$

where c.c. denotes the complex conjugate, and using the two hypothesis mentioned above, the following evolution equations for the perturbations of the

first vortex are obtained by means of an asymptotic analysis accurate at first order in $k_z^2 a^2 F_{hi}^2$ and $\Gamma_i/2\pi b^2$:

$$\begin{aligned}\frac{\mathrm{d}\Delta x_1}{\mathrm{d}t} &= -\frac{\Gamma_2}{2\pi b^2}\Delta y_1 + \frac{\Gamma_2}{2\pi b^2}\Psi(\beta)\Delta y_2 \qquad (4.3a)\\ &\quad + \left(f - \frac{\Gamma_1}{2\pi}\omega_{\mathrm{Re}}(k_z, F_{h1}, Ro_1)\right)\Delta y_1 + \frac{|\Gamma_1|}{2\pi}\omega_{\mathrm{Im}}(k_z, F_{h1}, Ro_1)\Delta x_1,\\ \frac{\mathrm{d}\Delta y_1}{\mathrm{d}t} &= -\frac{\Gamma_2}{2\pi b^2}\Delta x_1 + \frac{\Gamma_2}{2\pi b^2}\chi(\beta)\Delta x_2 \qquad (4.3b)\\ &\quad - \left(f - \frac{\Gamma_1}{2\pi}\omega_{\mathrm{Re}}(k_z, F_{h1}, Ro_1)\right)\Delta x_1 + \frac{|\Gamma_1|}{2\pi}\omega_{\mathrm{Im}}(k_z, F_{h1}, Ro_1)\Delta y_1.\end{aligned}$$

The complementary pair of equations for the second vortex are found by interchanging the subscripts 1 and 2. These equations are written in the frame of reference rotating at angular velocity $f + \Omega_b$, where $f = (\Gamma_1 + \Gamma_2)/2\pi b^2$ is the rate at which the unperturbed vortices rotate around each other. In this frame of reference, the base flow is steady. The functions ψ and χ are the mutual-induction functions and $\omega = \omega_{\mathrm{Re}} + \mathrm{i}\omega_{\mathrm{Im}}$ is the self-induction function which can be complex in a stratified and rotating fluid. They will be detailed below.

These equations have the same form as the ones derived by Crow (1970) or Jimenez (1975) for a pair of vortices in a homogeneous fluid using the Biot–Savart law to compute the induced motion of the vortices and the cut-off approximation to determine the self-induced velocity of the individual vortices. However, The vortex filament approach does not apply in a stratified and rotating fluid since the Kelvin theorem is not valid.

The physical meaning of the three terms in the righthand side of (4.3) is the following. The first term represents the strain effect of the basic flow field of one vortex on the perturbation sustained by the other vortex. The second term is the mutual-induction effect, i.e. the effect of the perturbation of one vortex on the basic flow of the other vortex. This effect depends on the mutual-induction functions:

$$\chi(\beta) = -\beta^2 K_1'(\beta), \qquad \psi(\beta) = \beta K_1(\beta), \qquad (4.4)$$

where $\beta = bk_zF_{h1}/|Ro_1| = bk_zF_{h2}/|Ro_2|$ and K_1 is the modified Bessel function of the second kind of first order. Although their explicit form are different, these functions are the equivalent, in a stratified and rotating fluid, of the Crow's first and second mutual-induction functions (Crow 1970). χ and ψ are equal to unity for $\beta = 0$ and then goes to zero exponentially for large β.

The last term represents the effect of the rotation of the vortex pair at angular velocity f and the self-induction effect, i.e. the effect of a vortex on itself. If alone, this self-induction corresponds to a rotation of the vortex at angular velocity $\Gamma_i/2\pi\omega_{Re}$ around its unperturbed location. When $\omega_{Im} < 0$,

this rotation is damped at rate $\sigma = |\Gamma|/2\pi\omega_{Im}$. In a stratified and rotating fluid, the self-induction function[1] is given by:

$$\omega(k_z, F_{hi}, Ro_i) = k_z^2 F_{hi}^2 \left[\frac{D(F_{hi})}{2} + \frac{E(F_{hi})}{Ro_i} - \frac{1}{2Ro_i^2} \left(\ln\left(\frac{ak_z F_h}{2|Ro_i|} \right) - F(F_{hi}) + \gamma_e \right) \right], \quad (4.5)$$

where $\gamma_e = 0.5772$ is the Euler constant and D, E and F are parameters depending on the Froude number F_{hi} (Billant *et al.* 2007) and the angular velocity Ω of the individual vortices. Their expression is given in appendix A. In this paper, we consider the Lamb–Oseen profile:

$$\Omega(r) = \frac{1}{r^2} \left(1 - \mathrm{e}^{-r^2} \right). \quad (4.6)$$

In this case, the self-induction is real and positive for $F_h \leq 1$ whatever Ro in contrast to homogeneous fluids for which it is negative. For $F_h \geq 1$, the self-induction becomes complex with a negative imaginary part ω_{Im} because the bending disturbance is damped by a viscous critical layer at the radius where the angular velocity of the vortex is equal to the Brunt–Väisälä frequency.

By using the equations (4.3) and their complementary equations for the other vortex, Billant *et al.* (2007) have recovered the zigzag instability of vortex pairs.

4.2.2 Generalization to vortex arrays in a stratified and rotating fluid

Robinson & Saffman (1982) have investigated the stability of vortex arrays in a homogeneous fluid in the limit of well-separated vortices and long-wavelength bending perturbations following Crow's stability analysis of a counter-rotating vortex pair. Their stability equations have the same form as those of Crow (1970) (or 4.3) except that they sum up all the strain and mutual-induction effects of each vortex of the array. In order to determine the three-dimensional stability of vortex arrays in a stratified and rotating fluid, we can thus follow the analysis of Robinson & Saffman (1982), except that the mutual-induction functions and self-induction functions have to be replaced by those valid in a stratified and rotating fluid.

Since the detailed derivation of the stability equations of vortex arrays can be found in Robinson & Saffman (1982), we recall here only briefly the main steps in the case of the Kármán vortex street. The generalization to the symmetric double row and the single row is straightforward.

[1] Note that the self-induction function is not exactly defined as in Crow (1970) or Robinson & Saffman (1982).

Kármán vortex street

The Kármán vortex street consists in a staggered double row of two-dimensional vertical vortices. The upper row lies in the plane $y = 0$, with each vortex having a positive circulation Γ and a radius a (figure 4.1). The lower row is in the plane $y = -h$, with each vortex having a negative circulation $-\Gamma$ and also a radius a. The vortices on each row are separated by a distance b and the two rows are staggered by a distance $b/2$. The whole unperturbed vortex array moves with a uniform velocity U in the frame of reference rotating at rate Ω_b about the vertical axis. Since all vortices have the same absolute circulation, they are characterized by a single Froude number $F_h = \Gamma/2\pi a^2 N$. In contrast, the Rossby number of the vortices of the upper row is $Ro = \Gamma/4\pi a^2 \Omega_b$ while the Rossby number of the vortices of the lower row is opposite: $-Ro$.

In the frame of reference rotating at rate Ω_b and translating at constant velocity U, the position of the perturbed vortices in the horizontal plane (x, y) is:

$$\begin{aligned} (x_{1,m}, y_{1,m}) &= (ml\,,\,0) &&+ (\Delta x_{1,m}\,,\,\Delta y_{1,m})\mathrm{e}^{\mathrm{i}k_z z} + \text{c.c.}, \\ (x_{2,n}, y_{2,n}) &= ((n+1/2)\,l\,,\,-h) &&+ (\Delta x_{2,n}\,,\,\Delta y_{2,n})\mathrm{e}^{\mathrm{i}k_z z} + \text{c.c.}, \end{aligned}$$

where the subscripts $(1, m)$ and $(2, n)$ denote a vortex respectively in the upper and lower row, m and n being integers. The amplitude of the three-dimensional bending perturbations of the vortices around their unperturbed position are $(\Delta x_{1,m}, \Delta y_{1,m})\mathrm{e}^{\mathrm{i}k_z z}$ and $(\Delta x_{2,n}, \Delta y_{2,n})\mathrm{e}^{\mathrm{i}k_z z}$, and k_z is their vertical wavenumber.

By summing up the straining and the mutual induction effects due to each vortex, the following evolution equations for the perturbations of a vortex m

in the upper row are found:

$$\begin{aligned}
\frac{\mathrm{d}\Delta x_{1,m}}{\mathrm{d}t} &= -\frac{\Gamma}{2\pi}\omega_{\mathrm{Re}}(k_z,F_h,Ro)\Delta y_{1,m}+\frac{|\Gamma|}{2\pi}\omega_{\mathrm{Im}}(k_z,F_h,Ro)\Delta x_{1,m} \qquad (4.7a)\\
&\quad -\frac{\Gamma}{2\pi}\sum_{p\neq m}\frac{\Delta y_{1,m}-\psi_{pm}\Delta y_{1,p}}{b_{pm}^2}\\
&\quad +\frac{\Gamma}{2\pi}\sum_{q}\frac{(\tilde{b}_{qm}^2-h^2)\Delta y_{1,m}-(\tilde{b}_{qm}^2\psi_{qm}-h^2\chi_{qm})\Delta y_{2,q}}{L_{qm}^4}\\
&\quad +\frac{\Gamma}{2\pi}\sum_{q}\frac{\tilde{b}_{qm}h\left[2\Delta x_{1,m}-(\chi_{qm}+\psi_{qm})\Delta x_{2,q}\right]}{L_{qm}^4}\\
\frac{\mathrm{d}\Delta y_{1,m}}{\mathrm{d}t} &= +\frac{\Gamma}{2\pi}\omega_{\mathrm{Re}}(k_z,F_h,Ro)\Delta x_{1,m}+\frac{|\Gamma|}{2\pi}\omega_{\mathrm{Im}}(k_z,F_h,Ro)\Delta y_{1,m} \qquad (4.7b)\\
&\quad -\frac{\Gamma}{2\pi}\sum_{p\neq m}\frac{\Delta x_{1,m}-\chi_{pm}\Delta x_{1,p}}{b_{pm}^2}\\
&\quad +\frac{\Gamma}{2\pi}\sum_{q}\frac{(\tilde{b}_{qm}^2-h^2)\Delta x_{1,m}-(\tilde{b}_{qm}^2\chi_{qm}-h^2\psi_{qm})\Delta x_{2,q}}{L_{qm}^4}\\
&\quad -\frac{\Gamma}{2\pi}\sum_{q}\frac{\tilde{b}_{qm}h\left[2\Delta y_{1,m}-(\chi_{qm}+\psi_{qm})\Delta y_{2,q}\right]}{L_{qm}^4},
\end{aligned}$$

where $b_{pm}=(p-m)b$, $\tilde{b}_{qm}=(q-m+1/2)b$ and $L_{qm}^2=h^2+\tilde{b}_{qm}^2$. The subscripts on ψ and χ indicate that the function arguments are $|b_{pm}|k_zF_h/Ro$ and $|L_{qm}|k_zF_h/Ro$ for subscripts pm and qm respectively. Similar equations are found for a vortex $(2,n)$ in the lower row. We now consider linear perturbations of the form:

$$\begin{aligned}
(\Delta x_{1,m},\Delta y_{1,m}) &= (\Delta x_1,\Delta y_1)\mathrm{e}^{\mathrm{i}m\phi+\sigma t} \qquad (4.8a)\\
(\Delta x_{2,n},\Delta y_{2,n}) &= (\Delta x_2,\Delta y_2)\mathrm{e}^{\mathrm{i}(n+\frac{1}{2}\phi+\sigma t)} \qquad (4.8b)
\end{aligned}$$

with σ the growth rate and $0\leq\phi\leq\pi$. As shown by Robinson & Saffman (1982), ϕ/b can be considered as a wavenumber of the disturbance in the row direction. However, it will be more convenient to introduce in §§ 4.3 and 4.4 the wavelength of the disturbance $\mu b=2\pi b/\phi$ in the row direction with $2\leq\mu\leq\infty$. A value $\mu=2$ implies a periodicity every two vortices, $\mu=4$ every four vortices and so on, while $\mu=\infty$ means that all the vortices on a single row are displaced in the same direction.

Following Robinson & Saffman (1982), it is also convenient to introduce symmetric and antisymmetric modes:

$$\begin{aligned}
(\Delta x_s,\Delta y_s) &= (\Delta x_1+\Delta x_2,\Delta y_1-\Delta y_2),\\
(\Delta x_a,\Delta y_a) &= (\Delta x_1-\Delta x_2,\Delta y_1+\Delta y_2).
\end{aligned}$$

The physical meaning of these modes can be easily understood in the case $\mu = \infty$, i.e. when all vortices of a given row are displaced in the same direction. The symmetric mode corresponds then to a displacement of each row in the same $x-$direction but in opposite $y-$direction, i.e. a modulation of the row spacing h along the vertical direction. Conversely, the antisymmetric mode corresponds to displacements of each row in opposite $x-$direction but in the same $y-$direction, i.e. a vertical modulation of the interval $b/2$ in the $x-$direction between the two rows.

Inserting (4.8) into (4.7) and the corresponding equations for the lower row, we obtain the following eigenvalue problem for the symmetric and antisymmetric modes:

$$\begin{pmatrix} \frac{2\pi b^2}{\Gamma}\sigma + B - b^2\overline{\omega}_{\mathrm{Im}} & A - C + b^2\overline{\omega}_{\mathrm{Re}} & -b^2\Delta\omega_{\mathrm{Im}} & b^2\Delta\omega_{\mathrm{Re}} \\ \tilde{A} + \tilde{C} - b^2\overline{\omega}_{\mathrm{Re}} & \frac{2\pi b^2}{\Gamma}\sigma + \tilde{B} - b^2\overline{\omega}_{\mathrm{Im}} & -b^2\Delta\omega_{\mathrm{Re}} & -b^2\Delta\omega_{\mathrm{Im}} \\ -b^2\Delta\omega_{\mathrm{Im}} & b^2\Delta\omega_{\mathrm{Re}} & \frac{2\pi b^2}{\Gamma}\sigma - B - b^2\overline{\omega}_{\mathrm{Im}} & A + C + b^2\overline{\omega}_{\mathrm{Re}} \\ -b^2\Delta\omega_{\mathrm{Re}} & -b^2\Delta\omega_{\mathrm{Im}} & \tilde{A} - \tilde{C} - b^2\overline{\omega}_{\mathrm{Re}} & \frac{2\pi b^2}{\Gamma}\sigma - \tilde{B} - b^2\overline{\omega}_{\mathrm{Im}} \end{pmatrix} \begin{pmatrix} \Delta x_s \\ \Delta y_s \\ \Delta x_a \\ \Delta y_a \end{pmatrix} = 0, \quad (4.9)$$

where

$$\overline{\omega} = \overline{\omega}_{\mathrm{Re}} + \mathrm{i}\overline{\omega}_{\mathrm{Im}} = \frac{1}{2}[\omega(k_z, F_h, Ro) + \omega(k_z, F_h, -Ro)], \quad (4.10a)$$

$$\Delta\omega = \Delta\omega_{\mathrm{Re}} + \mathrm{i}\Delta\omega_{\mathrm{Im}} = \frac{1}{2}[\omega(k_z, F_h, Ro) - \omega(k_z, F_h, -Ro)], \quad (4.10b)$$

and

$$A = \frac{\pi^2}{3} - \frac{\pi^2}{\cosh^2 \kappa\pi} - 2\sum_{p=1}^{\infty} \frac{\psi_p \cos p\phi}{p^2}, \quad (4.11a)$$

$$B = 2\mathrm{i}\sum_{q=0}^{\infty} \frac{(q+\frac{1}{2})\kappa}{\left[(q+\frac{1}{2})^2 + \kappa^2\right]^2} (\chi_q + \psi_q) \sin (q + \frac{1}{2})\phi, \quad (4.11b)$$

$$C = 2\sum_{q=0}^{\infty} \frac{(q+\frac{1}{2})^2\psi_q - \kappa^2\chi_q}{\left[(q+\frac{1}{2})^2 + \kappa^2\right]^2} \cos (q + \frac{1}{2})\phi, \quad (4.11c)$$

with the spacing ratio $\kappa = h/b$. The function arguments of ψ and χ are pbk_zF_h/Ro and $[(q+1/2)^2+\kappa^2]^{\frac{1}{2}}bk_zF_h/Ro$ for subscripts p and q respectively. $\tilde{A}$, $\tilde{B}$ and $\tilde{C}$ are found by interchanging the symbols χ and ψ in (4.11).

Contrary to homogeneous fluids studied by Robinson & Saffman (1982), the symmetric and antisymmetric modes do not always decouple in (4.9) because $\Delta\omega \neq 0$ when the self-induction for the vortices of the upper and lower rows are not equal: $\omega(k_z, F_h, Ro) \neq \omega(k_z, F_h, -Ro)$. A decoupling is recovered only in the limits $Ro \to \infty$ and $Ro \to 0$ for which $\omega(k_z, F_h, Ro) = \omega(k_z, F_h, -Ro)$ (see (4.5)).

Symmetric double row

The equations for the perturbations for the symmetric double row are the same as (4.7) except that $\tilde{b}_{qm} = (q-m)b$. Considering perturbations of the form:

$$\begin{aligned}(\Delta x_{1,m}, \Delta y_{1,m}) &= (\Delta x_1, \Delta y_1)\mathrm{e}^{\mathrm{i}m\phi+\sigma t},\\ (\Delta x_{2,n}, \Delta y_{2,n}) &= (\Delta x_2, \Delta y_2)\mathrm{e}^{\mathrm{i}n\phi+\sigma t},\end{aligned}$$

leads to exactly the same eigenvalue problem as (4.9) except that the coefficients A, B and C are slightly different:

$$A = \frac{\pi^2}{3} + \frac{\pi^2}{\sinh^2 \kappa\pi} - 2\sum_{p=1}^{\infty} \frac{\psi_p \cos p\phi}{p^2}, \tag{4.12a}$$

$$B = 2\mathrm{i}\sum_{q=1}^{\infty} \frac{q\kappa}{(q^2+\kappa^2)^2}(\chi_q + \psi_q)\sin q\phi, \tag{4.12b}$$

$$C = -\frac{\chi_\kappa}{\kappa^2} + 2\sum_{q=1}^{\infty} \frac{q^2\psi_q - \kappa^2\chi_q}{(q^2+\kappa^2)^2}\cos q\phi, \tag{4.12c}$$

where the function arguments of ψ and χ are pbk_zF_h/Ro, $(q^2+\kappa^2)^{\frac{1}{2}}bk_zF_h/Ro$ and $\kappa bk_zF_h/Ro$ for subscripts p, q and κ respectively. $\tilde{A}$, $\tilde{B}$ and $\tilde{C}$ are also found by interchanging the symbols χ and ψ in (4.12).

Single row

Finally, the case of the single row can be directly obtained by neglecting all terms related to the second row in (4.9) and by taking the limit $\kappa \to \infty$ for the coefficients in (4.11):

$$\begin{pmatrix} \frac{2\pi b^2}{\Gamma}\sigma - b^2\omega_{\mathrm{Im}} & A + b^2\omega_{\mathrm{Re}} \\ \tilde{A} - b^2\omega_{\mathrm{Re}} & \frac{2\pi b^2}{\Gamma}\sigma - b^2\omega_{\mathrm{Im}} \end{pmatrix} \begin{pmatrix} \Delta x_1 \\ \Delta y_1 \end{pmatrix} = 0, \tag{4.13}$$

with

$$A = \frac{\pi^2}{3} - 2\sum_{p=1}^{\infty} \frac{\psi_p \cos p\phi}{p^2},$$

where the function argument of ψ is pbk_zF_h/Ro for subscript p. $\tilde{A}$ has the same expression than A but with ψ replaced with χ. In this case, the growth rate can be obtained directly:

$$\frac{2\pi b^2}{\Gamma}\sigma = \pm\sqrt{[A + b^2\omega_{\mathrm{Re}}][\tilde{A} - b^2\omega_{\mathrm{Re}}]} + b^2\omega_{\mathrm{Im}}. \tag{4.14}$$

4.3 Stratified and non-rotating fluid

4.3.1 Kármán vortex street

In the case of a stratified and non-rotating fluid ($Ro = \infty$), additional simplifications can be made in (4.9–4.11). The arguments pbk_zF_h/Ro and $[(q+1/2)^2+\kappa^2]^{\frac{1}{2}}bk_zF_h/Ro$ of the mutual induction functions are equal to 0 implying that χ and ψ have always a value equal to unity. This also implies that $A = \tilde{A}$, $B = \tilde{B}$ and $C = \tilde{C}$. Moreover, we see from (4.5) that the self-induction functions $\omega(k_z, F_h, \pm Ro)$ converge to a single function $\omega_\infty(k_z, F_h)$ when $Ro \to \infty$:

$$\omega_\infty(k_z, F_h) = \lim_{Ro\to\infty} \omega(k_z, F_h, \pm Ro) = \frac{D(F_h)}{2} k_z^2 F_h^2. \tag{4.15}$$

The symmetric and antisymmetric modes then decouple since $\Delta\omega_{\mathrm{Re}} = \Delta\omega_{\mathrm{Im}} = 0$ in (4.9). Their growth rate is given by:

$$\frac{2\pi b^2}{\Gamma}\sigma_s = -B \pm \sqrt{A^2 - (C - b^2\omega_{\infty\,Re})^2} + b^2\omega_{\infty\,Im}, \tag{4.16a}$$

$$\frac{2\pi b^2}{\Gamma}\sigma_a = +B \pm \sqrt{A^2 - (C + b^2\omega_{\infty\,Re})^2} + b^2\omega_{\infty\,Im}, \tag{4.16b}$$

where A, B and C are still given by (4.11) when taking χ and ψ equal to 1. One may note that because B is purely imaginary and $\omega_{\infty\,Im} < 0$, the vortex array can be unstable only if the term inside the square-root is positive: $A^2 > (C \pm b^2\omega_{\infty\,Re})^2$. Note that in the two-dimensional limit $k_z = 0$, we have $\omega_\infty = 0$ so that symmetric and antisymmetric modes have the same growth rate. Similarly, symmetric and antisymmetric modes have the same growth rate whatever k_z when $\mu = 2$ because $C = 0$.

Strongly stratified and non-rotating fluid

For clarity we first present the case of a strongly stratified and non-rotating fluid ($F_h \to 0$, $Ro \to \infty$). To contrast our results, it is first interesting to recall briefly the results of Robinson & Saffman (1982) in homogeneous fluids. For the Kármán vortex street, Robinson & Saffman (1982) found that for κ less than about 0.3 (the precise value depends on the vortex radius a compared to b), the dominant instability is three-dimensional with $\mu = \infty$ and an antisymmetric configuration (we exclude the short-wavelength instabilities also found by Robinson & Saffman (1982) but for which their approach is not valid.). When κ is greater than about 0.3, the most unstable mode is two-dimensional with $\mu = 2$ and with either the symmetric and antisymmetric configurations since they have the same growth rate in this case (see (4.16)). This two-dimensional instability is a pairing instability where adjacent vortices of the same row tend to merge.

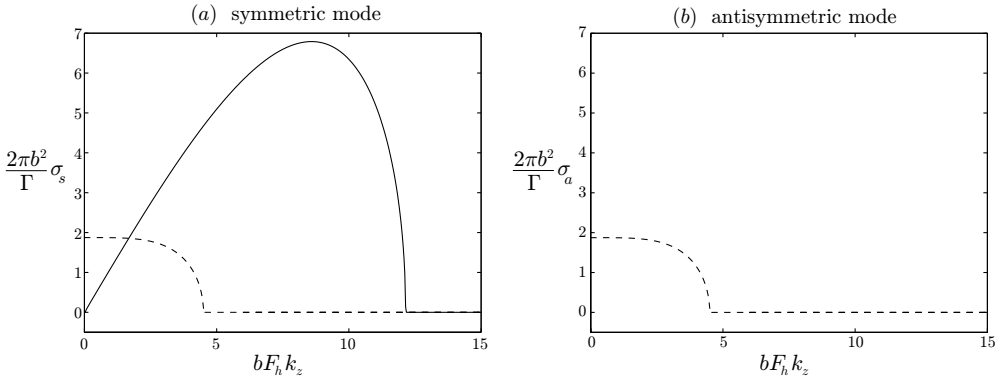

Figure 4.2: Nondimensional growth rate $2\pi b^2\sigma/\Gamma$ as a function of the rescaled vertical wavenumber $bF_h k_z$ for the Kármán vortex street with close rows $\kappa = 0.2$ in a strongly stratified and non-rotating fluid: (a) symmetric mode, (b) antisymmetric mode. The case $\mu = \infty$ is plotted in solid line and the case $\mu = 2$ is plotted in dashed line.

Now looking to the case of a strongly stratified fluid, figure 4.2 shows the nondimensional growth rate $2\pi b^2\sigma/\Gamma$ of the symmetric and antisymmetric modes as a function of the rescaled vertical wavenumber $bF_h k_z$ in the case of a strongly stratified fluid for the street spacing ratio $\kappa = 0.2$. For each mode, two row wise periodicities are shown $\mu = \infty$ (solid line) and $\mu = 2$ (dashed line). For $\mu = \infty$, we see that the symmetric mode is the most unstable for a finite value of k_z while the antisymmetric mode is stable for any vertical wavenumber. Strikingly, this is the opposite to the case of a homogeneous fluid where the symmetric mode is stable while the antisymmetric mode is three-dimensionally unstable. A sketch of the displacements induced by these three-dimensional instabilities in stratified and homogeneous fluids is shown in figure 4.3 (a, b) in a horizontal cross-section. In stratified fluids (figure 4.3 a), the interval in the $y-$direction between the two rows is modulated along the vertical by the instability. In homogeneous fluids (figure 4.3 b), it is the interval in the $x-$direction between the two rows which is vertically modulated. Since such three-dimensional bending instability in strongly stratified fluids has been called zigzag instability for vortex pairs in stratified fluids (Billant & Chomaz 2000a; Otheguy *et al.* 2006), we use also this name for the present three-dimensional symmetric instability of the Kármán vortex street in stratified fluids. For a counter-rotating vortex pair, a similar inversion of the symmetry is observed: the unstable mode is symmetric in homogeneous fluids (Crow instability), while in stratified fluids, it is the antisymmetric mode which is unstable (zigzag instability). This inversion is due to the fact that the self-induction is positive in stratified and rotating fluids while it is negative in homogeneous fluids (Billant *et al.* 2007).

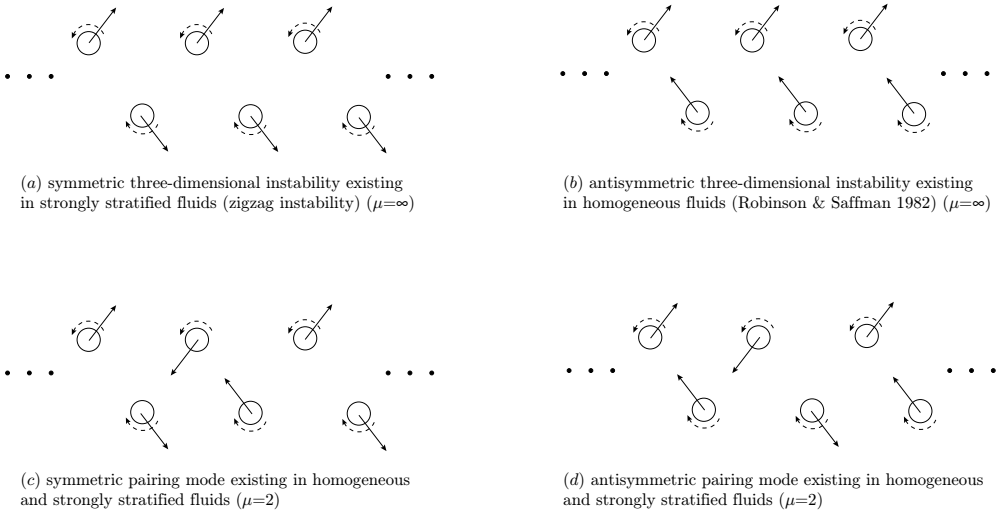

(a) symmetric three-dimensional instability existing in strongly stratified fluids (zigzag instability) (μ=∞)

(b) antisymmetric three-dimensional instability existing in homogeneous fluids (Robinson & Saffman 1982) (μ=∞)

(c) symmetric pairing mode existing in homogeneous and strongly stratified fluids (μ=2)

(d) antisymmetric pairing mode existing in homogeneous and strongly stratified fluids (μ=2)

Figure 4.3: Sketch of the displacements in horizontal cross sections induced by the variant dominant modes for the Kármán vortex street. In the case of three-dimensional instabilities, the displacements shown alternate along the vertical $z-$direction.

As seen on figure 4.2, the case $\mu = 2$ (dashed line) is also unstable but the maximum growth rate is obtained for two-dimensional perturbations ($k_z = 0$) and the symmetric and antisymmetric modes have the same growth rate. As sketched on figure 4.3 (c, d), this instability is a pairing instability which tends to move closer or away adjacent vortices of a given row (von Kármán 1912; Robinson & Saffman 1982). Because this instability is two-dimensional the stratification has no effect on the dominant mode. However, it should be remarked that the growth rate of three-dimensional perturbations decreases with bF_hk_z in strongly stratified fluids instead of bk_z in homogeneous fluids. As $F_h \to 0$, the band of unstable vertical wavenumbers k_z thus widens like for the instability of a horizontal shear layer in stratified fluids (Deloncle *et al.* 2007*b*).

For the value $\kappa = 0.2$ shown in figure 4.2, the overall dominant instability is the symmetric three-dimensional instability for $\mu = \infty$ (zigzag instability). Intermediate values of the parameter μ between 2 and ∞ give always lower maximum growth rate than the one for $\mu = \infty$. By varying κ and μ, we have found that the symmetric zigzag instability with $\mu = \infty$ remains dominant for $\kappa \leq 0.41$ (note that this value does not depend on the vortex radius a compared to b in a stratified and non-rotating fluid). When the two vortex rows are more distant $\kappa > 0.41$, the dominant overall instability becomes the $\mu = 2$ two-dimensional instability (pairing instability) with both symmetric and antisymmetric configurations. These results are summarized in figure 4.4 where

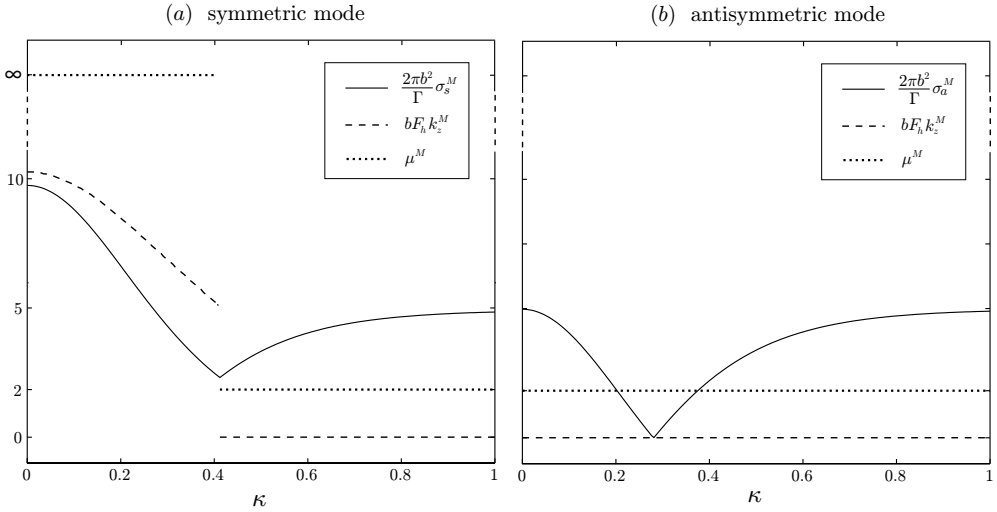

Figure 4.4: Plots of the maximum growth rate $2\pi b^2\sigma^M/\Gamma$, the corresponding wavenumbers $bF_h k_z^M$ and row wise periodicity μ^M versus the street spacing ratio κ for the Kármán vortex street in a strongly stratified and non-rotating fluid: (a) symmetric mode, (b) antisymmetric mode.

the maximum growth rates of the symmetric $2\pi b^2\sigma_s^M/\Gamma$ and antisymmetric $2\pi b^2\sigma_a^M/\Gamma$ modes versus the street spacing ratio κ are plotted. The corresponding wavenumbers $bF_h k_z^M$ and row wise periodicity μ^M are also indicated.

Stratified and non-rotating fluid: effect of the Froude number

We now investigate the effect of the Froude number in a non-rotating fluid. Figure 4.5 shows the growth rate of the symmetric and antisymmetric modes for various Froude numbers from strong stratification ($F_h = 0$) to moderate stratification ($F_h = 1.2$). We see that the growth rate curves (solid lines) of the three-dimensional zigzag instability for $F_h = 0$ and $F_h = 1$ are almost similar except a small decrease in the most amplified wavenumber. The maximum growth rate has exactly the same value and is independent of F_h if $F_h < 1$. For this reason, the threshold $\kappa = 0.41$ below which the dominant instability is the three-dimensional for $F_h = 0$ remains the same for all $F_h \leq 1$. The stratification has thus little effect on the zigzag instability as long as $F_h < 1$. However, when the Froude number is further increased to $F_h = 1.2$, an abrupt drop of 60% of the maximum growth rate is observed. This damping is due to the fact that ω_{Im} is no longer zero but negative when $F_h > 1$ because the bending disturbances have a viscous critical layer (Billant *et al.* 2007).In contrast, the maximum growth rate of the two-dimensional pairing instabilities

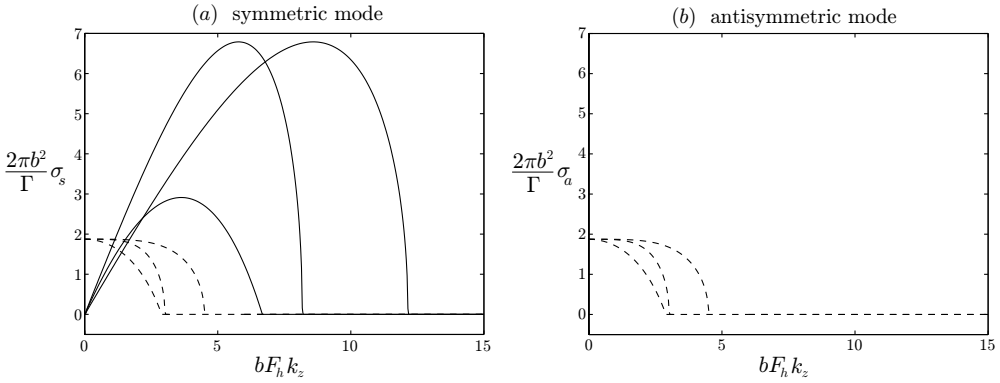

Figure 4.5: Similar to figure 4.2 but for various Froude numbers. We recall that we present two periodicities: $\mu = \infty$ (solid lines) and $\mu = 2$ (dashed lines). For each μ, the curves from right to left correspond to the Froude numbers: $F_h \to 0$, $F_h = 1.$ and $F_h = 1.2$.

is not affected by the stratification. If we would further increase the Froude number to $F_h \approx 1.3$, pairing modes would become dominant.

4.3.2 Symmetric double row

For a stratified and non-rotating fluid, simplifications similar to the Kármán vortex street case are made for the symmetric double row. Symmetric and antisymmetric modes decouple leading to the same dispersion relations (4.16) with A, B and C given by (4.12) by taking again ψ and χ equal to 1.

Strongly stratified and non-rotating fluid

In homogeneous fluid, Robinson & Saffman (1982) have found that the most unstable instability for this vortex array is always the symmetric mode for $\mu = 2$ and a finite value of k_z regardless of the value of the street spacing ratio κ.

As shown in figure 4.6, we see that the most unstable mode of the symmetric double row for $\kappa = 0.5$ in a strongly stratified and non-rotating fluid is also a three-dimensional mode with $\mu = 2$ (dashed line in figure 4.6 *b*) like in homogeneous fluid but with the opposite symmetry, i.e. antisymmetric. The $\mu = \infty$ antisymmetric mode (solid line in figure 4.6 *b*) is also three-dimensionally unstable but its maximum growth rate is less than the $\mu = 2$ antisymmetric mode. The symmetric mode is unstable for $\mu = 2$ but not for $\mu = \infty$ (figure 4.6 *a*).

The displacements induced by the $\mu = 2$ three-dimensional antisymmetric instability is displayed in figure 4.7 (*d*) along with the other eigenmodes with $\mu = \infty$ or opposite symmetry (figure 4.7 *a*,*b*,*c*). We see on figure 4.7 (*d*), that

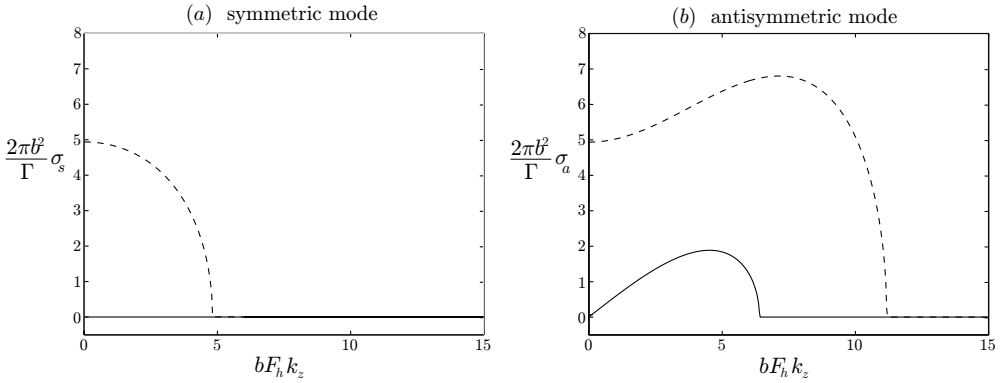

Figure 4.6: Similar to figure 4.2 but for the double symmetric row with $\kappa = 0.5$. We recall that we present two periodicities: $\mu = \infty$ (solid lines) and $\mu = 2$ (dashed lines).

two adjacent vortices of a given row tend to move closer or away from each other like in the zigzag instability of a single co-rotating vortex pair (Otheguy *et al.* 2006). Similarly, two facing vortices of the two rows tend to be rotated like in the zigzag instability of a single counter-rotating vortex pair (Billant & Chomaz 2000*a*). Therefore, the $\mu = 2$ antisymmetric instability can be interpreted as a cooperation between a separate zigzag instability of adjacent pairs of co-rotating vortices of a given row and a separate zigzag instability of pairs of facing counter-rotating vortices. This results in a three-dimensional instability more unstable than any of the two instabilities considered separately.

Figure 4.8 shows the maximum growth rate of the dominant instability over all possible values of μ and as a function of κ for the symmetric and antisymmetric configurations. The $\mu = 2$ zigzag instability with the antisymmetric configuration is the most unstable for all value of κ. In the limit where the rows are very close: $\kappa \to 0$, the growth rate scaled by $\Gamma/2\pi b^2$ diverges since it is proportional to the maximum strain: $\sigma_a^M \sim \Gamma/2\pi h^2$ so that $\sigma_a^M 2\pi b^2/\Gamma \sim 1/\kappa^2$. When κ increases, i.e. when the distance between the two rows increases, the most amplified vertical wavenumber k_z^M tends to 0. This is because the unstable interaction between the facing rows of vortices decreases so that the $\mu = 2$ three-dimensional zigzag instability tends toward a two-dimensional pairing instability of adjacent vortices of a given row.

Stratified and non-rotating fluid: effect of the Froude number

Like for the Kármán vortex street, we have investigated the effect of the Froude number in a non-rotating fluid. As seen in figure 4.9, the Froude number has a weak effect of the zigzag instability when it is increased from $F_h = 0$ to $F_h = 1$.

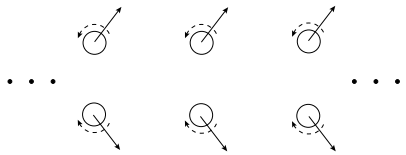

(a) symmetric three-dimensional instability existing in homogeneous fluids (Robinson & Saffman 1982) (μ=∞)

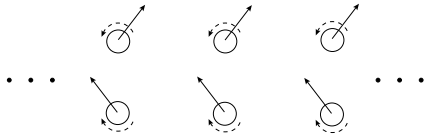

(b) antisymmetric three-dimensional instability existing in strongy stratified fluids (zigzag instability) (μ=∞)

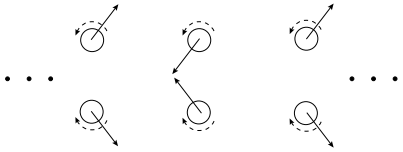

(c) symmetric three-dimensional instability existing in homogeneous and strongly stratified fluids.
This is the dominant instability in homogeneous fluids (Robinson & Saffman 1982) (μ=2)

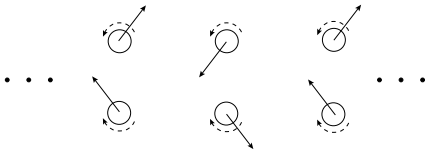

(d) antisymmetric three-dimensional instability existing in homogeneous and strongly stratified fluids.
This is the dominant instability in strongly stratified fluids (zigzag instability) (μ=2)

Figure 4.7: Similar to figure 4.3 but for the double symmetric row.

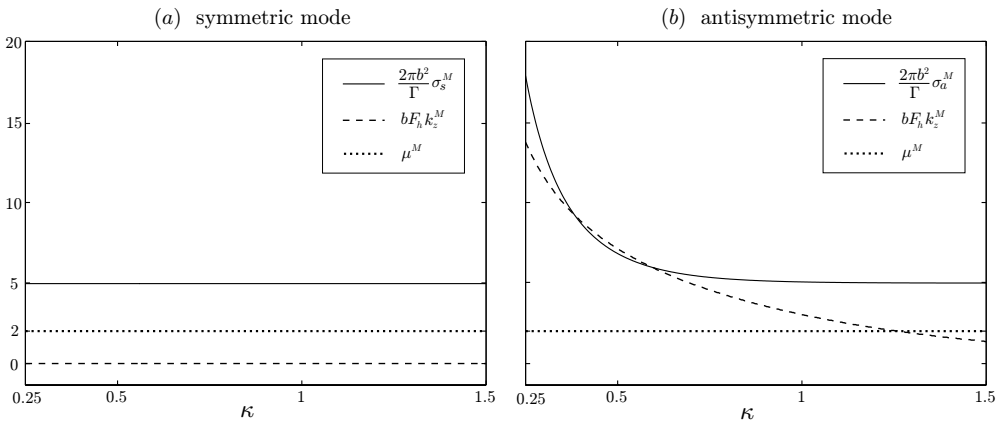

Figure 4.8: Similar to figure 4.4 but for the double symmetric row.

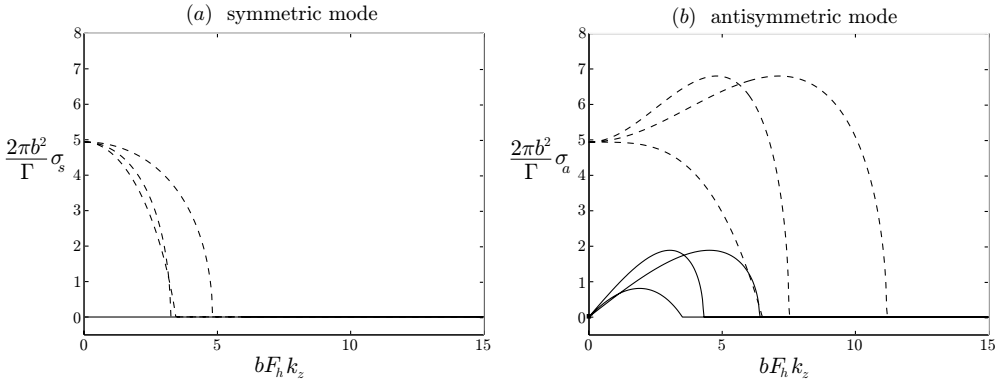

Figure 4.9: Similar to figure 4.2 but for the double symmetric row with $\kappa = 0.5$ and for various Froude numbers. We recall that we present two periodicities: $\mu = \infty$ (solid lines) and $\mu = 2$ (dashed lines). For each μ, the curves from right to left correspond to the Froude numbers: $F_h \to 0$, $F_h = 1.$ and $F_h = 1.2$.

However, when the Froude number is further increased to $F_h = 1.2$, the three-dimensional zigzag instability is strongly damped. The dominant instability is then the two-dimensional pairing mode.

4.3.3 Single row

The limit $\kappa \to \infty$ considered above for the Kármán vortex street or symmetric double row is in fact identical to the case of a single row since the two rows are infinitely far away from each other and do not feel themselves. As explained above, the dominant instability is then a two-dimensional instability with $\mu = 2$, i.e. a pairing instability of adjacent vortices of the row. The stratification has thus no effect except that the width of the band of unstable vertical wavenumbers scales like $1/F_h$ for $F_h \to 0$ and narrows slightly when F_h is increased.

4.4 Strongly stratified and rotating fluid: effect of the Rossby number

For a strongly stratified and rotating fluid ($F_h \to 0$, $Ro \neq \infty$), symmetric and antisymmetric modes do not decouple and the complete eigenvalue problem (4.9) or (4.13) is solved numerically using the eigensolver *eig* of Matlab.

4.4.1 Kármán vortex street

We have determined the dominant mode for $F_h \to 0$ four Rossby numbers from non-rotating fluid ($Ro = \infty$) to strong rotation ($Ro = 0.75$) and for various

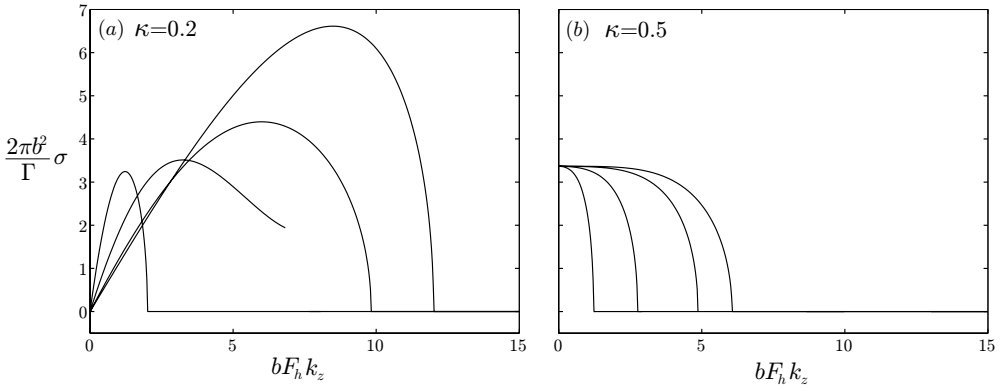

Figure 4.10: Nondimensional growth rate $2\pi b^2\sigma/\Gamma$ of the dominant mode as a function of the rescaled vertical wavenumber $bF_h k_z$ for the Kármán vortex street in a strongly stratified and rotating fluid: (a) close rows $\kappa = 0.2$, (b) distant rows $\kappa = 0.5$. In each plot, four increasing rotation rates are presented (from right curve to left curve): $Ro = \infty$, $Ro = 6$, $Ro = 2$, $Ro = 0.75$ for $a/b = 0.067$.

spacing ratios. Only positive Rossby numbers need to be considered since the problem is independent of the sign of Ro because the vortices of the two rows are counter-rotating. In this case, the problem depends on the core radius to separation distance a/b because of the logarithm term in (4.5). Here we have taken $a/b = 0.067$.

Figure 4.10 shows the growth rate of the dominant mode for the two typical configurations found in the previous section: close rows ($\kappa = 0.2$) and distant rows ($\kappa = 0.5$). In both cases, we have found that the most unstable mode remains qualitatively the same as in the non-rotating case: it is a $\mu = \infty$ three-dimensional bending instability for close rows and a two-dimensional pairing instability for distant rows. For close rows, we see that the maximum growth rate of the three-dimensional mode decreases significantly ($\sim 40\%$) for $Ro = 6$ compared to $Ro = \infty$ and then remains approximately constant when Ro is further decreased. The corresponding most unstable vertical wavenumber decreases monotically with Ro. Figure 4.11 further shows the maximum growth rate and most amplified wavenumber as a function of Ro. We notice that the most unstable vertical wavenumber decreases linearly to zero when Ro goes to zero. For distant rows, we directly see in figure 4.10 (b) that even if the maximum growth rate of the two-dimensional growth rate is not affected by rotation, the band of unstable vertical wavenumbers also narrows dramatically when the rotation increases.

In the limit of strong rotation ($Ro \to 0$), it can be proved that the unstable vertical wavenumbers follow the quasi-geostrophic scaling law. Indeed, we see from (4.11) that the coefficients A, B and C are only functions of bk_zF_h/Ro

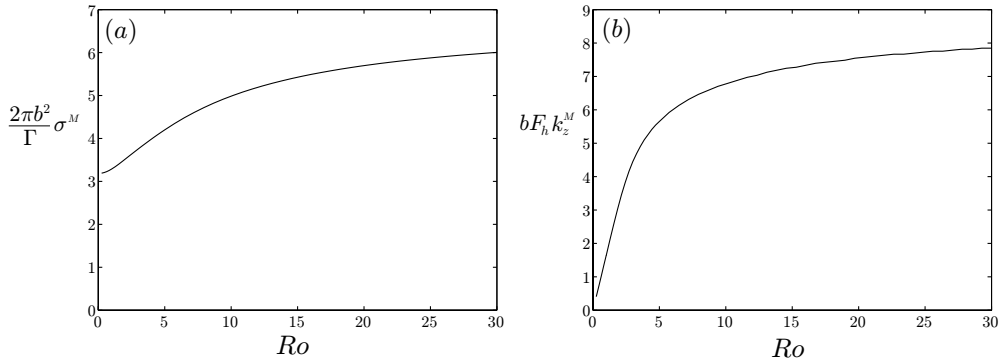

Figure 4.11: (a) Nondimensional growth rate $2\pi b^2\sigma^M/\Gamma$ of the most unstable mode and (b) the corresponding unstable wavenumber $bF_h k_z^M$ as a function of the Rossby number Ro for the Kármán vortex street with close rows ($\kappa = 0.2$) in a strongly stratified and rotating fluid.

through the arguments of the mutual-induction functions ψ and χ. In addition, the self-induction terms $b^2\omega(k_z, F_h, \pm Ro)$ that appear in the eigenvalue problem (4.9–4.11) converge to a single function $b^2\omega_0$ when $Ro \to 0$:

$$b^2\omega_0 = \lim_{Ro\to 0} b^2\omega(k_z, F_h, \pm Ro) = -\frac{b^2k_z^2F_h^2}{2Ro^2}\left(\ln\left(\frac{bk_zF_h}{2Ro}\right) + \ln\left(\frac{a}{b}\right) - F(F_h) + \gamma_e\right), \quad (4.17)$$

which is also a function of bk_zF_h/Ro. Consequently, k_z, F_h and Ro never appear separately but always as the group bk_zF_h/Ro in the eigenvalue problem (4.9). Thus, the growth rate is also only a function of bk_zF_h/Ro, i.e. $\sigma(k_z, F_h, Ro) = \tilde{\sigma}(bk_zF_h/Ro)$. It implies that the maximum vertical wavenumber of a three-dimensional instability scales like $Ro/bF_h = N/2b\Omega_b$ for small Ro and, similarly, that the size of the unstable band of vertical wavenumbers of a two-dimensional instability scales as Ro/bF_h for small Ro in agreement with quasi-geostrophic theory and figures 4.10 and 4.11.

4.4.2 Symmetric double row

Like for the Kármán vortex street, we have determined the dominant mode of the double symmetric row for $\kappa = 0.5$ for various Ro. Again, only positive Rossby number needs to be considered because of the symmetry of the base flow. As seen in figure 4.12 the growth rate curves keep the same shape when Ro is decreased from $Ro = \infty$ to $Ro = 0.75$ but the most amplified wavenumber decreases. We have found that the most unstable mode remains qualitatively the same as in the non-rotating case: it is a $\mu = 2$ three-dimensional bending

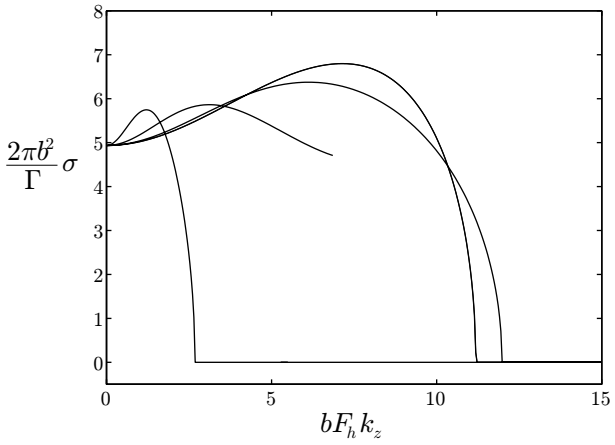

Figure 4.12: Similar to figure 4.10 but for the symmetric double row ($\kappa = 0.5$). Four rotation rates are presented (from right curve to left curve): $Ro = \infty$, $Ro = 6$, $Ro = 2$, $Ro = 0.75$ for $a/b = 0.067$.

instability. Figure 4.13 further shows the maximum growth rate and the most unstable vertical wavenumber of the dominant mode as a function of the Rossby number Ro. Contrary to the Kármán vortex street, the maximum growth rate is only slightly affected by the rotation: it is about 10% smaller with rotation compared to no-rotation. The most unstable vertical wavenumber is proportional to Ro for small Ro like for the Kármán vortex street (§ 4.4.1) and in agreement with the quasi-geostrophic theory.

4.4.3 Single row

The effect of rotation on the single row in a strongly stratified fluid is presented in figure 4.14. For this vortex array, the base flow is not symmetric so that positive as well as negative Rossby numbers need to be considered. For the positive Rossby numbers, the unstable band decreases monotically when Ro decreases as observed before. For negative Rossby numbers, the unstable wavenumber band first widens for intermediate values but then also shrinks for small negative values.

4.5 Conclusion

We have investigated by an asymptotic approach the three-dimensional stability in a stratified and rotating fluid of three steady vertical vortex arrays: the Kármán vortex street, the symmetric double row and the single row of corotating vortices. The approach assumes long-wavelength bending perturba-

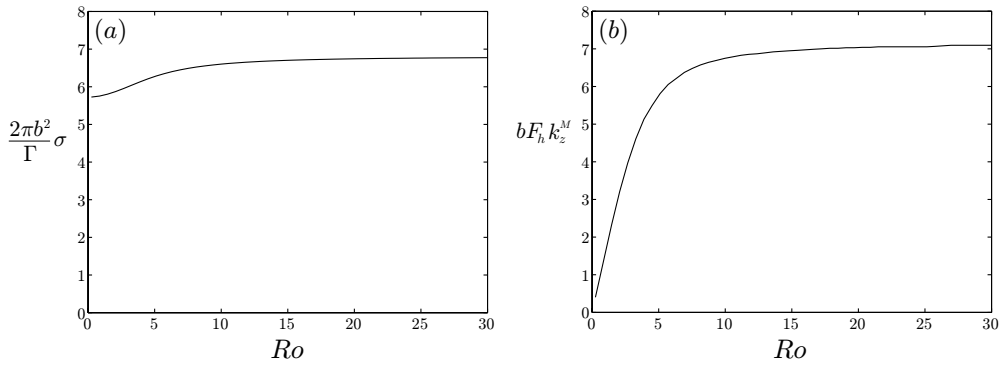

Figure 4.13: Similar to figure 4.11 but for the symmetric double row ($\kappa = 0.5$).

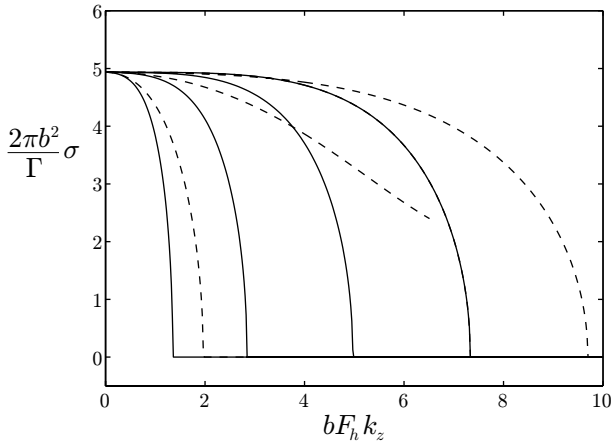

Figure 4.14: Similar to figure 4.11 but for the single row. Four positive rotation rates are presented in solid lines (from right curve to left curve): $Ro = \infty$, $Ro = 6$, $Ro = 2$, $Ro = 0.75$ and three negative rotation rates are presented in dashed lines (from right curve to left curve): $Ro = -6$, $Ro = -2$, $Ro = -0.75$. All curves were determined for $a/b = 0.067$.

tions and well-separated vortices. It is accurate to first order in rescaled vertical wavenumber $k_z^2 a^2 F_h^2$ and in strain $\Gamma/2\pi b^2$. The stability equations have the same form as those derived by Robinson & Saffman (1982) in a homogeneous fluid although their approach can not be directly applied in a stratified and rotating fluid since the circulation is not conserved. The differences between homogeneous and stratified and rotating fluids lies only in explicit expression of the mutual induction functions and the self-induction function (Billant *et al.* 2007).

Using this approach in a strongly stratified fluid and assuming a Lamb–Oseen vortex profile for each individual vortex, we have found that the Kármán vortex street for a spacing ratio $\kappa \leq 0.41$ and the symmetric double row for any spacing ratio are most unstable to a three-dimensionally instability which bends the vortices. This three-dimensional bending instability is similar to the zigzag instability on vortex pairs in a strongly stratified fluid (Billant & Chomaz 2000*a*; Otheguy *et al.* 2006).

Similar three-dimensional bending instabilities also exist in a homogeneous fluid (Robinson & Saffman 1982) but a striking difference is the opposite symmetry of the unstable mode in a stratified. For the Kármán vortex street, we have found that the most unstable mode for $\kappa \leq 0.41$ is three-dimensional symmetric while it is three-dimensional antisymmetric in homogeneous fluid (Robinson & Saffman 1982). Similarly, the double symmetric row is most unstable to a three-dimensional antisymmetric mode while it is a three-dimensional symmetric mode in a homogeneous fluid (Robinson & Saffman 1982). Like for vortex pairs (Billant *et al.* 2007), this inversion of the symmetry of the unstable mode is rooted in the different sign of the self-induction in a stratified fluid compared to a homogeneous fluid.

Another important difference is the most amplified vertical wavenumber, it scales like $1/bF_h$ (or $1/hF_h$ if $\kappa \ll 1$ for the double symmetric row) in a stratified fluid instead of $1/b$ in a homogeneous fluid. The instabilities predicted in the present study will therefore produce layers of typical thickness bF_h. In contrast, in both cases, homogeneous or stratified fluid, the growth rate of these three-dimensional instabilities scales like the strain $\Gamma/2\pi b^2$. The present instability of the Kármán vortex street in a stratified fluid might explain the experimental observations of Praud *et al.* (2005) and Holford & Linden (1999). They have observed that the columnar vortices created by towing a rake of vertical bars in a stratified fluid become vertically bent and evolve into pancake vortices.

For the Kármán vortex street with a large spacing ratio $\kappa > 0.41$, or the single row, the dominant instability remains a two-dimensional pairing instability in a stratified fluid like in a homogeneous fluid. In their study of the nonlinear evolution of an horizontal shear layer in a stratified fluid, Basak & Sarkar (2006) have observed the formation of a row of three-dimensional pan-

cake vortices. This result is not in contradiction with our finding that the single row is most unstable to two-dimensional disturbances because Basak & Sarkar (2006) have perturbed the initial two-dimensional shear layer with relatively strong three-dimensional fluctuations.

We have investigated the effect of the Froude number and shown that it has almost non effect as long as $F_h < 1$. However, when F_h is increased above unity, three-dimensional instabilities become strongly damped because long-wavelength bending perturbations have a viscous critical layer.

The effect of background rotation has been also investigated for a strongly stratified fluid. In this case, symmetric and antisymmetric modes do not decouple but we have always found that the dominant instability remains qualitatively similar to the non-rotating case: it is a three-dimensional zigzag instability for the Kármán vortex street with a small spacing ratio and for the double symmetric row with any spacing ratio; it is a two-dimensional pairing instability for the Kármán vortex with a large spacing ratio and for the single row. However, the most unstable wavenumber of three-dimensional instabilities decreases with rotation and has been shown to scale like $Ro/bF_h = N/2b\Omega_b$ for small Ro in agreement with quasi-geostrophic scaling laws. In this quasi-geostrophic limit, the decoupling between symmetric and antisymmetric modes is also recovered and the dominant three-dimensional instabilities have the same symmetry as for a stratified and non-rotating fluid.

All the asymptotic results will be compared to the results of numerical stability analysis in a companion paper (Deloncle *et al.* 2007*c*).

Appendix A. Expression of the parameters D, E and F

The parameters D, E and F used in the expression of the self-induction function ω valid in stratified and rotating fluids (see 4.2.1) depend on the Froude number and the nondimensional angular velocity Ω of the individual vortices. Their expression is (Billant *et al.* 2007):

$$D(F_h) = \lim_{\eta_0\to\infty}\int_0^{\eta_0}\frac{r^3\Omega(r)^4}{1-F_h^2\Omega(r)^2}\mathrm{d}r - \frac{1}{4F_h^2}\ln\left(1-\frac{F_h^2}{\eta_0^4}\right) \tag{4.18}$$

$$E(F_h) = \lim_{\eta_0\to\infty}\int_0^{\eta_0}\frac{r^3\Omega(r)^3}{1-F_h^2\Omega(r)^2}\mathrm{d}r - \frac{1}{4F_h}\ln\left(\frac{\eta_0^2-F_h}{\eta_0^2+F_h}\right) \tag{4.19}$$

$$F(F_h) = \lim_{\eta_0\to\infty}\int_0^{\eta_0}\frac{r^3\Omega(r)^2}{1-F_h^2\Omega(r)^2}\mathrm{d}r - \frac{1}{4}\ln\left(\eta_0^4-F_h^2\right). \tag{4.20}$$

These parameters are plotted in figure 4.15 for the Lamb–Oseen vortex profile. Note that in a strongly stratified fluid ($F_h \to 0$), $D = 9\ln 3 - 14\ln 2$, $E = 3/2\,(2\ln 2 - \ln 3)$ and $F = (\gamma_e - \ln 2)/2$.

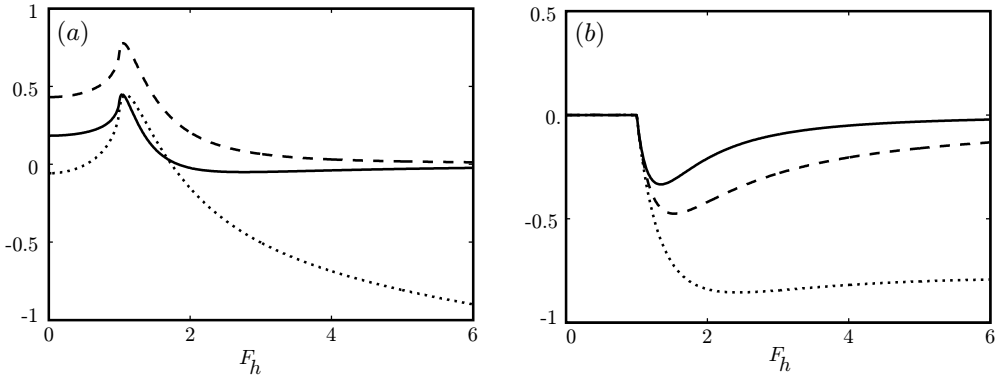

Figure 4.15: Real part (a) and imaginary part (b) of the parameters D (solid line), E (dashed-line) and F (dotted line) as a function of the Froude number F_h for the Lamb–Oseen vortex.

Chapter 5

Stability of vortex arrays in a stratified and rotating fluid: numerical analysis

Article in preparation for the *Journal of Fluid Mechanics*.

Three-dimensional stability of vortex arrays in a stratified and rotating fluid: numerical analysis

By AXEL DELONCLE, PAUL BILLANT AND JEAN-MARC CHOMAZ

Hydrodynamics Laboratory (LadHyX), Ecole Polytechnique,
91128 Palaiseau Cedex, France
axel.deloncle@ladhyx.polytechnique.fr

(In preparation for the *Journal of Fluid Mechanics*)

We determine numerically the dominant instabilities of steady vertical vortex arrays in a stratified and rotating fluid for high Reynolds numbers. Three classical configurations are studied: the Kármán vortex street, the symmetric double row and the single row of co-rotating vortices. The numerical results fully agree with the asymptotic analysis of Deloncle *et al.* (2007*d*) which assumes well-separated vortices and long-wavelength bending perturbations in a stratified and rotating inviscid fluid. The computed growth rates and eigenmodes are in excellent agreement with the theoretical results even for finite wavelength and close vortices. The Kármán vortex street with close rows and the double symmetric row in a stratified and rotating fluid are most unstable to a three-dimensional bending instability: the zigzag instability. The Kármán vortex street with distant rows and the single row are most unstable to a two-dimensional instability that tends to merge adjacent vortices of the same row, i.e. the pairing instability.

5.1 Introduction

By means of an asymptotic analysis, Deloncle *et al.* (2007*d*) (hereinafter referred as part I) have studied the three-dimensional stability of steady vertical vortex arrays in a stratified and rotating inviscid fluid. Three classical configurations have been considered: the Kármán vortex street, the symmetric double row and the single row of co-rotating vortices. The latter analysis assumes well-separated vortices and long-wavelength bending perturbations like in the stability analysis of Robinson & Saffman (1982) of arrays of vortex filaments in homogeneous fluid. However, the approach of part I is valid in a stratified and rotating fluid since it does not rely on the conservation of circulation like vortex filaments methods. The stability equations in stratified and rotating fluids turn out to be formally identical to those derived in homogeneous fluids by means of vortex filaments (Robinson & Saffman 1982), except that the self-induction and mutual-induction functions are different.

In a stratified and non-rotating fluid (for $F_h < 1$, where F_h is the horizontal Froude number), this analysis has revealed that the Kármán vortex street for a street spacing ratio $\kappa = h/b \leq 0.41$, where h is the distance between the rows and b the distance between vortices in the same row, and the symmetric double row for any spacing ratio are most unstable to a three-dimensional bending instability called zigzag instability. Its growth rate scales like the strain $\Gamma/2\pi b^2$, where Γ is the vortex circulation and the most unstable vertical wavenumber scales like $1/bF_h$. For the Kármán vortex street, the zigzag instability is symmetric with respect to the middle plane between the two rows while it is antisymmetric for the symmetric double row. In the cases of Kármán vortex street with well-separated vortex rows $\kappa > 0.41$ and the single row, the dominant instability is two-dimensional and corresponds to a pairing of adjacent vortices of the same row. In the presence of background rotation, symmetric and antisymmetric modes do not decouple anymore but the dominant instability remains qualitatively the same i.e. quasi-symmetric or quasi-antisymmetric and three-dimensional or two-dimensional. However, the most unstable wavenumber of three-dimensional instabilities decreases with the Rossby number Ro and scales like Ro/bF_h for small Ro in agreement with quasi-geostrophic scaling laws.

In this paper, we investigate numerically the stability of these vortex arrays. The goal is to validate the theoretical results and to extend them to finite vertical wavenumbers and to finite vortex separation distances. The paper is organized as follows: the governing equations, the basic states and the numerical method are presented in § 5.2. In § 5.3, the dominant instability is computed and compared to the theoretical predictions for the three vortex arrays for a given Froude number but with a varying Rossby number. In §§ 5.4 and 5.5, the effects of the Froude number and the vortex radius to separation distance ratio are investigated for the Kármán vortex street without background rotation ($Ro = \infty$).

5.2 Problem formulation and numerical procedure

5.2.1 Governing equations

The governing equations are the incompressible Navier–Stokes equations within the Boussinesq approximation in a frame rotating at angular velocity Ω_b about the vertical z-axis:

$$\frac{\partial \boldsymbol{u}}{\partial t} + \boldsymbol{u}\cdot\boldsymbol{\nabla}\boldsymbol{u} + 2\Omega_b \boldsymbol{e}_z \times \boldsymbol{u} = -\frac{1}{\rho_0}\boldsymbol{\nabla} p + b\boldsymbol{e}_z + \nu\boldsymbol{\Delta}\boldsymbol{u}, \tag{5.1a}$$

$$\boldsymbol{\nabla}\cdot\boldsymbol{u} = 0, \tag{5.1b}$$

$$\frac{\partial b}{\partial t} + \boldsymbol{u}\cdot\boldsymbol{\nabla} b + N^2 w = D\Delta b, \tag{5.1c}$$

where $\boldsymbol{u} = (u, v, w)$ is the velocity vector in Cartesian coordinates (x, y, z), ρ_0 a constant reference density, p the pressure, $b = -g\rho/\rho_0$ the buoyancy with ρ the density perturbation with respect to the base density $\rho_0 + \overline{\rho}(z)$, g the gravity and $\boldsymbol{e}_z$ the unit vector in the upward z-direction. $N = \sqrt{-g/\rho_0 \, \mathrm{d}\overline{\rho}/\mathrm{d}z}$ is the Brunt–Väisälä frequency assumed here constant, ν is the kinematic viscosity and D the molecular diffusivity of the stratifying agent.

5.2.2 Basic states

As in part I, the stability of three classical vortex arrays is investigated: (i) the Kármán vortex street, (ii) the symmetric double row and (iii) the single row of co-rotating vortices. A scheme of these configurations is shown in the figure 1 of part I. The Kármán vortex street consists in a staggered double infinite row of two-dimensional vertical vortices of circulation $+\Gamma$ and $-\Gamma$ in the upper and lower row respectively. The vortices on each row are separated by a distance b and the two rows are staggered by a distance $b/2$. The distance between the two rows h is set by the street spacing ratio $\kappa = h/b$. The symmetric double row is similar to the Kármán vortex street except that the two rows are not staggered. The last configuration of interest consists in a single row of co-rotating vortices.

The basic flows $\boldsymbol{U_{2D}}$ corresponding to these vortex arrays are obtained from two-dimensional nonlinear numerical simulations for large Reynolds number $Re = \Gamma/2\pi\nu = 50\,000$ initialized by vortices placed in the required arrangement and each having a Gaussian distribution of vertical vorticity $\omega_z(x, y, t = 0) = \pm(\Gamma/\pi a^2)\exp(-r^2/a^2)$ where a is the vortex radius and r the distance to the axis of the vortex. As time evolves, each vortex rapidly adapts to the strain exerted by each other so that a quasi-steady state $\boldsymbol{U_{2D}}$ is quickly reached (Sipp *et al.* 2000). The Froude number F_h and the Rossby number Ro are based on the initial vortex parameters:

$$F_h = \frac{\Gamma}{2\pi a^2 N}\,, \qquad Ro = \frac{\Gamma}{4\pi a^2 \Omega_b}. \tag{5.2}$$

The numerical simulation is performed with a pseudo-spectral method with periodic boundary conditions. Time advancement is carried out with the classical fourth-order Runge–Kutta scheme for the nonlinear term and exact integration for the viscous term (see Vincent & Meneguzzi 1991 for details). Most of the aliasing is removed by truncating 9/10 of the modes along each direction. Since the base flow is periodic, the computational domain size in the row direction L_x is taken as b, the distance between the vortices on each row. In the other direction, L_y is taken large enough to minimize the effect of the periodic boundary condition. The number of collocation points N_x and N_y are chosen in order to have the same mesh resolution in both directions. The time

label	configuration	a	Γ	b	κ	Re	L_x	L_y	N_x	N_z	δ_t
K0.2	Kármán vortex street	1	2π	15	0.2	50 000	30	38	512	640	0.01
K0.5	Kármán vortex street	1	2π	15	0.5	50 000	30	38	512	640	0.01
D0.5	Symmetric double row	1	2π	15	0.5	50 000	30	38	512	640	0.01
S	Single row	1	2π	15	-	50 000	30	60	512	1024	0.01
K0.2b10	Kármán vortex street	1	2π	10	0.2	50 000	10	38	192	640	0.01
K0.2b7.5	Kármán vortex street	1	2π	7.5	0.2	50 000	7.5	38	128	640	0.01

Table 5.1: Overview of the physical and numerical parameters of the basic states.

step is $\delta_t = 0.01$ in all simulations. The numerical parameters of all the basic states are summarized in table 5.1.

5.2.3 Three-dimensional stability problem

The two-dimensional basic states $\boldsymbol{U_{2D}}$ are subjected to infinitesimal three-dimensional perturbations such that the total flow is of the form:

$$\begin{pmatrix} \boldsymbol{u} \\ p \\ b \end{pmatrix}(x,y,z,t) = \begin{pmatrix} \boldsymbol{U_{2D}} \\ P_{2D} \\ 0 \end{pmatrix}(x,y) + \begin{pmatrix} \tilde{\boldsymbol{u}} \\ \tilde{p} \\ \tilde{b} \end{pmatrix}(x,y,t)\,\mathrm{e}^{\mathrm{i}k_z z + \mathrm{i}\alpha x} + \text{c.c.}, \tag{5.3}$$

where quantities with a tilde have a period b in x-direction, k_z is the vertical wavenumber and $\alpha = 2\pi/\mu b$ measures the periodicity of the perturbation along the row-wise direction. A value $\mu = 2$ represents a perturbation which repeats every two vortices of the basic state, i.e. with a period $2b$, $\mu = 4$ is a perturbation which repeats every 4 vortices etc. while $\mu = \infty$ represents a perturbation which repeats in x with the same periodicity as the base flow. Here, we have restricted the analysis to the values $\mu = 2$ (subharmonic) and $\mu = \infty$ (fundamental) for which the theory predicts the dominant modes to exist. The flow decomposition (5.3) is inserted in (5.1) and the equations are linearized around the base state.

The linearized equations are integrated numerically for each k_z and μ values using a linearized pseudo-spectral code similar to the one described in § 5.2.2. The size of the computational domain and the number of collocation points are identical to those used to compute the corresponding basic state $\boldsymbol{U_{2D}}$. The Schmidt number $Sc = \nu/D$ is set to unity $Sc = 1$. The perturbation velocity $\tilde{\boldsymbol{u}}(x,y,t=0)$ is initialized with a divergence free white noise. After integrating the linearized equations for a sufficiently long time, typically $T = 2400\pi a^2/\Gamma$, the eigenmode with the largest growth rate dominates over the perturbation and we can retrieve its structure and growth rate.

5.3 Strongly stratified and rotating fluid: effect of the Rossby number

In this section, we present the numerical results for a given fixed Froude number $F_h = 0.1$ and various Rossby numbers and compare them to the asymptotic results of part I. The latter analysis is asymptotically valid when the fluid is inviscid and the vortices well-separated. In the computations, we have therefore first investigated a small ratio of the core radius of the vortices over their separation distance $a/b = 0.067$ for a large Reynolds number $Re = 50\,000$. This corresponds to the basic states labelled K0.2, K0.5, D0.5 and S in table 5.1. The effective ratio a/d where d is the minimum distance between vortices is however larger and reaches a value as large as $a/d = 0.133$ for the symmetric double row for $\kappa = 0.5$. The results for the three different vortex arrays are described successively.

5.3.1 Kármán vortex street

Figure 5.1(a) shows the case of the Kármán vortex street with close rows $\kappa = 0.2$. The nondimensional growth rate $2\pi b^2\sigma/\Gamma$ of the dominant mode as a function of the rescaled vertical wavenumber bF_hk_z is presented for different Rossby numbers from no background rotation ($Ro = \infty$) to high rotation ($Ro = 0.75$). In this case, the instability is three-dimensional and the rotation decreases the most amplified wavenumber and maximum growth rate. As expected, there is a perfect agreement for small values of k_z between the numerical simulations (symbols) and the theoretical results of part I (solid lines). Small departures at large wavenumbers are observed because the asymptotic theory is restricted to long-wavelength disturbances. Nevertheless, the agreement is quite good and the theory predicts very well the most unstable vertical wavenumber $k_{z\,max}$ and the maximum growth rate.

Figure 5.2(a) shows the vertical vorticity field $\tilde{\omega}_z$ of the most amplified perturbation for the non-rotating case ($Ro = \infty$). We see that the perturbations are localized in the vortex cores and consist for each vortex in two regions of opposite vorticity. If this perturbation were added to the basic flow, it would correspond to translations of the vortices in the direction indicated by the arrows. Besides, this mode is symmetric with respect to the middle plane between the two rows and all the vortices of a given row are displaced in the same direction meaning that $\mu = \infty$. This is in full agreement with the dominant eigenmode predicted by the theoretical study of part I which is also shown in figure 5.2(b).

We further show in figure 5.3(a) the most amplified eigenmode for a typical rotating case ($Ro = 2$). The eigenmode is not perfectly symmetric because symmetric and antisymmetric modes do not decouple for finite Rossby numbers

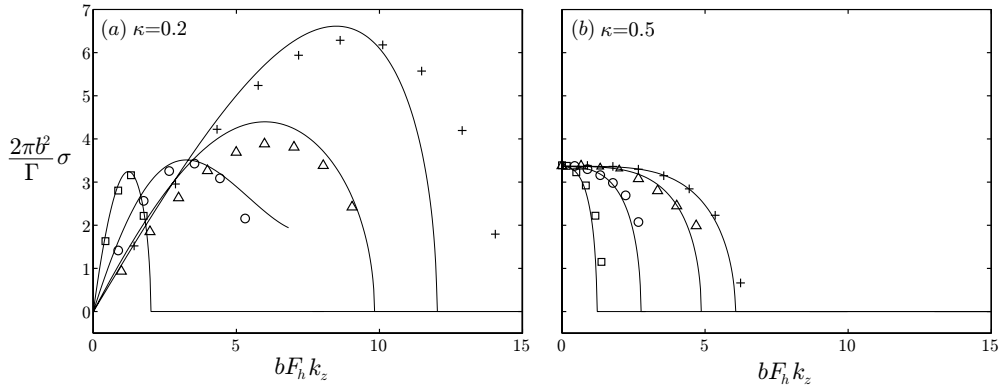

Figure 5.1: Nondimensional growth rate $2\pi b^2\sigma/\Gamma$ of the dominant mode as a function of the rescaled vertical wavenumber $bF_h k_z$ for $F_h = 0.1$ for the Kármán vortex street with (a) close rows $\kappa = 0.2$ and (b) distant rows $\kappa = 0.5$. The symbols correspond to the numerical results and the solid lines to the asymptotic theory. In each plot, the curves from right to left correspond to the Rossby numbers: $Ro = \infty$ (+), $Ro = 6$ ($\triangle$), $Ro = 2$ ($\circ$), $Ro = 0.75$ ($\square$).

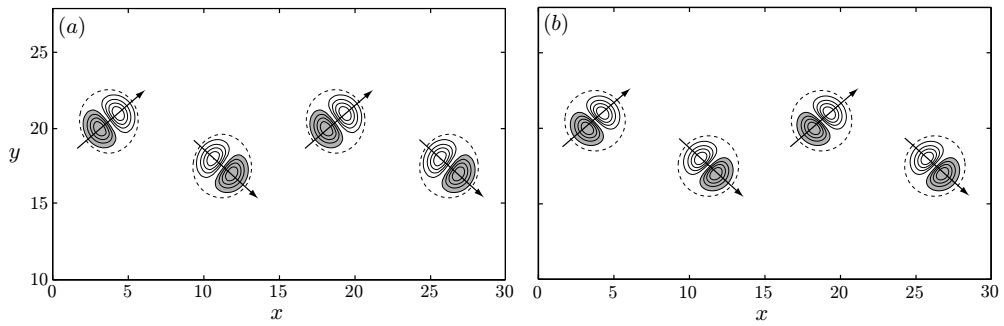

Figure 5.2: Contours of the vertical vorticity $\tilde{\omega}_z$ of the most amplified perturbation in a stratified and non-rotating fluid ($F_h = 0.1$, $Ro = \infty$) of the Kármán vortex street with close rows $\kappa = 0.2$ for $F_h = 0.1$. The left figure (a) corresponds to the numerical results and the right figure (b) to the asymptotic theory. The arrows denote the directions of displacement of each vortex due to the instability. The dominant instability is a three-dimensional symmetric zigzag instability. Only a domain of size 30×18 is shown while the original computational domain is 30×38. Shaded areas are regions of negative values. The dotted line indicates the boundary $r = 2a$ of the vortices of the basic state.

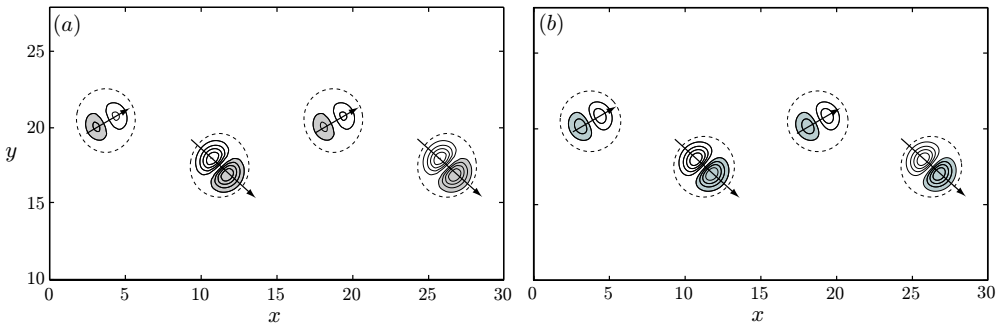

Figure 5.3: Similar to figure 5.2 but in a rotating fluid with $Ro = 2$.

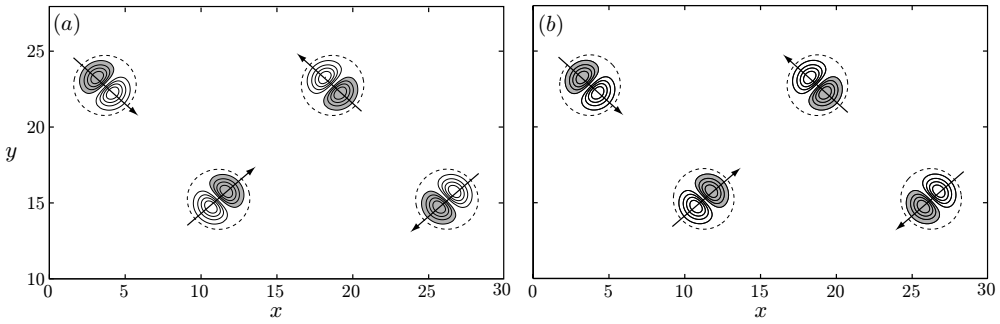

Figure 5.4: Similar to figure 5.2 but for the Kármán vortex street with distant rows $\kappa = 0.5$. The dominant instability is a two-dimensional pairing mode.

(part I). The vortices in the lower row which are anticyclonic are more displaced by the zigzag instability than the cyclonic vortices in the upper row. This is in full agreement with the theoretical predictions (figure 5.3*b*).

Figure 5.1(*b*) is similar to 5.1(*a*) but for a Kármán vortex street with more distant rows $\kappa = 0.5$. In this case, the most unstable mode is two-dimensional ($k_{z\,max} = 0$) and oscillatory (the frequency is not shown). The agreement between numerical (symbols) and theoretical (solid lines) results is excellent over almost all the unstable band of vertical wavenumbers k_z. Figure 5.4(*a*) shows its vertical vorticity field $\tilde{\omega}_z$ at one instant. Adjacent vortices of the same row are displaced in opposite direction and tend to merge. This mode corresponds to a pairing mode in full agreement with the theoretical eigenmode predicted in part I (figure 5.4*b*). Note that this eigenmode is not affected by background rotation because it is two-dimensional.

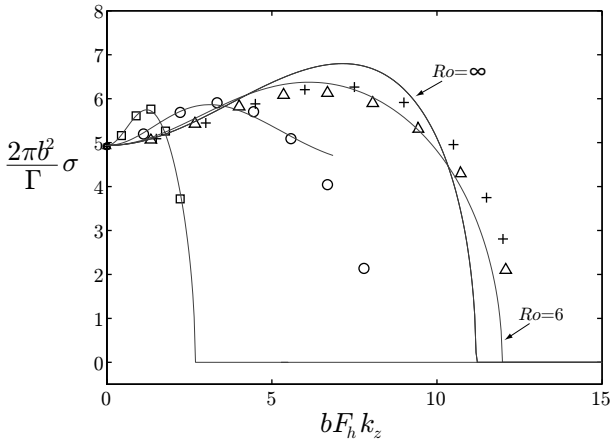

Figure 5.5: Similar to figure 5.1 but for the symmetric double row with $\kappa = 0.5$. We recall that the symbols correspond to: $Ro = \infty$ (+), $Ro = 6$ ($\triangle$), $Ro = 2$ ($\circ$), $Ro = 0.75$ ($\square$).

5.3.2 Symmetric double row

We show in figure 5.5 the growth rate of the dominant mode in the case of the symmetric double row with $\kappa = 0.5$. The same Rossby numbers than in the previous section are presented. The dominant instability is three-dimensional although two-dimensional perturbations are also unstable. As before, the most amplified wavenumber decreases when Ro decreases but the corresponding maximum growth rate is only slightly reduced. The agreement between numerical (symbols) and theoretical (solid lines) results is again excellent for small wavenumbers and good for large wavenumbers. Figure 5.6(a) shows the vertical vorticity field $\tilde{\omega}_z$ of the most amplified perturbation in the non-rotating case ($Ro = \infty$). Adjacent vortices of a given row are displaced in opposite direction and antisymmetrically with respect to the other row. The dominant mode corresponds therefore to an antisymmetric $\mu = 2$ three-dimensional instability in remarkable agreement with the mode predicted by the theory (figure 5.6b). As seen in figure 5.7(a, b), the eigenmode when there is a background rotation ($Ro = 2$) is similar but not exactly antisymmetric. Like for the Kármán vortex street, the anticyclonic vortices in the lower row are more displaced than the cyclonic vortices in the upper row.

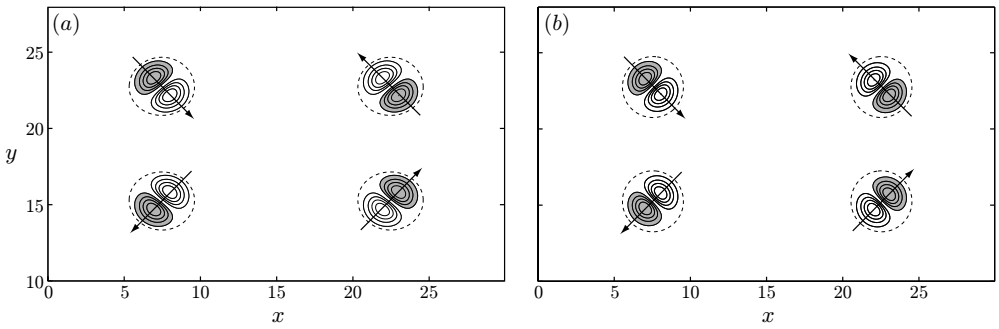

Figure 5.6: Similar to figure 5.2 but for the symmetric double row with $\kappa = 0.5$. The dominant instability is a three-dimensional antisymmetric zigzag mode.

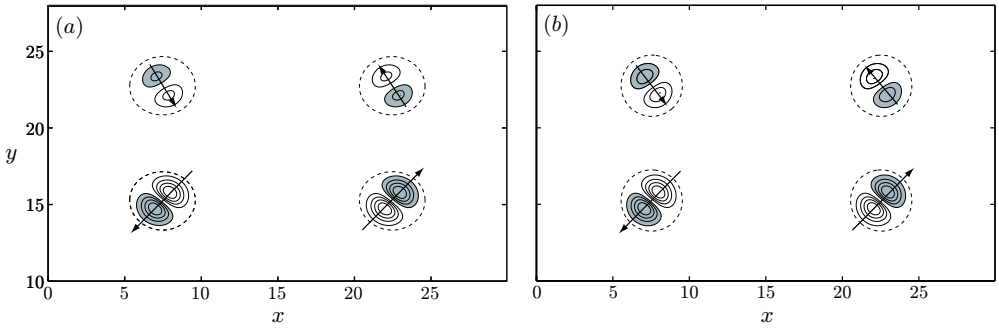

Figure 5.7: Similar to figure 5.2 but for the symmetric double row with $\kappa = 0.5$ and in a rotating fluid with $Ro = 2$.

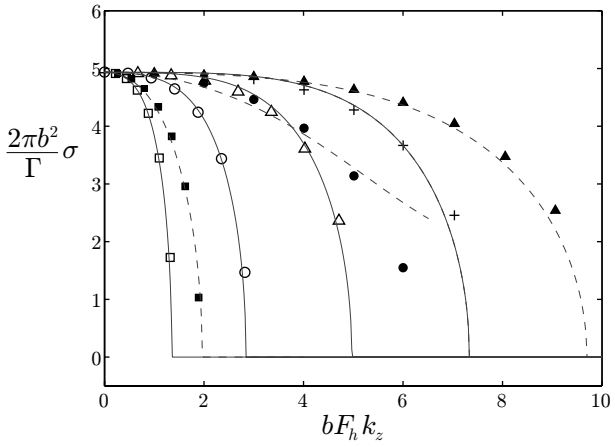

Figure 5.8: Similar to figure 5.1 but for the single row of co-rotating vortices. The numerical results are represented by open symbols for positive Rossby numbers: $Ro = \infty$ (+), $Ro = 6$ (△), $Ro = 2$ (○), $Ro = 0.75$ (□) and by filled symbols for negative Rossby numbers: $Ro = -6$ (▲), $Ro = -2$ (●), $Ro = -0.75$ (■). The corresponding theoretical results are shown by solid lines for positive Ro and dashed lines for negative Ro.

5.3.3 Single row

Finally, we show in figure 5.8 the growth rate of the dominant mode of the single row. For this configuration[1], the vortices of the base flow have all the same sign so that cyclonic ($Ro > 0$) and anticyclonic ($Ro < 0$) background rotations differ and need to be considered. The dominant mode is always two-dimensional but the width of the unstable wavenumber band depends on Ro and is different for cyclonic and anticyclonic rotations. There is an excellent agreement between numerical (symbols) and theoretical (solid lines) results except for $Ro = 2$ where a departure is observed at large wavenumbers. The eigenmode (not shown) corresponds to the pairing instability and has the same spatial structure as the one seen in figure 5.4 for each row of the Kármán vortex street.

[1]In this case, the base flow is not periodic in the y-direction since the velocity for $y \to \pm\infty$ is constant but in opposite direction. Therefore the base flow can not be computed directly with a pseudo-spectral code. To circumvent this difficulty, a symmetric double row with $\kappa = 8$, i.e. with almost independent rows, has been first computed. Half of this flow, i.e. one row, has been taken here as basic state.

5.4 Stratified and non-rotating fluid: effect of the Froude number

We now set the Rossby number to $Ro = \infty$ (no background rotation) and investigate the effect of the Froude number for the Kármán vortex street with $\kappa = 0.2$. Figure 5.9 shows the growth rate of the dominant mode for various Froude numbers from strong stratification ($F_h = 0.1$) to moderate stratification ($F_h = 1.2$). In all cases, the agreement between numerical (symbols) and theoretical (solid lines) results is very good although a slight departure is observed at large wavenumbers. We see that the growth rate curves for $F_h = 0.1$ and $F_h = 1$ are almost similar except a small decrease in the most amplified wavenumber. The stratification has thus little effect on the zigzag instability as long as $F_h < 1$. However, when the Froude number is further increased to $F_h = 1.2$, an abrupt drop of 50% of the maximum growth rate is observed. Billant *et al.* (2007) have shown that this is due to the damping of the zigzag instability by a viscous critical layer that appears for $F_h > 1$. This is confirmed by figure 5.10 that shows the corresponding numerical eigenmode: the viscous critical layer is clearly distinguishable in each vortex core, as the radius where the angular velocity of the vortex is equal to the Brunt–Väisälä frequency. If the Froude number were further increased to $F_h \approx 1.3$, the maximum growth rate would be even more reduced and would eventually become lower than the maximum growth rate of the $\mu = 2$ two-dimensional pairing instability ($2\pi b^2 \sigma_{max}/\Gamma \approx 2$, see part I).

5.5 Strongly stratified and non-rotating fluid: effect of the vortex radius to separation distance ratio: a/b

We now investigate the effect of the vortex radius to separation distance ratio a/b for the Kármán vortex street with $\kappa = 0.2$ for a fixed set of Froude and Rossby numbers ($F_h = 0.1$, $Ro = \infty$). Figure 5.11 shows the growth rate of the dominant mode for various ratios a/b from well-separated vortices ($a/b = 0.067$) to very close vortices ($a/b = 0.133$). These cases correspond to the basic states labelled K0.2, K0.2b10 and K0.2b7.5 in table 5.1. We recall that the effective ratio a/d where d is the minimum distance between vortices is even larger and goes here from $a/d = 0.124$ to $a/d = 0.248$. As the vortices get closer, the maximum growth rate decreases slightly and the band of unstable vertical wavenumbers widens. We see a departure between the numerical results (dotted line with symbols) and the asymptotic theory (solid line) which is only valid for well-separated vortices (i.e. at leading order in a/b). However, the instability remains of the same nature as for well-separated vortices.

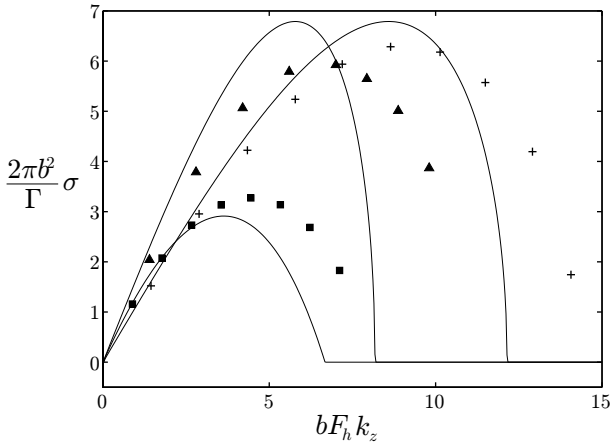

Figure 5.9: Nondimensional growth rate $2\pi b^2\sigma/\Gamma$ of the dominant mode as a function of the rescaled vertical wavenumber $bF_h k_z$ with $Ro = \infty$ for the Kármán vortex street with close rows $\kappa = 0.2$. The symbols correspond to the numerical results and the solid lines to the asymptotic theory. The curves from right to left correspond to the Froude numbers: $F_h = 0.1$ (+), $F_h = 1.$ (▲), $F_h = 1.2$ (■).

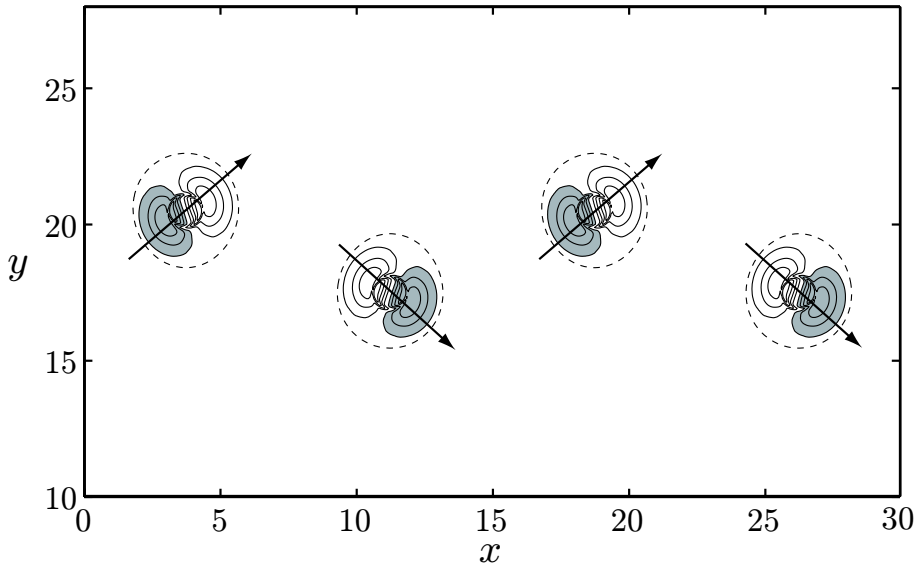

Figure 5.10: Similar to figure 5.2 but for a Froude number $F_h = 1.2$. We see viscous critical layers in the vortex cores.

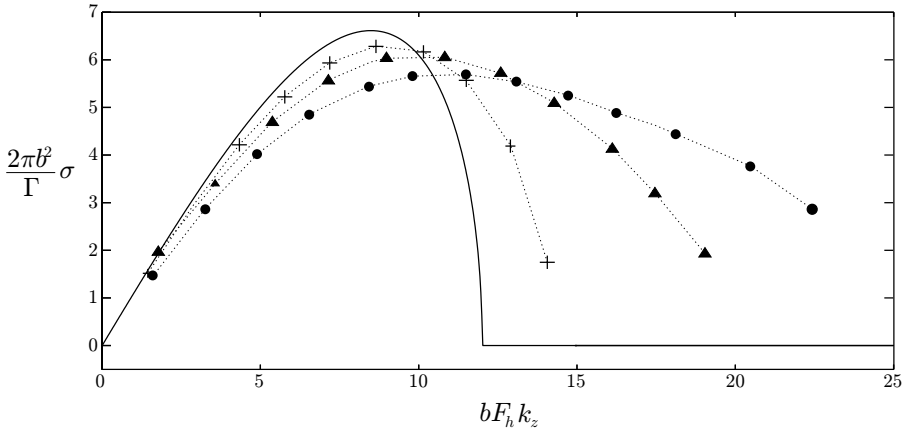

Figure 5.11: Nondimensional growth rate $2\pi b^2\sigma/\Gamma$ of the dominant mode as a function of the rescaled vertical wavenumber $bF_h k_z$ with $F_h = 0.1$ and $Ro = \infty$ for the Kármán vortex street with $\kappa = 0.2$. The dotted lines with symbols correspond to numerical results and the solid line to the asymptotic theory valid for well-separated vortices. Different vortex radius to separation distance ratios are presented: $a/b = 0.067$ (+), $a/b = 0.100$ (▲), $a/b = 0.133$ (•).

5.6 Conclusion

We have investigated numerically the three-dimensional stability of arrays of columnar vortices in a stratified and rotating fluid for high Reynolds number. The results for the Kármán vortex street, the symmetric double row and the single row are in excellent agreement with the asymptotic stability analysis of part I for all the Rossby and Froude numbers investigated.

This agreement proves first that the asymptotic theory is fully valid over a wide range of conditions and that it captures the physics of the instabilities due to the vortex interactions in stratified and rotating fluids. Furthermore, we have shown that the theory works very well for finite wavelengths and quite well for close vortices despite the two assumptions used in the asymptotics: long-wavelength bending perturbations and well-separated vortices. This should give us confidence to use the theory to predict the stability of any other vortex configuration. It should be useful since numerical stability analysis as performed here require huge computing resources compared to the theory.

Second, the present numerical stability analysis proves that displacement perturbations of vortices, either two-dimensional or three-dimensional (i.e. bending perturbations) are the most unstable in stratified and rotating fluids. We have not found any other perturbations of a different nature which would be more unstable, at least over the range of vertical wavenumbers investigated.

If we summarize the stability results, we have found that when the fluid is sufficiently stratified (i.e. $F_h \leq F_{hc}$ where $F_{hc} \approx 1.3 - 1.6$ depending on the parameters of the arrays), the instability is three-dimensional whatever the Rossby number for both the Kármán vortex street with close rows and the symmetric double row for any street spacing ratio. It is a bending instability of the same type as the zigzag instability of vortex pairs. This instability might explain the destabilization of the Kármán vortex streets observed experimentally in stratified fluids by Holford & Linden (1999) and Praud *et al.* (2005). The Kármán vortex street for distant rows and the single row are most unstable to a two-dimensional pairing instability for any Rossby number.

Chapter 6

Stability of unsteady vortex distributions

6.1 Introduction

In chapters 4 and 5, we have shown that various configurations of infinite vortex arrays are subject to the zigzag instability, extending the previous results obtained on pairs of counter- (Billant & Chomaz 2000*b*) and co-rotating vortices (Otheguy *et al.* 2006). This suggests that the zigzag instability should be a generic mechanism that applies on many vorticity distributions with any number of vortices.

However, the previous studies were performed only on basic states that are steady in a frame of reference, allowing to determine the most unstable linear perturbations. Although these configurations can be observed in nature, atmospheric and oceanic flows usually exhibit more complex vortical distributions. In this chapter, we have therefore performed direct numerical simulations (DNS) of unsteady distributions of columnar vertical vortices in order to determine whether the zigzag instability still applies in more realistic flows.

6.2 Numerical method

The NS3D code, already presented in chapter 2, is used to solve the nonlinear incompressible Navier–Stokes equations under the Boussinesq approximation. We recall that it is a pseudo-spectral method with periodic boundary conditions and that time advancement is carried out with the classical fourth-order Runge–Kutta scheme for the nonlinear term and exact integration for the viscous and diffusive terms.

Several DNS were performed with a different total number N of vertical columnar vortices. In each run, the velocity field is initialized with an equal

Run	N	F_h	Re	Sc	a	b_{min}	$L_x \times L_y \times L_z$	$N_x \times N_y \times N_z$	δ_t
N6	6	0.8	1060	1	1	2	$50 \times 50 \times 12.5$	$128 \times 128 \times 32$	0.08
N10	10	0.8	1060	1	1	2	$50 \times 50 \times 12.5$	$128 \times 128 \times 32$	0.08
N20	20	0.8	1060	1	1	2	$50 \times 50 \times 12.5$	$128 \times 128 \times 32$	0.08

Table 6.1: Overview of the physical and numerical parameters of the simulations performed in this chapter.

number $N/2$ of vortices having a positive $+\Gamma$ and negative $-\Gamma$ circulation. Each vortex is initially two-dimensional and has a Gaussian distribution of vertical vorticity $\omega_z(t=0) = \pm(\Gamma/\pi a^2)\exp(-r^2/a^2)$ where a is the vortex radius and r the distance to the axis of the vortex. The initial positions of the vortices are random but we impose a minimum distance b_{min} between them. A low-level, white noise is added to the initial velocity field in order to break the two-dimensionality of the flow and to excite any existing three-dimensional instability.

The Reynolds number Re and the Froude number F_h are based on the initial conditions:

$$Re = \frac{\Gamma}{2\pi\nu}, \qquad F_h = \frac{\Gamma}{2\pi a^2 N}, \tag{6.1}$$

where ν is the kinematic viscosity and N the Brunt–Väisälä frequency. The Schmidt number $Sc = \nu/D$, where D is the mass diffusivity, is set to unity in all runs. In the sequel, the time unit is taken as $2\pi a^2/\Gamma$, the length unit as a.

The computational domain size is $L_x \times L_y \times L_z$ and the number of collocation points N_x, N_y and N_z are chosen so as to have the same mesh resolution in all directions. Time step is δ_t. The numerical parameters of all the initial states are summarized in table 6.1.

6.3 Results

6.3.1 Qualitative behaviour

Figure 6.1 shows the temporal evolution of the vertical vorticity isosurfaces for the run labelled N10 in table 6.1. At the beginning ($t = 0$), the vortices are straight along the vertical since the three-dimensional white noise is very small and no instability has developed. In a first step between $t = 0$ and $t = 20$, the dynamics remains two-dimensional: the vortices are advected by each other like two-dimensional point vortices. By $t = 41$, we see that several vortices are bent as a whole by the zigzag instability. For instance, the pair of vortices labelled $g1$ on the figure exhibit a very regular zigzag pattern. Subsequently, the amplitude of the bending deformation continues to grow. At $t = 48$, the two vortices are extremely distorted and at $t = 50$, they have almost disappeared, indicating that a strong dissipation has occurred. A similar behaviour is observed for

the group of vortices labelled $g2$ although the zigzag pattern is a little bit defected. At final time $t = 90$, all the vortices have been dissipated and only pancake vortices remain. Note that a strong dissipation has occurred since the isosurfaces shown are only 10% of the initial values.

6.3.2 Effects of the number of vortices

Figure 6.2 shows characteristic times of the evolution of the three simulations labelled N6, N10 and N20, corresponding to 6,10 and 20 initial vortices, respectively. The time of each run is adjusted so as to capture the early development of the zigzag instability. In all simulations, we see the bending of the vortices due to the zigzag instability. However, as already noticed in § 6.3.1, the zigzag pattern becomes more defected when more vortices are interacting, which is more likely to occur for a large number of vortices. The instabilities develop much more regularly in the $N = 6$ case (figure 6.2a) compared to the $N = 20$ case (figure 6.2c).

6.4 Conclusion

In this chapter, we have studied the three-dimensional stability of unsteady two-dimensional flows: random distributions of vertical columnar vortices. These flows were found to be unstable to the zigzag instability with a zigzag pattern that becomes more distorted when a large number of vortices are interacting. This confirms that the zigzag instability is a robust mechanism that applies for a large range of flows.

We have seen that the nonlinear development of the zigzag instability always leads to the apparition of pancake vortices associated with a strong dissipation of energy. The relatively low Reynolds numbers and mesh resolutions used in the present simulations have not allowed us to investigate closely the corresponding energy transfers. This is the object of chapter 7.

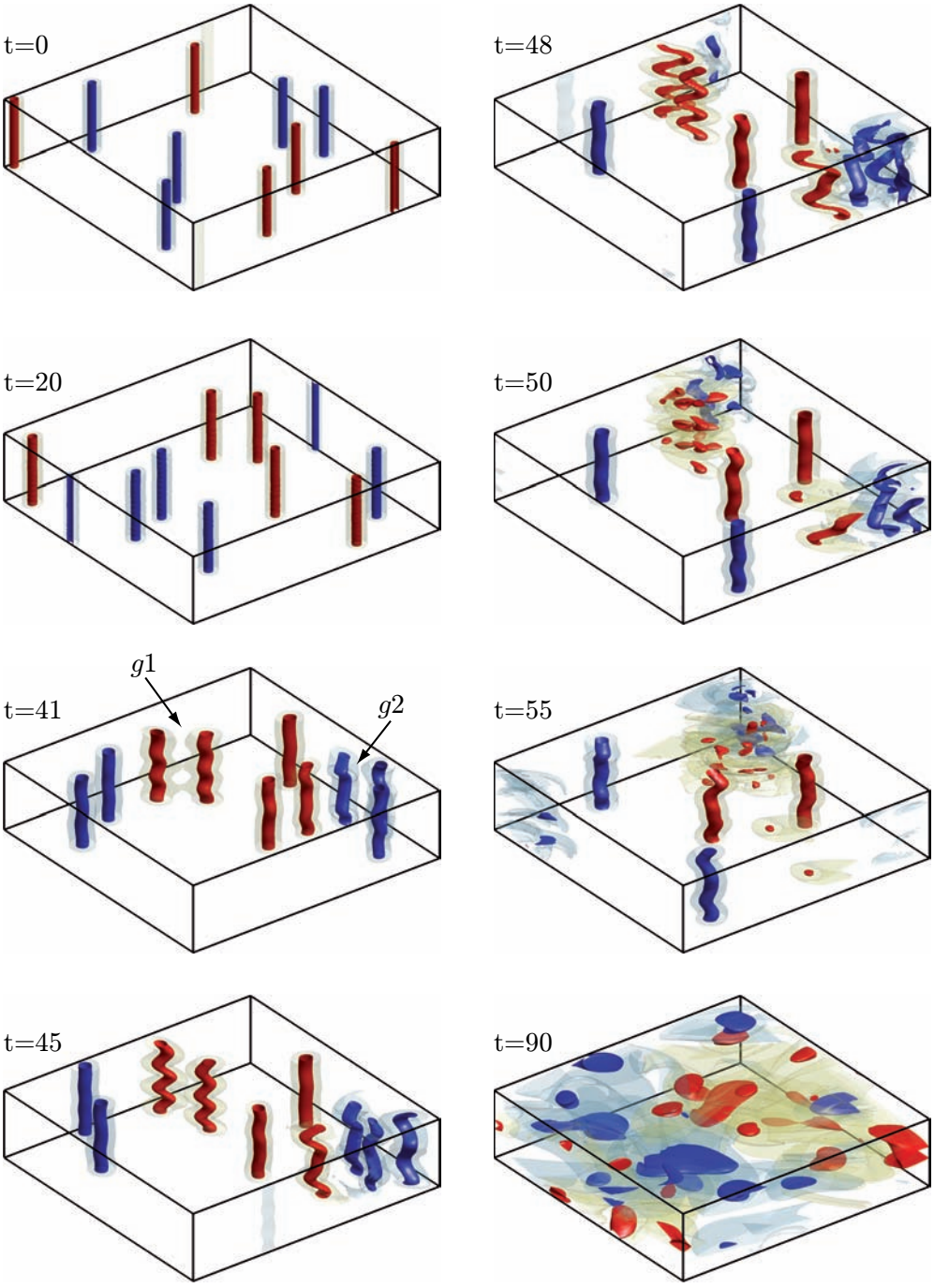

Figure 6.1: Vertical vorticity isosurfaces of the simulation N10. Red and deep blue contours represent respectively plus and minus 60% of $\langle \omega_z^{max} \rangle_z$, the vertical average of the maximum vertical vorticity in each horizontal plane. Transparent yellowish and bluish isosurfaces are the same for a 10% level.

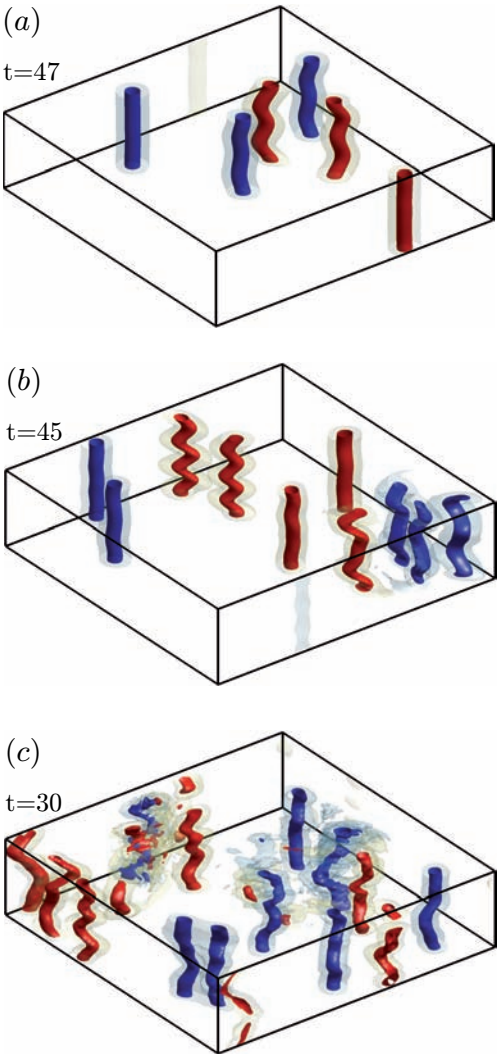

Figure 6.2: Similar to figure 6.1 but for the simulations N6 (a), N10 (b) and N20 (c) corresponding to 6, 10 and 20 initial vortices, respectively. Time for each run is adjusted so as to capture the early development of the zigzag instability.

Chapter 7

Nonlinear evolution of a pair of counter-rotating vortices

Article submitted to the *Journal of Fluid Mechanics*.

Nonlinear evolution of the zigzag instability in stratified fluids: a shortcut on the route to dissipation

By AXEL DELONCLE, PAUL BILLANT AND JEAN-MARC CHOMAZ

Hydrodynamics Laboratory (LadHyX), Ecole Polytechnique,
91128 Palaiseau Cedex, France
axel.deloncle@ladhyx.polytechnique.fr

(Submitted to the *Journal of Fluid Mechanics*)

We present high-resolution direct numerical simulations of the nonlinear evolution of a pair of counter-rotating vertical vortices in a stratified fluid for various high Reynolds numbers Re and low Froude numbers F_h. The vortices are bent by the zigzag instability producing high vertical shear. There is no nonlinear saturation so that the exponential growth is stopped only when the viscous dissipation by vertical shear is of the same order as the horizontal transport, i.e. when $Z^h_{max}/Re = O(1)$ where Z^h_{max} is the maximum horizontal enstrophy nondimensionalized by the vortex turn-over frequency. The zigzag instability therefore transfers directly the energy from large scales to the small dissipative vertical scales. However, for high Reynolds number, the vertical shear created by the zigzag instability is so intense that the minimum local Richardson number Ri decreases below a threshold around 1/4 and small-scale Kelvin–Helmholtz instabilities develop. We show that this can only occur when ReF_h^2 is above a threshold estimated to 340.

7.1 Introduction

In a strongly stratified fluid, pairs of counter-rotating and co-rotating vertical vortices are subject to the zigzag instability (Billant & Chomaz 2000*a*; Otheguy *et al.* 2006). This linear three-dimensional instability bends the vortices with a most unstable vertical wavelength scaling like the buoyancy length scale bF_h where b is the distance between the two vortices and F_h the horizontal Froude number ($F_h = \Gamma/2\pi a^2 N$ with a the vortex cores radius, Γ their circulation and N the Brunt–Väisälä frequency) and develops with a growth rate proportional to the strain $\Gamma/2\pi b^2$.

In the experiments of Billant & Chomaz (2000*a*), the zigzag instability of a counter-rotating vortex pair grows to a large amplitude and produces layers of pancake dipoles separated by regions of extreme vertical shear. However, in

these experiments, the Reynolds number is relatively low whereas atmospheric and oceanic flows have high Reynolds numbers. We have therefore performed direct numerical simulations (DNS) of the zigzag instability of a pair of counter-rotating vortices at high Reynolds number in order to understand the nonlinear development of this linear instability and the resulting energy transfer.

7.2 Numerical method

A pseudo-spectral method with periodic boundary conditions is used to solve the nonlinear incompressible Navier–Stokes equations under the Boussinesq approximation. Time advancement is carried out with the classical fourth-order Runge–Kutta scheme for the nonlinear term and exact integration for the viscous and diffusive terms (see Vincent & Meneguzzi 1991 for details). Most of the aliasing is removed by truncating 9/10 of the modes along each direction.

The velocity field of the DNS is initialized as:

$$\boldsymbol{U}(x,y,z,t=0) = \boldsymbol{U_{2D}}(x,y) + \epsilon\cos(k_{z\,max}z)\boldsymbol{U_p}(x,y), \tag{7.1}$$

where $\boldsymbol{U_{2D}}$ is a two-dimensional flow representing a quasi-steady vortex pair, $\boldsymbol{U_p}$ its most unstable three-dimensional zigzag eigenmode with vertical wavenumber $k_{z\,max}$, ϵ a chosen small amplitude, z the vertical coordinate and (x,y) the horizontal Cartesian coordinates.

The flow $\boldsymbol{U_{2D}}$ is obtained from a two-dimensional nonlinear simulation initialized by a pair of counter-rotating Gaussian vortices of circulation $\pm\Gamma$, radius a and separated by a distance $b = 2.5a$, corresponding to the vertical vorticity $\omega_z(x,y) = \Gamma/\pi a^2[\exp(-(x^2 + y^2)/a^2) - \exp(-(x^2 + (y+b)^2)/a^2]$. As time evolves, each vortex rapidly adapts to the strain exerted by the other one so that a quasi-steady state $\boldsymbol{U_{2D}}$ is quickly reached (Sipp *et al.* 2000). The initial state is presented at $t = 0$ in figure 7.1(a).

The Reynolds number Re and the Froude number F_h are based on the initial conditions:

$$Re = \frac{\Gamma}{2\pi\nu}, \qquad F_h = \frac{\Gamma}{2\pi a^2 N}, \tag{7.2}$$

where ν is the kinematic viscosity and N the Brunt–Väisälä frequency. The Schmidt number $Sc = \nu/D$, where D is the mass diffusivity, is set to unity in all runs. In the sequel, the time unit is taken as $2\pi a^2/\Gamma$, the length unit as a and the density unit as $a\,|\mathrm{d}\rho_0/\mathrm{d}z|$ where $\rho_0(z)$ is a reference density.

The flow $\boldsymbol{U_p}$ is the most unstable three-dimensional perturbation of $\boldsymbol{U_{2D}}$ determined by a numerical linear stability analysis for each Froude number. Since $F_h < 1$, it corresponds to the eigenmode of the zigzag instability with a

Run	F_h	Re	$R = ReF_h^2$	Sc	a	b	$k_{z\,max}$	$L_x \times L_y \times L_z$	$N_x \times N_y \times N_z$	δ_t
F0.6R1	0.66	1060	460	1	1	2.5	2.2	$10.5 \times 10.5 \times 2.85$	$256 \times 256 \times 64$	0.04
F0.6R3	0.66	3180	1380	1	1	2.5	2.2	$10.5 \times 10.5 \times 2.85$	$384 \times 384 \times 96$	0.02
F0.6R6	0.66	6360	2770	1	1	2.5	2.2	$10.5 \times 10.5 \times 2.85$	$768 \times 768 \times 192$	0.01
F0.3R4	0.33	4240	460	1	1	2.5	4.4	$10.5 \times 10.5 \times 1.425$	$512 \times 512 \times 72$	0.02
F0.3R12	0.33	12 720	1380	1	1	2.5	4.4	$10.5 \times 10.5 \times 1.425$	$1440 \times 1440 \times 192$	0.004

Table 7.1: Overview of the physical and numerical parameters of the main simulations described in the paper. The number of nodes in the x-,y- and z-direction are denoted, respectively, N_x, N_y and N_z. The time step is δ_t.

most amplified wavenumber $k_{z\,max}$ proportional to F_h in agreement with the linear theory of the zigzag instability (Billant & Chomaz 2000*b*).

The parameters of each run are summarized in table 7.1. The height of the computational domain L_z is adjusted so as to have only one wavelength in the box. The horizontal size of the box $L_x = L_y = 10.5$ is taken sufficiently large compared to the distance between the two vortices in order to have negligible effects of the periodic boundary conditions. Furthermore, several additional cases were run, changing the domain size and/or the numerical resolution, in order to test the accuracy and robustness of the results presented. The results of these additional runs were consistent with those presented in the following, and so will not be discussed.

7.3 Qualitative behaviour

The zigzag instability exhibits two different nonlinear evolutions depending on the Reynolds and Froude numbers. Figure 7.1 shows the temporal evolution of the vertical vorticity isosurfaces for these two distinct behaviours: figure 7.1(a) for run F0.6R1 ($F_h = 0.66$, $Re = 1060$) and figure 7.1(b) for run F0.6R3 ($F_h = 0.66$, $Re = 3180$). The corresponding movies can be viewed on the on-line version of the journal alongside the paper. At the beginning ($t = 0$), the two vortices are straight along the vertical since the three-dimensional perturbation is very small. By $t = 50$, the vortices are bent as a whole by the zigzag instability. Subsequently, the amplitude of the bending deformations for run F0.6R1 continues to grow dramatically without apparent saturation ($t = 70$, $t = 105$) as observed experimentally (Billant & Chomaz 2000*a*). This eventually produces decorrelated thin horizontal layers ($t = 160$), but at that time a strong dissipation has occurred since the isosurfaces shown are only 12% of the initial values. A distinctly different behaviour is observed at the intermediate times ($t = 70$, $t = 105$) for a higher Reynolds number (run F0.6R3, figure 7.1b). Small-scale three-dimensional structures develop in the highly sheared region of the vortices so that the vortices breakdown.

However, at late time ($t = 160$), smooth decorrelated layers are seen again like in figure 7.1(a).

7.4 Energy and enstrophy analysis

Figure 7.2(a) shows the temporal evolution of the total kinetic energy $E_k^T = \langle \boldsymbol{u} \cdot \boldsymbol{u} \rangle / 2$ (where $\boldsymbol{u}$ is the velocity and $\langle \, . \, \rangle$ denotes the volume integral per unit vertical length: $\langle \, . \, \rangle = 1/L_z \int_V \, . \, \mathrm{d}V$) as well as its horizontal E_k^h and vertical E_k^v components for a typical run: F0.6R1. Almost all the kinetic energy is contained in the horizontal motion which confirms that vertical displacements are inhibited by stratification. Up to $t \sim 40$, the evolution of the total kinetic energy (solid line) is identical to the one of a purely two-dimensional flow without zigzag instability (■ symbols). Then a strong decrease of kinetic energy is observed when the zigzag instability develops. The potential energy $E_p = \langle \rho^2 \rangle / 2F_h^2$ where ρ is the nondimensional density perturbation (see, e.g., Gill 1982 for a detailed discussion of potential energy) is also shown in figure 7.2(a) (dash-dot line) but it remains always negligible compared to the kinetic energy.

Figure 7.2(b) presents the temporal evolution of the total enstrophy $Z^T = \langle \boldsymbol{\omega} \cdot \boldsymbol{\omega} \rangle / 2$ where $\boldsymbol{\omega}$ is the vorticity and its horizontal Z^h and vertical Z^v components. The total enstrophy first decreases like in the two-dimensional case up to $t \sim 40$, then strongly increases up to $t \sim 90$ and eventually relaxes. The vertical enstrophy decreases steadily whereas the horizontal enstrophy grows exponentially owing to the development of the zigzag instability from $t = 0$ up to $t \sim 70$ as demonstrated by the inserted graph in figure 7.2(b). It then saturates around $t \sim 80$ when the decrease of energy is the fastest.

These behaviours can be understood by looking at the total energy equation in nondimensional form:

$$\frac{\mathrm{d}(E_k^T + E_p)}{\mathrm{d}t} = -2\frac{Z^T}{Re} - \frac{1}{ReSc}\frac{\langle \boldsymbol{\nabla}\rho \cdot \boldsymbol{\nabla}\rho \rangle}{F_h^2}. \tag{7.3}$$

Figure 7.3(a) presents the temporal evolution of the two dissipative processes of (7.3): we see that the kinetic energy dissipation (first term at the right-hand side of (7.3)) is largely dominant over the potential energy dissipation (second term at the right-hand side of (7.3)). The kinetic energy dissipation is directly related to the total enstrophy whose equation in nondimensional form is:

$$\frac{\mathrm{d}Z^T}{\mathrm{d}t} = \langle \boldsymbol{\omega} \cdot (\boldsymbol{\omega} \cdot \boldsymbol{\nabla}\boldsymbol{u}) \rangle - \frac{1}{F_h^2}\langle \boldsymbol{\omega} \cdot \boldsymbol{\nabla} \times (\rho \boldsymbol{e}_z) \rangle - \frac{1}{Re}\langle \boldsymbol{\nabla}\boldsymbol{\omega} : \boldsymbol{\nabla}\boldsymbol{\omega} \rangle. \tag{7.4}$$

The three terms at the right-hand side of (7.4) correspond respectively to stretching, baroclinic and viscous effects. The temporal evolution of these

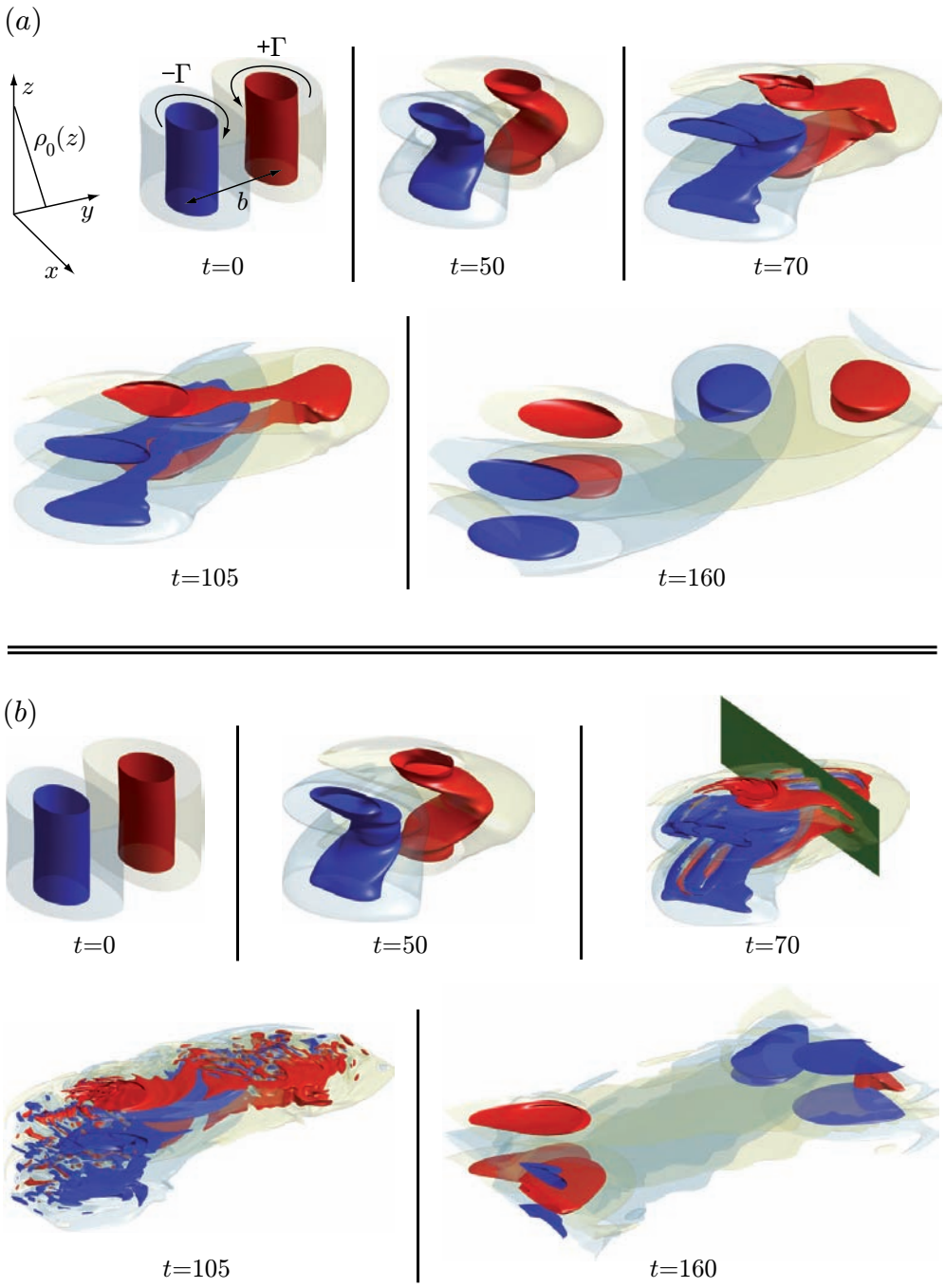

Figure 7.1: Vertical vorticity isosurfaces of the simulations (*a*) F0.6R1 ($F_h = 0.66$, $Re = 1060$) and (*b*) F0.6R3 ($F_h = 0.66$, $Re = 3180$). Red and deep blue contours represent respectively plus and minus 60% of $\langle \omega_z^{max} \rangle_z$, the vertical average of the maximum vertical vorticity in each horizontal plane. Transparent yellowish and bluish isosurfaces are the same for a 10% level. The green plane shown at $t = 70$ in (*b*) indicates the position of the vertical cross-sections presented in figures 7.5 and 7.7. The corresponding movies can be viewed on the on-line version of the journal alongside the paper.

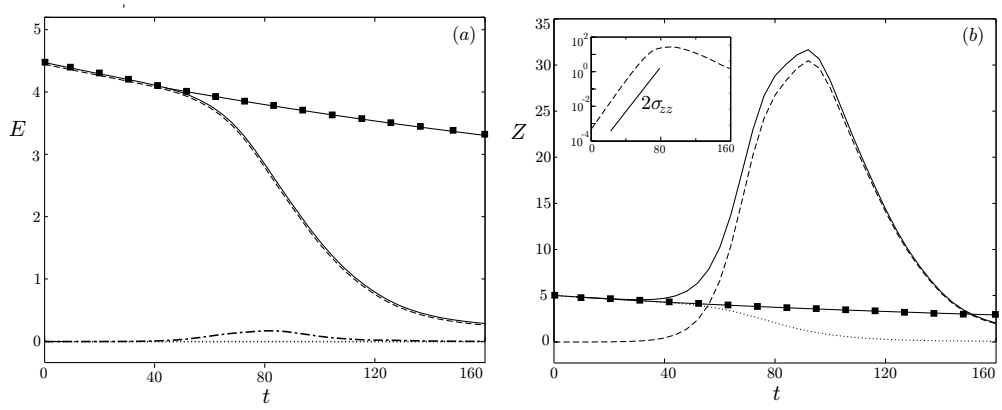

Figure 7.2: Energy (a) and enstrophy (b) evolutions of the run F0.6R1 ($F_h = 0.66$, $Re = 1060$). In (a), the total kinetic energy E_k^T is plotted (solid line) as well as its horizontal E_k^h (dash line) and vertical E_κ^v (dot line) components. Potential energy E_p (dash-dot line) is always negligible compared to the total kinetic energy E_k^T. The evolution of total kinetic energy for a two-dimensional simulation is also plotted (■ symbols). Plot (b) is similar to (a) but for the enstrophy Z. A semi-log plot of Z^h (i.e. $\log Z^h$ versus t) is inserted in the upper-left corner of (b) showing that Z^h grows exponentially in time until $t \sim 70$ at a rate of $2\sigma_{zz}$ where σ_{zz} is the growth rate of the zigzag instability.

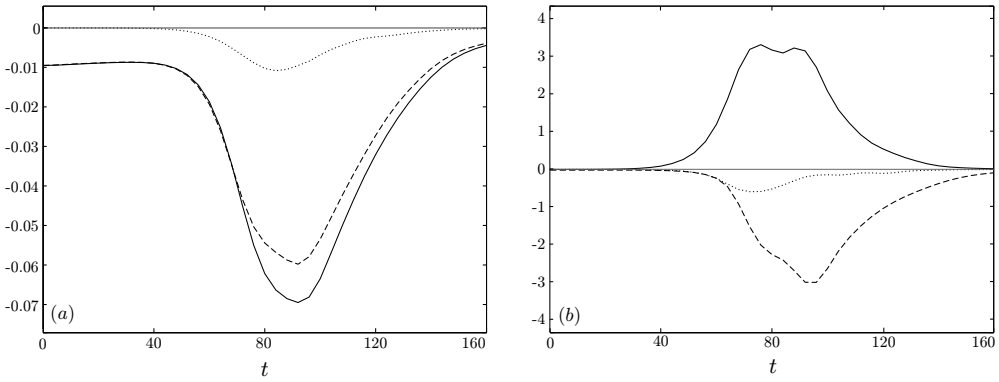

Figure 7.3: Evolutions of energy dissipation (a) and enstrophy sources (b) for run F0.6R1 ($F_h = 0.66$, $Re = 1060$). (a): the energy dissipation $\mathrm{d}(E_k^T + E_p)/\mathrm{d}t$ (solid line) is mainly caused by viscous effects (dash line) which are much more important than the potential energy dissipation (dot line). (b): evolution of the enstrophy sources: stretching (solid line), baroclinic (dot line) and viscous (dash line) terms.

three terms in figure 7.3(b) shows that the only source of enstrophy is the stretching term. This stretching effect comes from the high shear due to the bending of the vortices by the zigzag instability. It results in an exponential growth of horizontal enstrophy Z^h which becomes so large that $Z^T \sim Z^h$. It is then high enough to dissipate the initial kinetic energy and to saturate the development of the zigzag instability.

This physical mechanism implies that the maximum value of horizontal enstrophy Z^h_{max} is reached when the dissipation term in (7.3) induces an order one variation of the energy: $Z^T_{max}/Re \sim Z^h_{max}/Re = O(1)$. This is confirmed by figure 7.4 which shows the evolution of horizontal enstrophy for several simulations covering a range of Reynolds numbers from $Re = 1060$ to $Re = 12\,720$. As predicted, the maximum value of horizontal enstrophy (figure 7.4a) increases with the Reynolds number. There is an abrupt decrease for the runs with highest Reynolds numbers (F0.6R6 and F0.3R12) because of the intense development of the small-scale instability. However, the different curves collapse well when Z_h is rescaled by the Reynolds number (figure 7.4b).

The zigzag instability is therefore a shortcut on the route to dissipation since it produces a direct transfer of energy from the large scales to the small dissipative vertical scales. Horizontal enstrophy grows exponentially due to the zigzag instability until the vertical shear has reached the dissipative scales. This mechanism of stretching of the horizontal enstrophy can be seen as the stratified equivalent of the stretching of vortices in homogeneous flows. It eventually leads to a flow dominated by viscous effects.

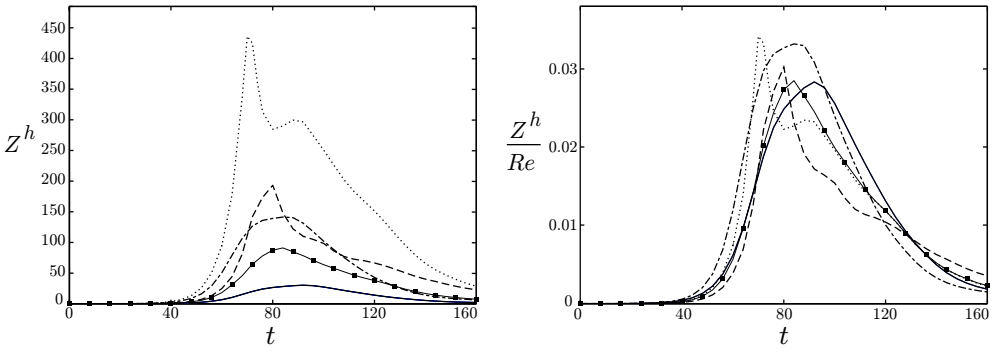

Figure 7.4: Evolutions of the horizontal enstrophy Z^h (a) and the rescaled horizontal enstrophy Z^h/Re (b) for different runs: F0.6R1 ($Re = 1060$, solid line), F0.6R3 ($Re = 3180$, ■ symbols), F0.3R4 ($Re = 4240$, dash-dot line), F0.6R6 ($Re = 6360$, dash line) and F0.3R12 ($Re = 12\,720$, dot line).

7.5 Kelvin–Helmholtz instability

Figure 7.1(b) corresponding to run F0.6R3 shows the development of small-scale structures in the highly sheared region of the vortices. To address their origin, several authors (Riley & deBruynKops 2003; Laval *et al.* 2003; Waite & Bartello 2004) have proposed to consider the local Richardson number Ri:

$$Ri = \frac{1 + \frac{\partial \rho}{\partial z}}{F_h^2 \left[\left(\frac{\partial u}{\partial z} \right)^2 + \left(\frac{\partial v}{\partial z} \right)^2 \right]}, \tag{7.5}$$

where $1 + \partial\rho/\partial z$ is the nondimensional vertical gradient of the total density. The presence of F_h in (7.5) comes from the nondimensionalization (see § 7.2).

Figure 7.5 shows a time series of the density perturbations and the local Richardson number in a vertical cross-section (whose position is indicated in figure 7.1b at $t = 70$). We clearly see (left column) small-scale billows resembling Kelvin–Helmholtz rolls at $t = 68$ and $t = 71$ but they are already incipient at $t = 65$ as marked by the arrows. The roll-up occurs in the regions where the Richardson number (right column) is lower than 1/4 demonstrating that its origin is the Kelvin–Helmholtz instability (Miles 1961; Howard 1961). This instability is not of Rayleigh-Taylor (gravitational) type since the Richardson number is positive just before its onset at $t = 65$ and becomes negative only in regions where the roll-up has occurred.

Following Riley & deBruynKops (2003), the presence or absence of the Kelvin–Helmholtz instability for a given set of parameters (F_h, Re) can be predicted using the Richardson criterion $Ri < 1/4$ and the scaling $Z^h_{max} \propto Re$. Indeed the nondimensional local vertical shear $(\partial u/\partial z)^2 + (\partial v/\partial z)^2$ can

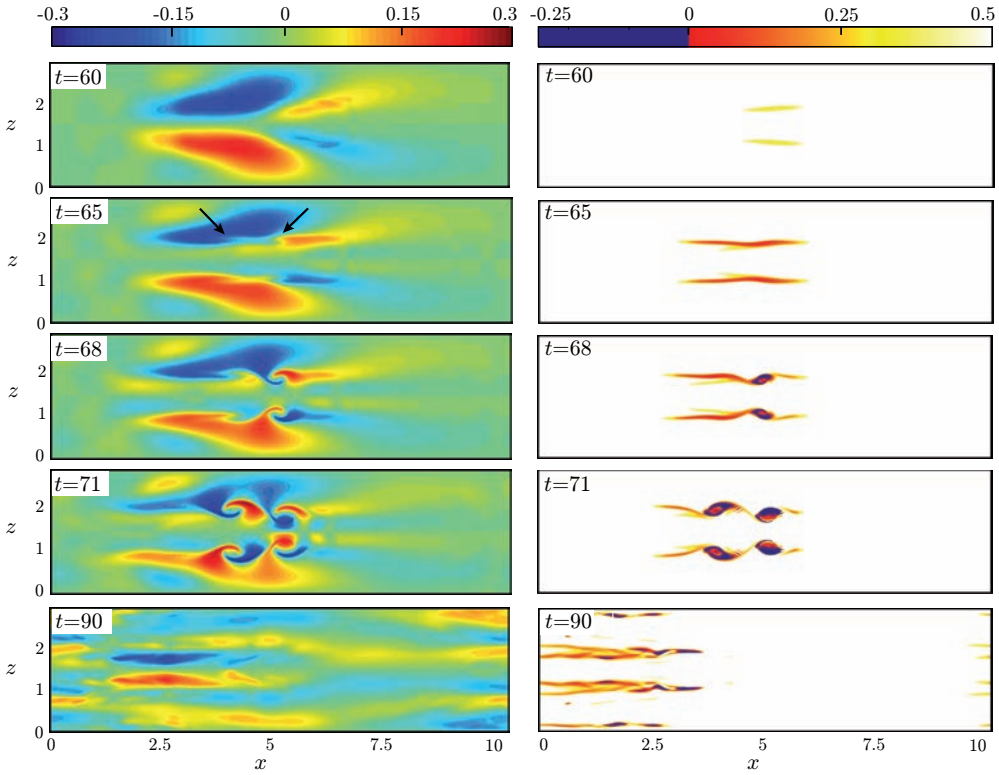

Figure 7.5: Time evolution of a vertical cross-section of density perturbations (left column) and Richardson number (right column) of the run F0.6R3 ($F_h = 0.66$, $Re = 3180$). The position of the cross-section is indicated in figure 7.1(b). The Kelvin–Helmholtz instability appears at $t = 65$ in regions where $Ri < 1/4$ and produces a roll-up as evidenced at $t = 68$ and $t = 71$ by the regions where Ri is negative. The billows breakdown into irregular structures by $t = 90$.

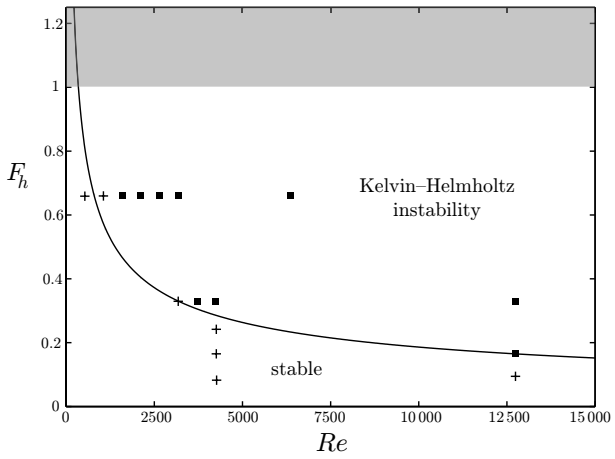

Figure 7.6: Summary of all the runs in F_h–Re plane. The symbol ■ indicates a run in which Kelvin–Helmholtz instabilities are observed ; otherwise a + symbol is used. The criterion for the occurrence of Kelvin–Helmholtz is the appearance of vertical roll-up. Note that additional runs not listed in table 7.1 have been performed in order to cover the F_h–Re plane. The solid line corresponds to the criterion $R = ReF_h^2 = 340$. In the shaded region ($F_h > 1$) the zigzag instability does not exist.

be estimated by the total vertical shear $S^2 = \langle(\partial u/\partial z)^2 + (\partial v/\partial z)^2\rangle$. This quantity is directly related to the total horizontal enstrophy $S^2 \sim 2Z^h$ when $F_h \ll 1$ since the vertical velocity is then very small and vertical derivatives are high (Billant & Chomaz 2001). Therefore, the minimum Richardson number is:

$$Ri_{min} \sim \frac{1}{S^2_{max}F_h^2} \sim \frac{1}{2Z^h_{max}F_h^2} \propto \frac{1}{ReF_h^2}, \tag{7.6}$$

where we have assumed that the total density gradient is of the order of the ambient density gradient, i.e. $1 + \partial\rho/\partial z \sim 1$.

Therefore, we expect the Kelvin–Helmholtz instability when $R = ReF_h^2$ is large. This is confirmed in figure 7.6 which summarizes all the runs in the parameters space (F_h, Re). We see that the threshold $R \sim 340$, determined empirically, discriminates quite well the runs where the Kelvin–Helmholtz instability has been observed from those where no such instability occurs (the threshold is slightly underestimated at small Re since the viscous dissipation of the base flow and of the perturbations is no longer small whereas it is neglected in the reasoning above).

Furthermore, the runs F0.6R3 and F0.6R6 shown in figure 7.7 have nearly identical roll-up indicating that the wavelength of the Kelvin–Helmholtz instability λ_{KH} is independent of the Reynolds number Re. On the contrary, it

is approximately proportional to the Froude number: $\lambda_{KH} \propto F_h$ as seen by comparing between the run F0.6R3 ($F_h = 0.66$, $\lambda_{KH} \sim 1$) and the run F0.3R4 ($F_h = 0.33$, $\lambda_{KH} \sim 0.55$) in figure 7.7. These observations are consistent with the Richardson number criterion since the nondimensional vertical shear S_c at onset of the Kelvin–Helmholtz instability is $S_c^2 \propto 1/F_h^2 Ri_c$ where $Ri_c = 1/4$ is the critical Ri. Since the wavelength of the Kelvin–Helmholtz instability scales on the shear thickness, i.e. $\lambda_{KH} \propto 1/S$, we deduce that $\lambda_{KH} \propto F_h$ at the instability onset in agreement with figure 7.7.

Subsequently, the Kelvin–Helmholtz billows breakdown into small-scales but disappear quite rapidly (figure 7.5). However, with much higher Reynolds numbers as in real geophysical flows, we would expect that the small scales created by the Kelvin–Helmholtz billows should evolve for a longer time before being dissipated and thus should play a more important role in the dynamics of the flow.

7.6 Conclusion and perspectives

We have performed direct numerical simulations of the nonlinear development of the zigzag instability of a pair of counter-rotating vertical vortices in a stratified fluid for various values of Reynolds numbers Re and Froude numbers F_h. We have observed that the zigzag instability develops exponentially without saturation by nonlinear inertial effects. Thus, the vortices are distorted in an extreme manner, creating high vertical shear, i.e. horizontal vorticity. The exponential growth of the instability is only stopped when the vertical shear is such that vertical viscous effects become of the same order as the horizontal transport, i.e. when the maximum nondimensional horizontal enstrophy is such that $Z^h_{max}/Re = O(1)$. The maximum in time of the horizontal enstrophy observed in all simulations agrees with this scaling law. The subsequent evolution of the flow is dominated by vertical viscous effects.

We have also shown that the intense vertical shear created by the zigzag instability leads to Kelvin–Helmholtz instabilities for large values of $R = ReF_h^2 \gtrsim 340$, which allow for $Ri_{min} < 1/4$ since $Ri_{min} \propto 1/ReF_h^2$ following the arguments of Riley & deBruynKops (2003).

As pointed out by Riley & deBruynKops (2003), the appearance of Kelvin–Helmholtz instabilities agrees to some extent with the suggestion of Lilly (1983) that vertical shear should increase in time and lead to Kelvin–Helmholtz instabilities. However, Lilly's suggestion is based on the hypothesis that a strongly stratified flow is a stack of two-dimensional flows without vertical coupling. In this case, a mean vertical shear increases algebraically in time if it is initially non-zero. In contrast, we have shown that the vertical shear arises spontaneously and grows exponentially in time because of the zigzag instability.

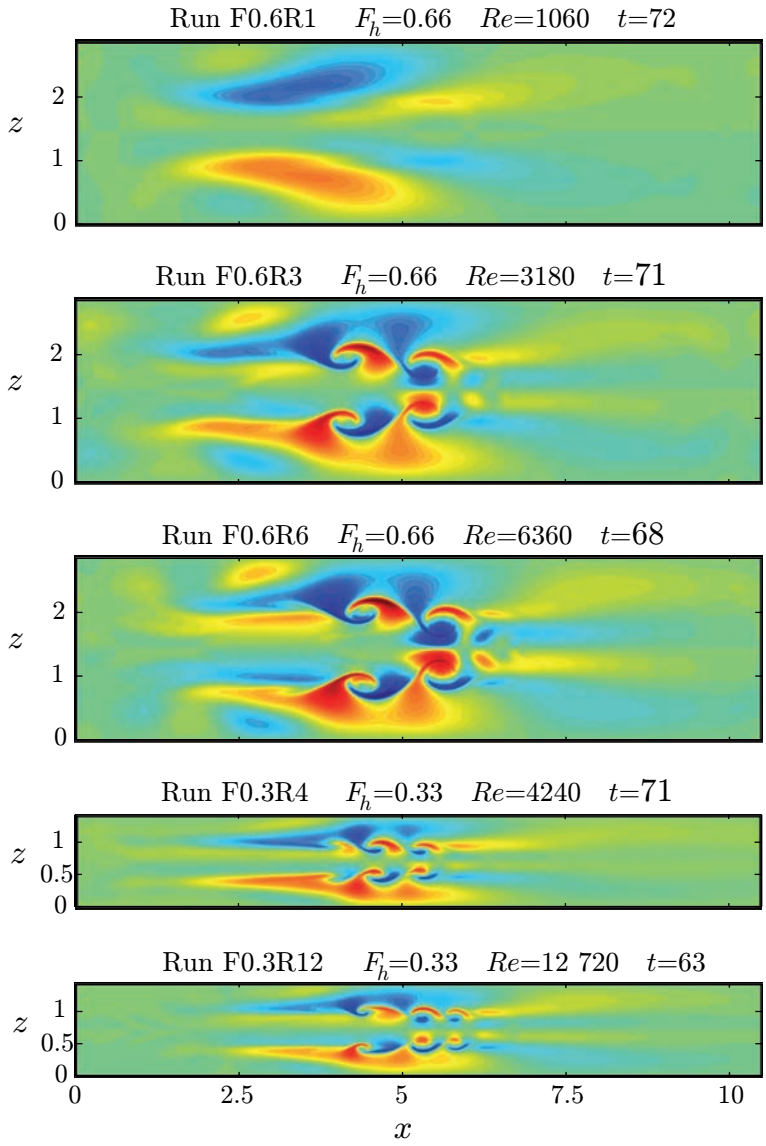

Figure 7.7: Vertical cross-sections of density perturbations for different simulations. The exact time of the cross-section is approximately the same but is adjusted for each simulation to show fully developed Kelvin–Helmholtz billows if any can be observed.

Kelvin–Helmholtz instabilities are therefore expected to develop much faster than speculated by Lilly (1983).

Recent work have demonstrated that the zigzag instability is a generic linear instability mechanism that applies to many vorticity distributions such as a pair of counter-rotating vortices (Billant & Chomaz 2000*a*), a pair of co-rotating vortices (Otheguy *et al.* 2006), an elliptic vortex with background strain (Billant *et al.* 2006), or vortex arrays (forthcoming paper). If we try to generalize the present results, pertaining to an idealized case, to more complex stratified flows and stratified turbulence, we may speculate that any flow with initial small horizontal and vertical Froude numbers should exhibit a cascade of instabilities similar to the one presented here. The energy should be first transferred from large to small vertical scales by zigzag instability and then jump from large to small horizontal scales by Kelvin–Helmholtz instability. These small vertical and horizontal scales are both of the order of the Ozmidov scale. This direct transfer to the Ozmidov scale is an alternative to the stratified turbulent cascade proposed by Lindborg (2006) and Brethouwer *et al.* (2007).

After completion of this work, we have been aware of a related study by Waite & Smolarkiewicz (2007). In their Large-Eddy Simulations (LES) at large Schmidt number, they study the nonlinear evolution of the zigzag instability for a Lamb–Chaplygin dipole. They observe small-scale structures that they identify as a gravitational instability. In the present DNS study, we also observe overturning but caused by the nonlinear development of Kelvin–Helmholtz instabilities. This apparent discrepancy might be due to the influence of the Schmidt number or to the difference of initial state. This is an issue that deserves further investigation.

This work is supported by IDRIS (CNRS) for computational facilities under project No. 61722.

Chapter 8

Conclusions and perspectives

8.1 Conclusions

The main purpose of this dissertation has been the study of the fundamental processes which can explain the structure and dynamics of stratified turbulence. We have investigated here the role of the zigzag instability which is a three-dimensional instability that vertically bends interacting columnar vortices with a most unstable vertical wavelength scaling like the buoyancy length scale. The first main conclusion is that the zigzag instability is a generic mechanism that affects complex flows made of a large number of interacting vertical vortices. The second main conclusion is that the nonlinear evolution of the zigzag instability is associated to a rapid transfer of energy from large scales to the small vertical dissipative scales. These two results suggest that the zigzag instability can be significant to explain the formation of horizontal layers and the direct energy cascade observed in stratified turbulence.

In the following, the main results of each chapter are briefly recalled.

Chapter 3: we have studied numerically the three-dimensional stability of a horizontal flow sheared horizontally, the hyperbolic tangent velocity profile, in a stably stratified fluid. When the Froude number, F_h, is varied from ∞ to 0.05, the most unstable mode remains two-dimensional. We could not find any three-dimensional instability of zigzag type, suggesting that the zigzag instability only develops in flows with interacting vortices. However, the range of unstable vertical wavenumbers widens proportionally to the inverse of the Froude number for $F_h \ll 1$, meaning that there is a loss of selectivity of the two-dimensional mode for strong stratifications.

Chapters 4 and 5: we have studied theoretically in chapter 4, the three-dimensional stability of arrays of columnar vortices in a stratified and rotating

fluid: the Kármán vortex street, the symmetric double row and the single row. we have found that when the fluid is sufficiently stratified (i.e. $F_h \leq F_{hc}$ where $F_{hc} \approx 1.3 - 1.6$ depending on the parameters of the arrays), the zigzag instability is dominant whatever the Rossby number for both the Kármán vortex street with close rows and the symmetric double row for any street spacing ratio. It confirms that the zigzag instability is a generic mechanism that affects complex flows made of a large number of interacting vertical vortices. The Kármán vortex street for distant rows and the single row are most unstable to a two-dimensional pairing instability for any Rossby number. These results were fully confirmed by the numerical analysis of chapter 5.

Chapter 6: we have tackled the three-dimensional stability of unsteady distributions of vortices that are initially two-dimensional. These flows have been found to be unstable to the zigzag instability with a zigzag pattern that becomes more distorted when a large number of vortices are interacting. This confirms again that the zigzag instability is a robust mechanism that applies to many vorticity distributions.

Chapter 7: we have performed direct numerical simulations of the nonlinear development of the zigzag instability of a pair of counter-rotating vertical vortices in a stratified fluid for various values of Reynolds numbers Re and Froude numbers F_h. We have observed that the zigzag instability develops exponentially without saturation by nonlinear inertial effects. Thus, the vortices are distorted in an extreme manner, creating high vertical shear, i.e. horizontal vorticity. The exponential growth of the instability is only stopped when the vertical shear is such that vertical viscous effects become of the same order as the horizontal transport, i.e. when the maximum nondimensional horizontal enstrophy is such that $Z^h_{max}/Re = O(1)$. The subsequent evolution of the flow is dominated by vertical viscous effects. The zigzag instability therefore transfers directly the energy from large scales to the small dissipative vertical scales. We have not found successive zigzag instabilities that break-up pancake vortices into smaller structures. However, for high Reynolds number, the vertical shear created by the zigzag instability is so intense that small-scale Kelvin–Helmholtz secondary instabilities develop.

8.2 Suggestions for future work

If we consider that two-dimensional vortices are a continuous source of energy at large scales in geophysical stratified flows, an extension of this work would be to study the effects of the zigzag instability on a stratified turbulent flow forced by columnar vortices. An experimental study has been already initiated at LadHyX. The experiment (see figure 8.1) is performed in a tank filled with

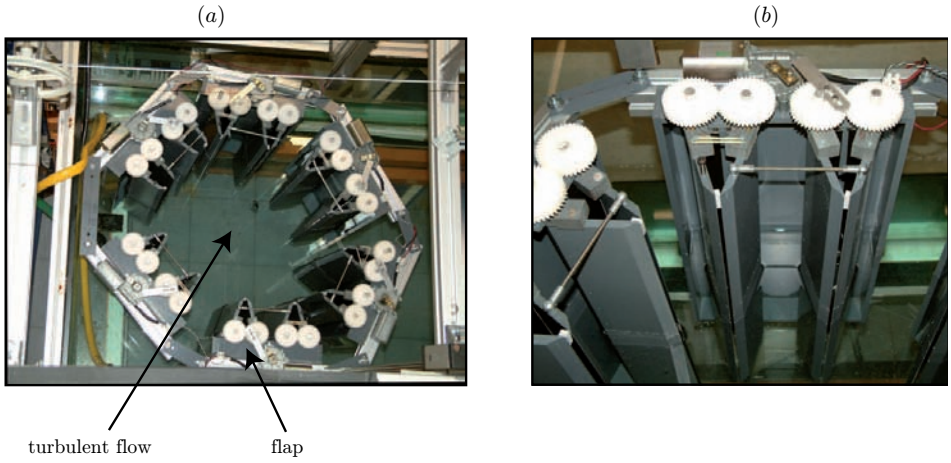

Figure 8.1: Experimental set-up to study stratified turbulence forced by vertical columnar vortices. A set of 14 flaps disposed radially produce columnar vortices that propagate towards the centre area. (a): Top-view. (b): Close-up view of flaps.

a linearly stratified salt solution. A set of 14 vertical "flaps" are disposed radially. Each flap, by suddenly closing at random times, generate a pair of counter-rotating columnar vortices that propagate towards the central area, providing energy to the turbulent flow. The three-dimensionalization of the columnar vortices and the energy transfers from the injection large scale to small dissipative scales should be determined and compared to the results of this dissertation. Before the completion of this dissertation, we unfortunately did not have enough time to properly run the experiment.

Bibliography

Basak, S. & Sarkar, S. 2006 Dynamics of a stratified shear layer with horizontal shear. *J. Fluid Mech.* **568**, 19–54.

Billant, P. & Chomaz, J.-M. 2000*a* Experimental evidence for a new instability of a vertical columnar vortex pair in a strongly stratified fluid. *J. Fluid Mech.* **418**, 167–188.

Billant, P. & Chomaz, J.-M. 2000*b* Theoretical analysis of the zigzag instability of a vertical columnar vortex pair in a strongly stratied fluid. *J. Fluid Mech.* **419**, 29–63.

Billant, P. & Chomaz, J.-M. 2000*c* Three-dimensional stability of a vertical columnar vortex pair in a stratified fluid. *J. Fluid Mech.* **419**, 65–91.

Billant, P. & Chomaz, J. M. 2001 Self-similarity of strongly stratified inviscid flows. *Phys. Fluids* **13**, 1645–1651.

Billant, P., Deloncle, A., Chomaz, J.-M. & Otheguy, P. 2007 A general theory for the zigzag instability of vortices in stratified and rotating fluids. *J. Fluid Mech.* (to be submitted).

Billant, P., Dritschel, D. G. & Chomaz, J.-M. 2006 Bending and twisting instabilities of columnar elliptical vortices in a rotating strongly stratified fluid. *J. Fluid Mech.* **561**, 73–102.

Blumen, W. 1970 Hydrostatic neutral waves in a parallel shear flow of a stratified fluid. *J. Atmos. Sci.* **28**, 340–344.

Boyd, J. P. 2001 *Chebyshev and Fourier spectral methods*, 2nd edn. Dover.

Brethouwer, G., Billant, P., Lindborg, E. & Chomaz, J.-M. 2007 Scaling analysis and simulation of strongly stratified turbulent flows. *J. Fluid Mech.* **585**, 343–368.

Cho, J. Y. N. & Lindborg, E. 2001 Horizontal velocity structure functions in the upper troposphere and lower stratosphere 1. Observations. *J. Geophys. Res.* **106**, (D10), 10223–10232.

Clercx, H. J. H., Maassen, S. R. & van Heijst, G. J. F. 1999 Decaying two-dimensional turbulence in square containers with no-slip and stress-free boundaries. *Phys. Fluids* **11**, 611–626.

Cot, C. 2001 Equatorial mesoscale wind and temperature fluctuations in the lower atmosphere. *J. Geophys. Res.* **106**, D2, 1523–1532.

Crow, S. C. 1970 Stability theory for a pair of trailing vortices. *A.I.A.A. J.* **8**, 2172–2179.

Deloncle, A., Billant, P. & Chomaz, J.-M. 2007*a* Nonlinear evolution of the zigzag instability in stratified fluids: a shortcut on the route to dissipation. *J. Fluid Mech.* (submitted).

Deloncle, A., Billant, P. & Chomaz, J.-M. 2007*b* Three-dimensional stability of a horizontally sheared flow in a stably stratified fluid. *J. Fluid Mech.* **570**, 297–305.

Deloncle, A., Billant, P. & Chomaz, J.-M. 2007*c* Three-dimensional stability of vortex arrays in a strongly stratified and rotating fluid: numerical analysis. *J. Fluid Mech.* (in preparation).

Deloncle, A., Billant, P. & Chomaz, J.-M. 2007*d* Three-dimensional stability of vortex arrays in a strongly stratified and rotating fluid: theoretical analysis. *J. Fluid Mech.* (in preparation).

Etling, D. 1990 Mesoscale vortex shedding from large islands: a comparison with laboratory experiments of rotating stratified flows. *Meteorol. Atmos. Phys.* **43**, 145–151.

Falkovich, G. & Sreenivasan, K. R. 2006 Lessons from hydrodynamic turbulence. *Physics Today* **April**, 43–49.

Fjòrtoft, R. 1950 Application of integral theorems in deriving criteria for instability for laminar flows and for the baroclinic circular vortex. *Geofys. Publ., Oslo* **17**, 1–52.

Gill, A. E. 1982 *Atmosphere-Ocean Dynamics*. Academic.

Godeferd, F. S. & Staquet, C. 2003 Statistical modelling and direct numerical simulations of decaying stably stratified turbulence. Part 2. Large-scale and small-scale anisotropy. *J. Fluid Mech.* **486**, 115–159.

Grosch, C. E. & Orszag, S. A. 1977 Numerical solution of problems in unbounded regions: coordinates transforms. *J. Comput. Phys.* **25**, 273–296.

Ho, C. M. & Huerre, P. 1984 Perturbed shear layers. *Annu. Rev. Fluid. Mech.* **16**, 365–424.

Holford, M. & Linden, P. F. 1999 Turbulent mixing in a stratified fluid. *Dyn. Atmos. Oceans* **30**, 173–198.

Howard, L. N. 1961 Note on a paper of John W. Miles. *J. Fluid Mech.* **10**, 509–512.

Jimenez, J. 1975 Stability of a pair of co-rotating vortices. *Phys. Fluids* **18**, 1580–1581.

von Kármán, T. 1911 Über den mechanismus des widerstands, den ein bewegter körper in einer flüssigkeit erfährt. *Göttinger Nachrichten, Math. Phys. Kl.* pp. 509–517.

von Kármán, T. 1912 Über den mechanismus des widerstands, den ein bewegter körper in einer flüssigkeit erfährt. *Göttinger Nachrichten, Math. Phys. Kl.* pp. 547–556.

von Kármán, T. & Rubach, H. L. 1912 Über den mechanismus des flüssigkeits- und luftwiderstands. *Phys. Z.* **13**, 49–59.

Kolmogorov, A. N. 1941 The local structure turbulence in incompressible viscous fluids for very large reynolds numbers. *Dokl. Akad. Nauk. SSSR* **30**, 301–305.

Kraichnan, R. H. 1967 Inertial ranges in two-dimensional turbulence. *Phys. Fluids* **10**, 1417–1423.

Lamb, H. 1932 *Hydrodynamics*. Cambridge University Press.

Laval, J.-P., McWilliams, J. C. & Dubrulle, B. 2003 Forced stratified turbulence: successive transitions with Reynolds number. *Phys. Rev.* E **68**, 036308.

Leblanc, S. & Cambon, C. 1998 Effects of the Coriolis force on the stability of Stuart's vortices. *J. Fluid Mech.* **356**, 353–379.

Lilly, D. K. 1983 Stratified turbulence and the mesoscale variability of the atmosphere. *J. Atmos. Sci.* **40**, 749–761.

Lindborg, E. 1999 Can the atmospheric kinetic energy spectrum be explained by twodimensional turbulence? *J. Atmos. Sci.* **388**, 259–288.

Lindborg, E. 2006 The energy cascade in a strongly stratified fluid. *J. Fluid Mech.* **550**, 207–242.

Michalke, A. 1964 On the inviscid instability of the hyperbolic tangent velocity profile. *J. Fluid Mech.* **19**, 543–556.

Miles, J. W. 1961 On the stability of heterogeneous shear flows. *J. Fluid Mech.* **10**, 496–508.

Morize, C. 2006 De la turbulence 3D en dclin la turbulence anisotrope dominée par la rotation. PhD thesis, Université Paris 7.

Nastrom, G. D. & Gage, K. S. 1985 A climatology of atmospheric wavenumber spectra of wind and temperature observed by commercial aircraft. *J. Atmos. Sci.* **42**, 950–960.

Otheguy, P., Chomaz, J.-M. & Billant, P. 2006 Elliptic and zigzag instabilities on co-rotating vertical vortices in a stratified fluid. *J. Fluid Mech.* **553**, 253–272.

Pedlosky, J. 1982 *Geophysical Fluid Dynamics*, 2nd edn. Springer.

Petitjeans, P. 2003 Stretching of a vortical structure: filaments of vorticity. *Europhysics News* **34 (1)**.

Potylitsin, P. G. & Peltier, W. R. 1998 Stratification effects on the stability of columnar vortices on the f-plane. *J. Fluid Mech.* **355**, 45–79.

Potylitsin, P. G. & Peltier, W. R. 1999 Three-dimensional destabilization of Stuart vortices: the influence of rotation and ellipticity. *J. Fluid Mech.* **387**, 205–226.

Praud, O., Fincham, A. M. & Sommeria, J. 2005 Decaying grid turbulence in a strongly stratified fluid. *J. Fluid Mech.* **522**, 1–33.

Rayleigh, L. 1887 On the stability of certain fluid motions. *Proc. Math. Soc. Lond.* **11**, 57–70.

Richardson, L. F. 1922 *Weather Prediction by Numerical Process*. Cambridge University Press.

Riley, J. J. & deBruynKops, S. M. 2003 Dynamics of turbulence strongly influenced by buoyancy. *J. Fluid Mech.* **15**, 2047–2059.

Riley, J. J. & Lelong, M.-P. 2000 Fluid motion in the presence of strong stable stratification. *Annu. Rev. Fluid. Mech.* **32**, 613–657.

Riley, J. J., Metcalfe, W. & Weissman, M. A. 1981 Direct numerical simulations of homogeneous turbulence in density-stratified fluids. In *Proc. AIP Conf. Nonlinear Properties of Internal Waves*, pp. 79–112. Bruce J. West.

Robinson, A. C. & Saffman, P. G. 1982 Three-dimensional stability of vortex arrays. *J. Fluid Mech.* **125**, 411–427.

Schmid, P. J. & Henningson, D. S. 2001 *Stability and transition in shear flows*. Springer.

Sipp, D., Jacquin, L. & Cossu, C. 2000 Self-adaptation and viscous selection in concentrated two-dimensional vortex dipoles. *Phys. Fluids* **12**, 245–248.

Smith, S. A., Fritts, D. C. & Zandt, T. E. V. 1987 Evidence for a saturated spectrum of atmospheric gravity waves. *J. Atmos. Sci.* **44**, 1404–1410.

Squire, H. B. 1933 On the stability for three-dimensional disturbances of viscous fluid flow between parallel walls. *Proc. Math. Soc. Lond.* A **142**, 621–628.

Staquet, C. & Sommeria, J. 2002 Internal gravity waves, from instabilities to turbulence. *Annu. Rev. Fluid. Mech.* **34**, 559–593.

Vincent, A. & Meneguzzi, M. 1991 The spatial structure and statistical properties of homogeneous turbulence. *J. Fluid Mech.* **225**, 1–20.

Waite, M. L. & Bartello, P. 2004 Stratified turbulence dominated by vortical motion. *J. Fluid Mech.* **517**, 281–308.

Waite, M. L. & Smolarkiewicz, P. 2007 Instability and breakdown of a vertical vortex pair in a strongly stratified fluid. *J. Fluid Mech.* (submitted).